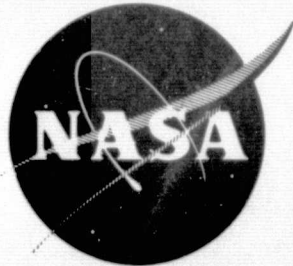


General Disclaimer

One or more of the Following Statements may affect this Document

- This document has been reproduced from the best copy furnished by the organizational source. It is being released in the interest of making available as much information as possible.
- This document may contain data, which exceeds the sheet parameters. It was furnished in this condition by the organizational source and is the best copy available.
- This document may contain tone-on-tone or color graphs, charts and/or pictures, which have been reproduced in black and white.
- This document is paginated as submitted by the original source.
- Portions of this document are not fully legible due to the historical nature of some of the material. However, it is the best reproduction available from the original submission.



DEVELOPMENT OF A PLASMA SPRAYED CERAMIC GAS PATH
SEAL FOR HIGH PRESSURE TURBINE APPLICATIONS

FINAL REPORT

by
L. T. Shiembob

(NASA-CR-135183) DEVELOPMENT OF A PLASMA
SPRAYED CERAMIC GAS PATH SEAL FOR HIGH
PRESSURE TURBINE APPLICATIONS Final Report,
2 Oct. 1975 - 31 Dec. 1976 (Pratt and
Whitney Aircraft) 124 p HC AC6/MF A01

N77-25534

G3/37 29121
Unclas

PRATT & WHITNEY AIRCRAFT GROUP
COMMERCIAL PRODUCTS DIVISION
UNITED TECHNOLOGIES CORPORATION

Prepared for

NATIONAL AERONAUTICS AND SPACE ADMINISTRATION

NASA-Lewis Research Center
Contract NAS3-19759



1. Report No. NASA CR 135183		2. Government Accession No.		3. Recipient's Catalog No.	
4. Title and Subtitle DEVELOPMENT OF A PLASMA SPRAYED CERAMIC GAS PATH SEAL FOR HIGH PRESSURE TURBINE APPLICATIONS				5. Report Date April 1977	
				6. Performing Organization Code	
7. Author(s) L. T. Shiembob				8. Performing Organization Report No. PWA-5521	
9. Performing Organization Name and Address Pratt & Whitney Aircraft Group Commercial Products Division United Technologies Corporation, East Hartford, Connecticut 06108				10. Work Unit No.	
				11. Contract or Grant No. NAS3-19759	
12. Sponsoring Agency Name and Address U.S. Army Air Mobility Research and Development Lab. Lewis Directorate Cleveland, Ohio 44135				13. Type of Report and Period Covered Contractor Report. 10/2/75 - 12/31/76	
				14. Sponsoring Agency Code	
15. Supplementary Notes Project Manager, Dr. Robert C. Bill NASA Lewis Research Center Cleveland, Ohio					
16. Abstract <p>The objective of this program was continued development of the plasma sprayed graded layered yttria stabilized zirconia (ZrO_2)/metal (CoCrAlY) seal system for gas turbine blade tip applications up to 1589°K (2400°F) seal temperatures. Abradability, erosion and thermal fatigue characteristics of the graded layered system were evaluated by rig tests. Satisfactory abradability and erosion resistance was demonstrated. Encouraging thermal fatigue tolerance was shown. Initial properties for the plasma sprayed materials in the graded, layered seal system was obtained and thermal stress analyses were performed. As sprayed residual stresses were determined. Thermal stability of the sprayed layer materials was evaluated at estimated maximum operating temperatures in each layer. Anisotropic behavior in the layer thickness direction was demonstrated by all layers. Residual stresses and thermal stability effects were not included in the analyses.</p> <p>Analytical results correlated reasonably well with results of the thermal fatigue tests. Analytical application of the seal system to a typical gas turbine engine application predicted performance similar to rig specimen thermal fatigue performance. A model for predicting crack propagation in the sprayed ZrO_2/CoCrAlY seal system was proposed and recommendations for improving thermal fatigue resistance were made. Seal system layer thicknesses were analytically optimized to minimize thermal stresses in the abradability specimen during thermal fatigue testing. Rig tests on the optimized seal configuration demonstrated some improvement in thermal fatigue characteristics.</p>					
17. Key Words (Suggested by Author(s))				18. Distribution Statement	
Abradable Seal Thermal Conductivity Turbine Seal Thermal Expansion Blade Tip Seal Rupture Modulus Gas Path Seal Ultimate Strength Ceramic Seal Residual Stress High Temperature Seal Prestress Zirconia Plasma Sprayed Seal Abradability Material Properties Erosion Physical Properties Thermal Stability Mechanical Properties Elastic Modulus					
19. Security Classif. (of this report) Unclassified		20. Security Classif. (of this page) Unclassified		21. No. of Pages 115	
				22. Price*	

* For sale by the National Technical Information Service, Springfield, Virginia 22151

FOREWORD

This report describes the work accomplished under NASA Contract NAS3-19759 and modification 1 thereto by the Pratt & Whitney Aircraft (P&WA) Division of United Technologies Corporation for the Lewis Research Center of the National Aeronautics and Space Administration. The technical effort was initiated on 2 October 1975 and completed on 31 December 1976.

Dr. Robert C. Bill of the National Aeronautics and Space Administration (NASA) was the Project Manager and Mr. Leonard W. Schopen of the NASA Research Center was the Contracting Officer.

Mr. Lawrence T. Shiembob was the Program Manager for Pratt & Whitney Aircraft.

Appreciation is extended to the following P&WA personnel for their assistance: Oscar L. Stewart, Senior Experimental Engineer, for overall program assistance; William D. Marscher, Senior Analytical Engineer, for contributions to the crack propagation study and general guidance and assistance with the thermal stress analysis; and Peter W. Schilke, Assistant Materials Project Engineer, Paul L. Crosswaith and Arnold S. Grot, Materials Engineers, for assistance in determining materials properties and metallurgical analyses.

TABLE OF CONTENTS

Section	Subject	Page No.
ABSTRACT		ii
FOREWORD		iii
TABLE OF CONTENTS		iv
LIST OF ILLUSTRATIONS		v
LIST OF TABLES		ix
1.0	SUMMARY AND CONCLUSIONS	1
	1.1 Summary of Results	1
	1.2 Conclusions	3
2.0	RECOMMENDATIONS	5
3.0	INTRODUCTION	6
	3.1 Background	6
	3.2 Program Objective	7
	3.3 Approach	7
4.0	TECHNICAL PROGRAM	9
	4.1 Seal Selection	9
	4.2 Performance Tests	10
	4.2.1 Abradability Tests	10
	4.2.2 Erosion Tests	13
	4.2.3 Thermal Fatigue Tests	14
	4.3 Materials Properties	17
	4.3.1 Physical and Mechanical Properties	17
	4.3.1.1 Hardness	17
	4.3.1.2 Linear Thermal Expansion Coefficient	18
	4.3.1.3 Thermal Conductivity	19
	4.3.1.4 Moduli of Elasticity and Rupture	20
	4.3.2 Thermal Stability	22
	4.3.3 Residual Stresses	22
	4.4 Analysis	23
	4.4.1 General Approach	23
	4.4.2 Thermal Fatigue Test Specimen Analysis	24
	4.4.3 Engine Application Analysis	26
	4.5 Cyclic Crack Propagation Study	27
	4.5.1 Literature Survey	27
	4.5.2 Analytical Application of Theory	28
	4.5.3 Methods of Increasing Cyclic Life	31
	4.6 Geometric Optimization of the Layer Structure	34
	4.6.1 Analysis	35
	4.6.2 Verification Tests	36
	4.6.3 Conclusions and Recommendations	38
REFERENCES		
APPENDIX A		

LIST OF ILLUSTRATIONS

Figure No.	Title	Page No.
1	Plasma Sprayed Graded Layered Y_2O_3 Stabilized $ZrO_2/CoCrAlY$ Seal System	55
2	High Temperature Abradability Test Rig	55
3	Abradability Sensitivity to Incursion Rate	56
4	Abnormal Blade Tip Wear (Abradability Test No. 1)	57
5	Test Specimen (Abradability Test No.1)	57
6	Axial Cracks in Rub Path (Abradability Test No. 3)	58
7	Metal Pickup on Leading Side of Blades (Abradability Test No. 6)	59
8	Metal Deposits on Seal Specimen Downstream of Rubbed Area (Abradability Test No. 6)	59
9	Metal Transfer and Seal Densification in Rub Path (Abradability Specimen No. 3)	60
10	Typical Cracks in Circumferential Section (Abradability Test No. 3)	61
11	Hot Particulate Erosion Rig	62
12	Erosion Test Specimen	62
13	Tested Erosion Specimens	63
14	Erosion Test Data Correlation	64
15	Thermal Fatigue Test Cycle, Abradability Specimen	65
16	Thermal Fatigue Test Cycle, Erosion Specimen	66
17	Thermal Fatigue Test Rig	67
18	Thermal Fatigue Specimen (Test No. 1)	68
19	Thermal Fatigue Specimen (Test No. 2)	69

LIST OF ILLUSTRATIONS (Cont'd)

Figure No.	Title	Page No.
20	Thermal Fatigue Specimen (Test No. 3)	70
21	Thermal Fatigue Specimen (Test No. 4)	71
22	Thermal Fatigue Specimen (Test No. 5)	72
23	Microstructure of NAS3-18565 Specimen	73
24	Microstructure of NAS3-19759 Specimen	74
25	Sprayed ZrO_2 Mean Coefficient of Thermal Expansion from 293°K (68°F)	75
26	Sprayed 85/15 ZrO_2 /CoCrAlY Mean Coefficient of Thermal Expansion from 293°K (68°F)	76
27	Sprayed 70/30 ZrO_2 /CoCrAlY Mean Coefficient of Thermal Expansion from 293°K (68°F)	77
28	Sprayed 40/60 ZrO_2 /CoCrAlY Mean Coefficient of Thermal Expansion from 293°K (68°F)	78
29	Thermal Conductivity of Sprayed ZrO_2 Layer	79
30	Thermal Conductivity of Composite Sprayed ZrO_2 /CoCrAlY Seal Coating	79
31	Estimated Thermal Conductivities for Mixed ZrO_2 /CoCrAlY Layers	80
32	Linear Change Due to Thermal Exposure, 1589K (2400F), ZrO_2 Layer	80
33	Linear Change Due to Thermal Exposure, 144K (1600F), 85/15 ZrO_2 /CoCrAlY Layer	81
34	Linear Change Due to Thermal Exposure, 1061K (1450F), 70/30 ZrO_2 /CoCrAlY Layer	81
35	Linear Change Due to Thermal Exposure 1005K (1350F) 40/60 ZrO_2 /CoCrAlY Layer	81
36	Volume Change Due to Thermal Exposure	82

LIST OF ILLUSTRATIONS (Cont'd)

Figure No.	Title	Page No.
37	Weight Change Due to Thermal Exposure	83
38	Residual Stress Machining Fixture	84
39	Residual Stress Distribution in Plasma Sprayed ZrO ₂ /CoCrAlY Erosion Specimen	85
40	Analytical Approach	86
41	Thermal Fatigue Test Specimen Maximum Principal Circumferential Stresses at Idle	87
42	Thermal Fatigue Test Specimen Maximum Principal Axial Stresses at Idle	88
43	Thermal Fatigue Test Specimen Maximum Principal Circumferential Stresses at 20.5 Sec. Accel.	89
44	Thermal Fatigue Test Specimen Maximum Principal Axial Stresses at 20.5 Sec. Accel.	90
45	Thermal Fatigue Test Specimen Maximum Principal Circumferential Stresses at SLTO	91
46	Thermal Fatigue Test Specimen Maximum Principal Axial Stresses at SLTO	92
47	Thermal Fatigue Test Specimen Maximum Principal Circumferential Stresses at 17.5 Sec. Decel.	93
48	Thermal Fatigue Test Specimen Maximum Principal Axial Stresses at 17.5 Sec. Decel.	94
49	Typical Engine Seal Segment	95
50	Engine Seal Segment Calculated Temperature Cycle at Hottest Location	96
51	Engine Seal Segment Temperature Distribution at 12 Sec. Decel.	97
52	Engine Seal Segment Maximum Principal Axial Stress Distribution at 12 Sec. Decel.	98

LIST OF ILLUSTRATIONS (Cont'd)

Figure No.	Title	Page No.
53	Engine Seal Segment Maximum Principal Circumferential Stress Distribution at 12 Sec. Decel.	99
54	Crack Tip to Applied Stress Ratio vs. Crack Length	100
55	Initial Stress Field	101
56	Crack Entering 85/15 ZrO ₂ /CoCrAlY Layer	102
57	Crack Allowed to Turn at Interface with 85/15 ZrO ₂ /CoCrAlY Layer	103
58	Stress at Irregular Edge	104
59	Location of Temperatures and Stresses Reported in Table XIII	104
60	Erosion Specimen, Optimized Configuration	105
61	Optimized Configuration, Thermal Fatigue Test (Test No. 6)	106
62	Optimized Configuration, Thermal Fatigue Test (Test No. 7)	107
63	Optimized Configuration, Thermal Fatigue Tested Specimen, Axial Section (Test No. 6)	108
64	Optimized Configuration, Thermal Fatigue Tested Specimen, Circumferential Section (Test No. 6)	109
65	Optimized Configuration Microstructure	110

LIST OF TABLES

Table No.	Title	Page No.
I	Single Blade/Multi-Blade Comparison	42
II	Abradability Test Schedule	42
III	Abradability Test Data Summary	43
IV	Erosion Test Schedule	44
V	Erosion Test Data Summary	45
VI	Thermal Fatigue Test Summary	46
VII	Average Layer Thicknesses, Thermal Fatigue Specimens	47
VIII	Porosity and Metal Volume Fractions of Thermal Fatigue Specimens	47
IX	Average Moduli of Rupture and Elasticity and Strain to Failure Test Results	48
X	Geometric Optimization Study, Configurations Analyzed	49
XI	Geometric Optimization Study, Summary of Results	50/51
XII	Optimized Configuration, Erosion Specimen Measured Layer Thickness	52
XIII	Optimized Configuration, Thermal Fatigue Specimen Measured Layer Thickness	53
XIV	Porosity and Metal Content of Composite Layers Determined by Point Count Method for Optimized Configuration	54

1.0 SUMMARY AND CONCLUSIONS

1.1 SUMMARY OF RESULTS

The plasma sprayed graded layered Y_2O_3 stabilized ZrO_2 /CoCrAlY seal system evaluated for 1589K (2400F) applications under contract NAS3-18565 was selected, for further development and characterization. Abradability, erosion and thermal fatigue rig tests of the baseline sprayed ZrO_2 /CoCrAlY seal system were performed under simulated engine conditions. Results indicated satisfactory abradability and erosion resistance and encouraging thermal fatigue performance.

Use of a 12-bladed rotor for the abradability tests resulted in better than an order of magnitude improvement in blade tip to seal volume wear ratio (VWR) over the performance with a single bladed rotor demonstrated under NAS3-18565. A strong sensitivity to the incursion rate between the seal and the rotor was demonstrated, with an optimum rate of approximately 0.0254 mm/sec (0.001 in/sec).

Erosion rates showed a strong dependence on average impingement angle. Test results correlated very well with Bitter's equation for brittle materials. Erosion rates increased as a function of increasing impingement angle. Extrapolated erosion rate at 45 degrees correlates well with other non-metallic seal materials (sintered NiCoCrAlY and plasma sprayed CoCrAlY) previously evaluated by P&WA.

Thermal fatigue tests results were encouraging in that all specimens survived 100 simulated engine idle-sea level takeoff-idle cycles without spallation of the ZrO_2 /CoCrAlY coating. Radial cracks were observed on the ZrO_2 surface within the first few thermal cycles. Laminar cracks were masked by the specimen holding fixture and, therefore, could not be observed until post test disassembly. Abradability and erosion specimens which were fabricated under contract NAS3-18565 demonstrated somewhat better thermal fatigue resistance than similar specimens fabricated under this program. Although similar cracks developed in specimens from both contracts, radial cracking did not initiate until approximately midway through the test in the NAS3-18565 specimens. Metallography of a specimen from each contract showed that radial cracks initiated at the surface and extended through the ZrO_2 layer to or slightly below the interface with the ZrO_2 /CoCrAlY intermediate layer. The extent of cracking in the NAS3-18565 specimen was less than in the specimen fabricated under this program. Laminar cracks occurred at or slightly below the ZrO_2 layer interface in both specimens and joined some of the radial cracks in the specimen from this program. Microstructural and thickness differences in the ZrO_2 layers were identified which may have contributed to the performance differences noted. Processing variations which may have caused the microstructural variations were also identified.

Plasma spray process modifications aimed at producing an increased porosity ZrO_2 surface layer to improve abradability of the baseline system were defined experimentally. Spray parameters to produce an increase porosity surface layer were utilized to spray a nominally 0.635 mm (0.025 in.) thick layer on selected baseline specimens for abradability and erosion rig tests. Abradability and erosion test results, and metallography proved that the attempt to produce an increased porosity surface layer was not very effective.

Modulus of elasticity, ultimate tensile strength and strain to failure, thermal expansion coefficient, thermal conductivity, thermal stability, and residual stress state in an as-sprayed erosion specimen were measured. Modulus of elasticity and ultimate tensile strength were observed to decrease with increasing temperature for some of the $\text{ZrO}_2/\text{CoCrAlY}$ layers, and increase for others. All layers were found to be dimensionally unstable at elevated temperature, especially during the first 20 or 30 hours. The ZrO_2 layer exhibited shrinkage due to sintering (Also noted during thermal coefficient of expansion tests.) The $\text{ZrO}_2/\text{CoCrAlY}$ layers exhibited growth due to oxidation of the CoCrAlY. Residual stresses up to approximately 73% of the measured average ultimate strength of the material were indicated in the as-sprayed erosion specimen.

The steady state and transient thermal stress distributions in the abrasability specimen for the measured thermal fatigue test cycle and specimen layer thicknesses were calculated using measured properties and existing P&WA computer programs. Local stresses were compared with local material strength and used as the basis for crack initiation predictions. These analytical predictions correlated well with experimental results with regard to radial cracking. Laminar cracking, however, was not predicted and could have been caused by combined residual and thermal stresses, edge defects, thermal instabilities and/or geometry variations such as pyramiding. Residual stresses and the effects of thermal instabilities and geometry variations such as pyramiding at the edges of the coating were not incorporated in the analysis.

Analysis of the baseline $\text{ZrO}_2/\text{CoCrAlY}$ seal system in a typical gas turbine engine configuration physically larger than test specimen size showed similar but somewhat higher maximum stress distributions. Therefore, similar performance would be predicted for the engine application.

A seal geometry optimization study was conducted to identify the layer thicknesses, to minimize thermal stresses in the abrasability specimen. Results indicated that, although thermal stresses in the ZrO_2 layer can be reduced significantly by thickness optimization, they cannot be reduced sufficiently to eliminate the probability of tensile stress cracking. The most promising configuration was selected with the approval of the NASA Project Manager and fabricated for abrasability, erosion and thermal fatigue testing and metallographic evaluation. The surface hardness of these specimens was slightly less than the baseline system hardness and seems to correlate with abrasability and erosion test results. Abrasability was slightly improved and erosion resistance was slightly reduced compared to the baseline system. Both optimized configuration specimens subjected to thermal fatigue testing, successfully survived 100 cycles without coating spallation. Radial cracking was less severe in the optimized specimen than in the baseline specimen and generally only propagated partially through the ZrO_2 layer. Laminar cracking initiated in the pyramiding at the edge of the optimized specimen and propagated along the ZrO_2 layer interface only a short distance. Microstructural evaluation indicated generally good correlation with previous specimens. Control of the ZrO_2 layer thickness varied somewhat and the average thickness was greater than targeted.

An analytical study of crack propagation in the sprayed $\text{ZrO}_2/\text{CoCrAlY}$ seal system was conducted. This study included; 1) a literature review to identify applicable, theory, 2) analytical application of the theory to define improvements to the sprayed $\text{ZrO}_2/\text{CoCrAlY}$ seal system to increase crack initiation and propagation resistance, and 3) definition of approaches to implement and evaluate methods of inhibiting crack initiation and growth and substantiating postulated crack growth mechanisms. Although they might ultimately hold potential for developing crack propagation resistant ceramic structures, none of the cyclic crack growth mechanisms proposed in the technical literature provided a suitable basis for predicting cyclic crack growth phenomena. A new mechanism, cyclic crack interaction, is proposed to explain cyclic crack growth observed experimentally during thermal fatigue tests. Analysis of the baseline seal system based on the Griffith criterion ⁽³⁴⁾ as applied by Irwin ⁽³⁵⁾ for crack growth in brittle materials, i.e.; crack tip stress intensity factor equals or exceeds the critical stress intensity factor for the material, indicates that in the first thermal cycle cracks would be expected to initiate at the ZrO_2 layer surface and propagate radially through the ZrO_2 layer into the intermediate layer where it will stabilize or turn and propagate along or parallel to the ZrO_2 layer interface, depending upon the local flaws encountered. Further thermal cycling would propagate these cracks or initiate new cracks by the cyclic crack interaction mechanism. Applicability of these mechanisms to the sprayed $\text{ZrO}_2/\text{CoCrAlY}$ seal system must be experimentally verified.

Various nonhomogeneities were considered as methods of inhibiting crack initiation and propagation in the ZrO_2 layer. Second phase particles show the best potential of those nonhomogeneities considered. However, modification of the seal system fabrication processing to eliminate tensile thermal stresses by generating compressive prestresses is believed to offer the best prospects for success. In any case, pursuit of microstructural modifications to inhibit crack initiation and propagation should be postponed until the proposed crack propagation model has been substantiated.

1.2 CONCLUSIONS

In general, the results of this program indicated that the abrasability and erosion resistance of the sprayed $\text{ZrO}_2/\text{CoCrAlY}$ seal system is acceptable and improvement to the thermal fatigue resistance is required. Improvement can be realized by optimizing the coating layer thicknesses to minimize thermal stresses but not sufficient to eliminate tensile stress cracking in the ZrO_2 layer. However, experimental test results indicate that radial cracks can be arrested in the ZrO_2 layer by design of the seal system and that laminar cracks may not be extensions of the radial cracks.

Residual stresses in the sprayed materials are tensile and are believed to be contributing to the tensile stress cracking observed during thermal fatigue testing. Processing modifications to generate compressive residual stresses in the sprayed coating are considered feasible and would be expected to improve the thermal fatigue resistance of the seal system.

Present analytical methods satisfactorily predict radial cracking initiation but do not predict laminar cracking observed experimentally. Further effort to identify and eliminate the cause of the laminar cracking is required. Since coating pyramiding at the specimen edges is one possible cause, the edges of all future thermal fatigue specimens should be machined to eliminate this factor. Other factors not currently accounted for in the analysis are the effects of residual stresses and dimensional instabilities, interlayer bond strengths, material properties degradation due to thermal aging, and surface temperature variation.

Considerable effort will be necessary to develop and substantiate a reliable life prediction system for the sprayed $\text{ZrO}_2/\text{CoCrAlY}$ seal system. Since both experimental and analytical results presently indicate seal system cracking during the initial or first few cycles, efforts should first be directed toward eliminating crack initiation prior to tackling the long term life prediction task.

2.0 RECOMMENDATIONS

The plasma sprayed $\text{ZrO}_2/\text{CoCrAlY}$ seal system evaluated in this program demonstrated reasonably good abrasability and erosion characteristics and an encouraging degree of cyclic thermal stress tolerance. The potential for further improvement of thermal fatigue resistance was demonstrated by the "optimized configuration" test results. Substantial properties data, which would have to be duplicated for any substitute system, were obtained and permit use of existing analytical tools to predict the effect of seal system modifications. Therefore, continued development of this basic system to obtain an acceptable level of thermal fatigue resistance is recommended as the most effective approach to meeting the long range goals of this effort.

Further optimization to reduce thermal stresses to an absolute minimum and processing modification to create compressive prestress to offset tensile thermal stresses are recommended. Continuation of the optimization study initiated under this program to evaluate the effect of layer thickness modifications on thermal stresses in both the axial and circumferential planes and to investigate changing the ratio of the mixed $\text{ZrO}_2/\text{CoCrAlY}$ layers component materials to vary properties is recommended as the next step. Sufficient information to permit estimation of properties for spray powder materials with different weight ratios of ZrO_2 and CoCrAlY than used in the baseline system was obtained in this program.

In combination with geometric and material optimization efforts to reduce thermal stresses (both stress level and stress range) processing modifications to create compressive residual stresses to offset tensile thermal stresses and maintain a reasonable safety margin between maximum thermal stresses and material strength is recommended. This would be expected to prevent crack initiation and is, therefore, considered the most promising approach to increasing thermal fatigue resistance of the sprayed $\text{ZrO}_2/\text{CoCrAlY}$ seal system. Three methods of creating compressive residual stresses in the sprayed coating are considered feasible: 1) preheating the substrate and maintaining the seal at an elevated temperature while spraying, 2) mechanically prestressing the metal substrate while spraying, and 3) heat treating the seal after fabrication to relax out initial residual stresses and establish a stress free temperature or temperature gradient. Analytical evaluation and selection of the most promising method in combination with the optimized seal design for fabrication and experimental evaluation is recommended. To accomplish this, it will be necessary to establish a procedure for estimating the residual stresses and the combined residual and thermal stresses at operating cycle points.

Continued development of a life prediction system for sprayed ceramic/metal seal systems should also be pursued.

3.0 INTRODUCTION

3.1 BACKGROUND

Gas path sealing is a proven and accepted method of improving gas turbine engine performance and, thereby, reducing fuel consumption. Generally, the turbine section of the engine presents the greatest potential for efficiency gains through the use of gas path sealing.

Turbine abradable gas path seals perform two primary functions: 1) permits operation at minimum clearances by reducing the potential of rotor damage during rotor-seal interactions, and 2) protects critical turbine parts from excessive temperatures by providing a thermal barrier between the hot turbine gas and the turbine static structure.

Gas turbine engine development trends are toward higher turbine inlet temperatures (TIT) to obtain improved performance with minimum engine size and weight. Projections indicate that growth versions of current commercial aircraft engines will approach 1811K (2800F) TIT, while future engine generations for the 1980's will approach 2033K (3200F). High pressure compressor bleed air is used to cool the turbine gas path seals to maintain them within acceptable material operating temperature limits. This results in an engine performance penalty due to the loss of high pressure air from the cycle. Seal materials with increased temperature capability will permit reduction in cooling air requirements and result in improved engine efficiency. If the thermal conductivity of the gas path seal is sufficiently low, so that the supporting structure is thermally protected and requires less cooling, further reductions in cooling air requirements with attendant engine efficiency improvements can also be realized. In this situation, significant cost reductions may also be affected in the seal support structure because of the possible use of lower temperature, less expensive materials and less sophisticated engines.

Reduced operating clearances limit the loss of high energy, high pressure gas from the main gas path without extracting useful work from it (reduced leakage), thereby, resulting in increased turbine efficiency. Current estimates for a typical commercial gas turbine engine are that a 0.254 millimeter (0.010 inch) reduction in first stage high pressure turbine blade tip average operating clearance would result in approximately one percent increase in turbine efficiency.

Reduced operating clearances will result in inadvertent rubs between the turbine rotor and static gas path seal components due to differential heating and cooling rates, case distortions such as ovalization due to circumferential heat flux variations and imposed loads, and rotor shift or bending. The seal must be capable of tolerating these rubs without catastrophic failure such as blade destruction. The gas path seal component should be abradable to wear preferably during rotor seal interaction to minimize the effect of a rub on average operating clearance by restricting the clearance increase to the local rubbed arc area.

Turbine gas path seals must also be capable of withstanding exposure to the scrubbing action of the high temperature gas and entrained particulate matter, such as ingested dirt and dust, wear debris and unburned carbon, without excessive degradation caused by oxidation or erosion for the life cycle of the seal. The durability of the seal to withstand the harsh turbine

environment not only affects its replacement rate, but also extends the life of other related critical turbine parts and, therefore, can reduce overhaul and maintenance costs considerably.

Ceramic materials offer the high temperature and insulation capability required for turbine outer air seal application. Of all the alternative approaches, the one offering the most benefits is the sprayed concept. The sprayed concept is more flexible and less costly than other concepts such as a sintered ceramic braze bonded to a metal substrate. An additional benefit is the possibility of repair and/or refurbishment directly at an overhaul facility using existing spray facilities.

The sprayed Y_2O_3 stabilized $ZrO_2/CoCrAlY$ seal systems evaluated under NASA Contract NAS3-18565⁽¹⁾ demonstrated promise for 189K (2400F) applications but required further development and evaluation. Two spray processes, layered and continuously graded, and the addition of CeO_2 to each process as a solid high temperature lubricant were evaluated. All four systems demonstrated the capability of operating at surface temperatures up to 1589K (2400F) during abrasability and erosion tests without evidence of any thermal distress. Hot particulate erosion rates compared favorably with other seal systems evaluated by P&WA under in-house and other contractual programs. Some slight grooving of the seal surface occurred during abrasability testing indicating that a desired degree of abrasability might be provided with additional modification. The CeO_2 additive did not have any discernable effect on the abrasability of these seal systems.

The effort described in this report, which was conducted under contract NAS3-19759, is a continuation of the effort to develop abrasable gas path seals for gas turbine engines. Previous effort conducted in 1975⁽¹⁾ and 1974⁽²⁾ evaluated the abrasability and erosion characteristics of several seal systems for use in 1144-1366K (1600-2000F) applications and initiated evaluation of selected seal systems with 1366-1589K (2000-2400F) capability.

3.2 PROGRAM OBJECTIVE

The long range goal of the effort reported herein is development of a durable abrasable blade tip seal material system capable of gas turbine engine operation at seal surface temperatures up to 1589K (2400F). Specific objectives of this program were to define the capability of a sprayed graded zirconia/metal turbine blade tip seal system and develop the technology required to identify the pertinent elements of, and make recommendations for, a long range program to substantiate the sprayed ceramic seal system for engine applications.

3.3 APPROACH

One of the four plasma sprayed graded Y_2O_3 stabilized $ZrO_2/CoCrAlY$ seal systems evaluated under contract NAS3-18565 which demonstrated the greatest potential for successful engine applications up to 1589K (2400F) seal surface temperature was selected, with the approval of the NASA Project Manager, for further evaluation and development. Abrasability, erosion and thermal fatigue characteristics of the selected seal system were evaluated by rig testing under simulated engine conditions. Plasma spray process modifications to increase the ZrO_2 surface porosity in an attempt to improve abrasability were investigated. The most

promising process change was selected, specimens were fabricated, and abrasability and erosion characteristics were evaluated by rig testing. Post test metallography was utilized to evaluate microstructural characteristics of the sprayed seal materials and phenomena such as crack initiation sites and extent of cracking in the seal, extent of blade tip metal transfer to the seal during rub interaction, and evidence of densification of the abrasable surface.

Physical and mechanical properties of the sprayed seal materials, long term thermal exposure effects on weight and dimensional stability and residual stress were also determined.

Thermal shock capability of the rub specimen for the thermal cycle used in the cyclic thermal stress tests was analyzed using existing P&WA analytical programs and the materials properties measured during this program. Analytical predictions were correlated with rig test results.

Applicability of the selected seal system to an engine application, which was selected jointly by NASA and P&WA, was assessed analytically. Recommendations for further development to substantiate use of this seal system for the specific engine application were formulated and discussed with the NASA Project Manager.

Analyses to optimize the layer thicknesses to minimize thermal stresses were performed. The resulting seal system configuration was fabricated and rig tested to evaluate abrasability, erosion and thermal fatigue characteristics. Metallography was utilized to verify the actual configuration and microstructural characteristics obtained and the probable initiation sites and extent of thermal stress cracking. Analysis and test results were then correlated to assess the accuracy of the analysis.

The applicability of cyclic crack propagation theory to the sprayed ZrO_2 seal system was evaluated and an experimental approach to investigate crack propagation was defined. Possible microstructural improvements to the sprayed structure to increase cyclic crack propagation resistance were also identified.

4.0 TECHNICAL PROGRAM

4.1 SEAL SELECTION

The sprayed graded layered Y_2O_3 stabilized ZrO_2 /CoCrAlY seal system shown in Figure 1 was selected, with the approval of the NASA Project Manager, for further evaluation under this contract. Selection was based on the following considerations:

1. Preliminary results from contract NAS3-18565 indicated:
 - a. The CeO_2 additive, intended to improve rub tolerance of the ZrO_2 , had no significant effect on abrasability or erosion resistance,
 - b. For all practical purposes, abrasability of both the sprayed graded layered and sprayed continuously graded Y_2O_3 - ZrO_2 /CoCrAlY seal systems were equivalent; both systems exhibited slight grooving during abrasability tests,
 - c. Both systems withstood ZrO_2 surface temperatures up to 1589K (2400F) without apparent distress.
2. The sprayed graded layered Y_2O_3 - ZrO_2 /CoCrAlY seal system does not involve spray processes which are proprietary to the fabricator. This permits more positive control and better understanding of the system.
3. Significant improvement in abrasability was demonstrated by using a 12-bladed rotor instead of the single bladed rotor used for NAS3-18565. The 12-bladed rotor more closely simulates engine rub parameters such as blade passing frequency and chip thickness (as shown in Table I) and the post test appearance of rub tested specimens more closely resemble rubbed engine hardware. Rig tests using 12 blades have demonstrated improved abrasability of an order of magnitude or more as compared to single bladed test results.

In addition to the baseline system, evaluation of a system with a goal of increased porosity ZrO_2 layer as a method of improving abrasability was included in the program. Two abrasability and one erosion specimens with 0.508-0.762 mm (0.020-0.030 in.) thick additional ZrO_2 layer sprayed with a modified procedure to effect an increased porosity surface layer were fabricated and tested.

A porosity of 50-60% was targeted. Fabrication process modification was considered necessary to achieve this porosity increase. A screening test program consisting of metallographic evaluation of manually sprayed tabs fabricated using various spray parameter variations was used to select spray parameters for fabrication of the increased porosity test specimens. Several variations of two basic approaches, i.e., 1) reduced power level to the spray gun and 2) co-spraying ZrO_2 and iron powder and subsequent leaching out of the iron with dilute nitric acid, was initially evaluated without success. A third method, increased gun stand-off distance, from 12.7 cm (5 in.) to 20.32 cm (8 in.) showed potential for some

increase in porosity and was selected for fabrication of the test specimens. Due to interference of the gun with the spray fixture it was necessary to reduce the spray angle from 90 degrees to approximately 60 degrees to obtain the increased standoff distance.

4.2 PERFORMANCE TESTS

4.2.1 Abradability Tests

The capability to tolerate blade tip rubs without catastrophic failure was evaluated by abradability rig tests. Six tests, four on the baseline sprayed $\text{ZrO}_2/\text{CoCrAlY}$ system and two on the system modified to increase the porosity of the ZrO_2 layer, were conducted under simulated conditions of seal surface temperature, blade tip speed and incursion rate combinations indicated in Table II.

One additional test on a seal system specimen optimized with respect to geometry to reduce thermal stresses was also conducted and will be discussed in a later section of this report.

All abradability tests were performed with P&WA's high temperature abradability test rig shown in Figure 2. Simulated turbine blade tips were mounted in the periphery of a disk driven at the required speed by a compressed air turbine. The seal segment specimen was mounted in a fixture at the end of a horizontal post attached to a moveable carriage assembly. The carriage assembly injects the specimen radially into the rotor assembly at the required incursion rate. The seal specimen was heated from both sides of the rotor by oxygen-acetylene torches directed at the seal surface. Heating torches were also mounted off the carriage assembly. Firing rate and distance between the torches and seal specimen was varied to control the seal surface temperature.

Seal surface temperature and blade tip temperature were monitored by optical pyrometers. Carriage travel was monitored by a linear differential transformer. A load cell in the carriage feed system permitted determination of the average normal force between the seal specimen and blade tips. All data were recorded continuously on a strip chart.

Blade tip and seal wear was determined through pre and post test measurements. Relative abradability between different specimens and different seal systems was assessed on the basis of the volume wear ratio (VWR); the blade tip wear volume divided by the seal wear volume. The smaller the volume wear ratio, the better the abradability of the seal system.

In order to simulate typical engine rub conditions more closely, as discussed earlier, a twelve-bladed rotor was used for abradability tests under this contract instead of the single-bladed rotor used for testing under contract NAS3-18565. Replaceable blades cast out of B-1900, a nickel base high temperature turbine blade alloy, were mounted in the periphery of a test rig disk and ground to uniform tip radius prior to testing. The tips of these blades were nominally 6.35 mm (0.25 in.) wide by 3.175 mm (0.125 in.) thick.

Abradability test results are summarized in Table III. The initial test in this sequence was scheduled to be at 1366K (2000F) and 304.9 m/sec (1000 ft/sec). The windage produced by

the twelve-bladed rotor necessitated reducing rotor speed to 249.9 m/sec (820 ft/sec) to obtain a 1366K (2000F) seal surface temperature. Analysis of the rig set up offered possible approaches to increasing the temperature-speed capacity with the twelve-bladed rotor. The most promising approach, shortening the rotor blades, was incorporated and resulted in successfully meeting the maximum temperature and speed requirements of subsequent tests without further difficulty.

Test results summarized in Table III indicate:

1. Abradability of the sprayed $ZrO_2/CoCrAlY$ seal system is highly sensitive to incursion rate as shown in Figure 3. An optimum incursion rate for minimum blade tip wear and blade tip metal transfer to the seal and maximum seal grooving occurs in the vicinity of 0.0254 mm/sec (0.001 in. sec). Greater blade tip wear and transfer occurred at both lower and high incursion rates. The maximum incursion rate of 0.254 mm/sec (0.010 in/sec) was most severe in that maximum blade tip wear and transfer and no seal grooving occurred. At the slower incursion rate, 0.0025 mm/sec (0.0001 in/sec), some seal grooving resulted initially and was followed by blade tip transfer.
2. A possible sensitivity to temperature level is also indicated by test No. 1. An unusual blade wear pattern shown in Figure 4 occurred which may identify a dependence of abradability on seal temperature. One side of the blade wore significantly more than the other, 1.143 mm (0.045 in.) and 0.127 mm (0.005 in.), respectively. Visual examination of the seal specimen, Figure 5, indicates that the side of the seal which grooved deeply (minimum blade tip wear) was significantly hotter than the side which wore the blade heavily. The variation in seal surface heating is attributed to the difficulty in adjusting the heating torches due to excessive blade tip windage. (Surface temperatures were more uniform in subsequent tests using shorter blades.) The magnitude of temperature difference is unknown because the pyrometer monitoring seal surface temperature was focused on the transition area between the deep and shallow grooves and was, therefore, probably measuring some average value. Additional testing would be required to substantiate the relationship between temperature and abradability.
3. Axial cracks shown in Figure 6 were present in the blade material transfer in the rub path. Some of these cracks did not extend to the edges of the specimens. As a result, it is suspected that the transfer of blade material, because of thermal stresses and/or mechanical forces during the rub interaction, is a site of crack initiation. It is, therefore, desirable to reduce and/or eliminate blade material transfer to the seal segment. This can be accomplished by use of suitable blade tip treatment.
4. Results of testing the specimens fabricated by a modified process in the expectation to produce a more porous structure, showed no discernable improvement in abradability. (Metallograph results discussed later in this report indicated there was no discernable increase in porosity.)

5. As expected, use of the 12-bladed rotor greatly improved abrasability. The actual improvement, assuming no variation in the sprayed system, was a factor of 8.

The blade tips picked up metal deposits on the leading side near the tip as shown in Figure 7, apparently from plowing the transferred material off the seal. The amount of these deposits varied proportionately to the amount of transferred material on the seal and therefore, the severity of the test conditions.

Downstream of the rubbed area on the seal specimen, metal particles, which were apparently sprayed off the blade tips in a semi-molten state by centrifugal action, were deposited on the seal surface as shown in Figure 8. Again the amount varied proportionately to the amount of transfer to the seal in the rubbed area.

The specimen shown in Figure 6 was sectioned in the axial and circumferential direction and metallographically examined. This specimen incorporated the increased porosity surface layer and was tested at 1589K (2400F), 304.8 m/sec (1000 ft/sec) and 0.0254 mm/sec (0.001 in/sec) (Abradability Test No. 3). Metallographic observations are summarized as follows:

1. Small amounts of blade tip residue were seen on the sections of the rub path which were examined. Deposit thicknesses up to approximately 0.0051 mm (0.0002 in.) were found as shown in Figure 9 (a).
2. Some apparent densification of the ceramic layer at the rub path surface extending to a depth of 0.0508-0.1016 mm (0.002-0.004 in.) occurred as shown in Figure 9(a) and (b). This may partially account for the change in mechanism from grooving the seal to blade tip wear and transfer.
3. The increased porosity ZrO_2 surface layer could not be distinguished from the baseline ceramic layer. This correlates with hardness measurements and abrasability and erosion data which indicate that efforts to produce an increased porosity ZrO_2 surface layer were unsuccessful.
4. Layer homogeneity was considered good. Areas of increased density or porosity were not detected in the sections analyzed. Metallic distribution in the intermediate layers appeared uniform.
5. Most cracks present on the surface propagated from the surface through the ZrO_2 layer and into the composite $ZrO_2/CoCrAlY$ layer to a depth of approximately 0.203 mm (0.008 in.). Some cracks stopped in the ZrO_2 layer at the interface with the composite layer. Typical cracks are shown in Figure 10. The presence of a few cracks outside the rub path indicate that a mechanism in addition to that postulated with reference to the blade material transfer as proposed earlier was active, possibly thermal stress rupture.

4.2.2 Erosion Tests

Erosion resistance of the sprayed $\text{ZrO}_2/\text{CoCrAlY}$ seal system was evaluated by hot particulate rig testing at various impingement angles and temperatures as shown in Table IV. Three specimens with the baseline coating and one with the additional ZrO_2 layer sprayed to produce a more porous structure were tested.

Erosion tests were performed in the hot particulate erosion rig shown in Figure 11. The specimen was positioned at the specified distance and impingement angle relative to the end of the combustor exit nozzle by a compound vise. The specimen was heated by impinging JP fuel and air combustion products on the ZrO_2 surface of the specimen through a 1.905 cm (0.75 in) diameter exit nozzle. Specimen temperature and exit gas velocity were controlled by varying fuel and air flows. During initial startup of the combustor the specimen was positioned out of the hot gas stream. It was slowly moved into the hot gas stream in a manner designed to minimize thermal shock to a predetermined position after the combustor was stabilized. Final adjustments to obtain the specified seal temperature and exit gas velocity were made after the specimen was in the final position.

After the specimen temperature and gas velocity were stabilized, particulate flow was initiated. The particulate matter was gravity fed into a tube connected into the combustor exit nozzle approximately 5.08 cm (2 in.) upstream of the nozzle end where it was picked up and accelerated to the specimen surface by the hot gas stream. Particulate flow rate was controlled by a precalibrated orifice in the storage hopper discharge line. The weight of particulate used and the duration of particulate flow during the test was monitored to check the particulate flow rate.

Specimen temperature was measured optically on the ZrO_2 and metal substrate surfaces. Erosion wear was determined by measuring the weight loss of the specimen at five minute intervals.

The erosion specimen shown in Figure 12 consists of the composite coating system sprayed on a flat Hastelloy X plate nominally 3.81 by 5.08 by 0.254 cm (1.5 by 2.0 by 0.1 in.). A 3.81 cm^2 (1.5 in^2) a section of the substrate is coated, leaving a 1.27 cm (0.5 in.) uncoated end for mounting in the test fixture.

Test conditions and results are summarized in Table V. Test results on the optimized seal configuration are included in Table V, but will be discussed later. Post test photographs of the baseline and "increased porosity" specimens are shown in Figure 13. Data presented in Table V indicate that both surface temperature and impingement angle have a significant effect upon erosion rate. The specimen tested at 1366K (2000F) and 15 degrees impingement angle (Test No. 1) exhibited an erosion rate approximately six times greater than specimens tested at 1589K (2400F) at the same impingement angle (Tests No.'s 2, 3 and 5). The specimen tested at 1589K (2400F) and 90 degrees impingement angle (Test No. 4) exhibited an erosion rate approximately 20 times greater than specimens tested at the same temperature and 15 degrees impingement angle (Tests No.'s 2, 3 and 5). As would be expected based on the microstructural evaluation of the abrasability specimen discussed earlier, the erosion rate was not significantly different between the baseline and the specimens fabricated with the intent to increase porosity (Test No's 2 and 3).

A simplification of Bitter's equation (3), given below, was used to investigate erosion results.

$$Q = \frac{1/2 M(V_{\sin \alpha} - K)^2}{\epsilon}$$

where: Q = wear due to repeated deformation -- cm^3
 M = total mass of impinging particles -- $\text{gf-sec}^2/\text{cm}$
 V = particle velocity before collision -- cm/sec
 K = constant related to target properties -- cm/sec
 α = impingement angle
 ϵ = deformation wear factor

For simplification K was assumed to be negligible in comparison to particle velocity -- an assumption substantiated in the literature, reference (4). With this assumption the equation correlates well with the 1589K (2400F) data obtained under this contract as shown in Figure 14. The quantity $MV^2/2$ was evaluated at the 90 degree point by equating it to the measured erosion rate. Data measured at 1366K (2000F) under this contract and at 1589K (2400F) under contract NAS3-18565 are shown for information. Also the range of other high temperature seal systems such as sintered NiCoCrAlY and plasma sprayed CoCrAlY evaluated by P&WA under in-house programs is indicated. The cause of the large scatter in the 1589K (2400F) data at 15 degrees is not known but there are several possible explanations. They are: 1) batch to batch reproducibility of the sprayed ZrO_2 structure, 2) weight loss measurement error due to partial delamination of the coating during testing of the NAS3-18565 specimen, or 3) a tendency toward ductile behavior. One or both of the first two are considered most likely since three out of four data points correlate very closely.

Generally speaking, the erosion resistance of the sprayed $\text{ZrO}_2/\text{CoCrAlY}$ seal system appears to be marginally satisfactory for engine application. Some improvement is desirable if it can be obtained without much sacrifice in abrasability or thermal fatigue resistance.

4.2.3 Thermal Fatigue Tests

The durability of the sprayed $\text{ZrO}_2/\text{CoCrAlY}$ seal system in an engine application will depend greatly on its capability to successfully survive the initial and subsequent thermal cycles corresponding to the engine operational conditions. This is the most difficult parameter to satisfy with a ceramic seal because of the relatively low strength (especially tensile strength) of ceramic materials and the large mismatch in thermal growth between ceramic and metallic materials. The graded, layered system was selected specifically to modify the layer difference in thermal expansion between the metal substrate and ceramic. Thermal and mechanical properties of each of the individual layers in the graded $\text{ZrO}_2/\text{CoCrAlY}$ structure and the metal substrate as well as the geometry of the seal segment affect the thermal stresses generated during thermal cycling.

Thermal fatigue characteristics were evaluated by rig tests which subject seal specimens to a simulated gas turbine engine thermal cycle from idle to sea level takeoff (SLTO) and back to idle. Appropriate temperatures are maintained on the ZrO_2 surface and the back of the substrate. Typical cycles are shown in Figures 15 and 16 for abrasability and erosion specimen configurations. The "proposed" or engine cycle is the same for both specimens. The actual temperature obtained, however, varied somewhat between the abrasability and erosion specimen largely because of the specimen geometry.

The thermal fatigue test rig is shown in Figure 17. The specimen was mounted in a water cooled copper fixture. A combination of oxygen-propane torches and cooling air jets were used to achieve the desired thermal cycles on the ZrO_2 and metal substrate surfaces. The torches were mechanically moved toward or away from the specimen at controlled rates to provide the required thermal cycle. Fixed cooling air jets were turned on or off or the flow was changed at predetermined intervals to meet the cycle requirements.

The ZrO_2 and metal substrate surface temperatures were monitored continuously with an optical pyrometer and thermocouples, respectively, and recorded on a strip chart.

Three abrasability and two erosion specimens of the baseline sprayed graded $ZrO_2/CoCrAlY$ seal system were tested. Test conditions and results are summarized in Table VI. All specimens tested completed 100 cycles without gross failure (delamination). However, all specimens exhibited both radial and laminar cracking as shown in Figures 18 through 22.

The specimens used in tests 1, 2 and 4 were fabricated under this contract. Tests 1 and 2 resulted in nearly identical results. Radial cracks were visible on the surfaces of both specimens in less than 15 cycles and tended to become progressively more pronounced as the test proceeded. Post test visual inspection indicated extensive laminar cracking in the vicinity of the ZrO_2 layer interface. Since interfacial cracking cannot be observed during testing because it is masked by the specimen holding fixture, the point in the thermal cycle at which laminar cracking initiated could not be identified.

The specimen used to set the thermal cycle parameters and check operation of the test rig was residual from contract NAS3-18565 and had the same sprayed seal system. It had survived 35 varied thermal cycles, several of which were more severe than the test cycle, without any visually detectable radial or laminar cracking. In an attempt to obtain data with respect to system repeatability it was decided, with the approval of the NASA Project Manager, to continue testing on this specimen to 100 cycles as the third abrasability specimen test. Hairline radial cracks became apparent on the surface after approximately 50 cycles, but did not appear to expand as the test proceeded as did the first two specimens. Post test visual inspection also revealed hairline laminar cracks in the vicinity of the ZrO_2 layer interface.

Results on the first erosion specimen, test No. 4, was similar to the results from the first two abrasability specimens. Therefore, a specimen fabricated under the previous contract was used for the second erosion specimen, test No. 5. Results on this specimen were similar to those from the abrasability specimen fabricated under NAS3-18565, test No. 3.

The test results indicated a discernable difference in thermal fatigue resistance between the specimens fabricated under this contract and those fabricated earlier under NAS3-18565. Hence, metallographic analysis of one specimen fabricated under each contract, to attempt to identify the cause of the difference in thermal fatigue resistance, was conducted. Fabrication processing differences were also investigated.

The following microstructural differences were determined and are considered potentially significant:

1. The ZrO_2 and 70/30 $ZrO_2/CoCrAlY$ layers of the NAS3-18565 specimens were approximately 0.254 mm(0.010 in.) thinner than for the current contract specimens as shown in Table VII. Other layers were nearly the same thicknesses.
2. The specimen fabricated under the previous contract exhibited larger ZrO_2 layer agglomerate size than the specimen from this contract as shown by comparison of Figures 23 and 24. Microstructure of other layers was essentially identical.
3. The average pore size in the ZrO_2 layer of the previous contract specimen was larger than the pore size of the current specimen. However, the total pore fraction and metal fraction of all layers of both specimens were very nearly the same as shown in Table VIII.

The following variations in spray processing were determined:

1. Coating deposition rates for the NAS3-18565 specimens were 2 to 2.5 times the deposition rates of the current contract specimens. A review of possible causes led to the belief that powder feed port wear was responsible and procedures were instituted to more closely control this variable.
2. Delay times between coating layers varied by as much as a factor of two but were not consistently different in one direction for all layers of either specimen lot. In fact, the average delay times were within 15 seconds of each other.
3. The number of interruptions in spraying to measure coating thickness were the same except for the top ceramic layer. This layer had two more interruptions for the current specimens than for the NAS3-18565 specimens.
4. Powder lots, spray gun electrodes and spray gun operators were different.

The observed microstructural differences could have been caused by the variations in the spray process and could also have significantly effected thermal fatigue resistance parameters such as residual stress and physical and mechanical properties.

Cracks in both specimens appeared to initiate at the surface and to propagate intergranularly through the ZrO_2 layer. Most cracks reached the interface with the ZrO_2 /CoCrAlY composite layers and were either arrested or redirected parallel to the interface in the ZrO_2 layer. It was not clear whether laminar cracks were extensions of the radial cracks or had initiated at the edge and propagated in to join the radial cracks.

4.3 MATERIALS PROPERTIES

The most cost and time effective approach to high temperature ceramic seal development involves thermal and structural analysis of the preliminary design of the seal system with subsequent substantiation by selected testing. This approach minimizes the requirement for time consuming, expensive "build & try" tests. It also provides an insight into the interrelationship between environmental temperature and seal geometry factors which reduces the probability of 1) preserving a concept which ultimately would prove unsatisfactory in an engine or 2) eliminating a potentially good engine system on the basis of failure during rig test. However, key to this approach is a thorough knowledge of the properties of the seal system materials and an accurate modeling technique. Material properties are discussed in this section, analytical modeling in Section 4.4.

Material properties necessary for thermal and structural analysis and evaluation of the effects of rig tests on the sprayed ZrO_2 /CoCrAlY seal system were measured. Measured properties included thermal stability and initial residual stress state of the as-sprayed baseline ZrO_2 /CoCrAlY seal system.

4.3.1 Physical and Mechanical Properties

Hardness of the ZrO_2 surface layer, thermal expansion characteristics of each sprayed material layer, thermal conductivity of the ZrO_2 layer and of the total composite seal system, moduli of elasticity and rupture, and strain to failure for each sprayed material layer were measured.

4.3.1.1 Hardness

The Superficial Rockwell 45Y hardness was measured on the abradable ZrO_2 surface of all abradability and erosion specimens. Experience has indicated that this property may prove to be a good non-destructive indicator of coating quality, abradability and erosion characteristics, and/or material strength. It is a quick and relatively inexpensive test to perform.

Measurements were taken on the as-sprayed surface at six locations on the erosion specimens and ten locations on the abradability specimen. All locations were outside the areas expected to be affected by subsequent testing to minimize the possibility of effects on the test results.

Average hardnesses of abrasability specimens varied between 72 and 76 with a typical hardness variation of about 12 observed on any given specimen. Average hardness of erosion specimens varied between 64 and 80, again with a typical hardness variation of about 12 observed on any given specimen. The increased porosity specimens showed reduced hardness, about 69 for abrasability specimens and 65 for the erosion specimen. This data indicates good repeatability between the two rings of parts sprayed under this contract and also with parts sprayed under the previous contract, NAS3-18565.

4.3.1.2 Linear Thermal Expansion Coefficient

The linear thermal expansion coefficient was measured for each material layer in the plasma sprayed $\text{ZrO}_2/\text{CoCrAlY}$ seal system in the direction parallel to the spraying direction. Specimens measuring $3.556 \times 0.762 \times 0.254$ cm ($1.4 \times 0.3 \times 0.1$ in.) were machined from thick plasma sprayed deposits of each individual layer which comprise the total seal structure after removing the deposits from their respective mild steel backings by immersion in 50% HNO_3 .

After being accurately measured in the 3.556 cm (1.4 in.) direction (parallel to the spraying direction), the specimens were instrumented with a Netzsch Electronic Automatic Recording Dilatometer. The system was placed in the center zone of a closed chamber which was evacuated and then backfilled with helium. The mixed $\text{ZrO}_2/\text{CoCrAlY}$ specimens were then programmed for temperature rise and equilibrium at 100K (180F) intervals from 293K (68F) to 1073K (1472F) and specimen length and temperature was continuously monitored. An equivalent program for temperature fall and equilibrium was also implemented. The ZrO_2 specimens were scheduled through a similar program up to 1573K (2372F). The mean coefficient of thermal expansion was calculated for each individual layer material using:

$$\alpha = \frac{L_T - L_O}{L_O (T - T_O)}$$

where: α = mean coefficient of thermal expansion from T_O to T
 L_T = measured length at T
 L_O = measured length at T_O
 T = temperature at which measurement was made
 T_O = initial temperature

Results are summarized in Figures 25 through 28. As expected, increasing metal content caused a slight increase in the expansion. The 1073K (1472F) maximum temperature on the $\text{ZrO}_2/\text{CoCrAlY}$ specimens was not high enough to cause detectable amounts of shrinkage due to sintering of the constituents; therefore, no irreversible length changes occurred. Incipient shrinkage did occur in the 100% ZrO_2 specimen above 922K (1200F). This was initially interpreted as warpage of the specimen and resulted in two arrests of the tests. The third cycle, which is plotted in Figure 25, consequently measured the expansion of a partially sintered specimen up to 1589K (2400F) and back down to room temperature. The effect of further sintering in the form of irreversible shrinkage was evident as shown in Figure 25.

4.3.1.3 Thermal Conductivity

Thermal conductivity was measured on samples of the ZrO_2 layer and the complete seal system. The ZrO_2 layer was applied to a 2.54 cm (1 in.) diameter Mar-M-509 backing 0.635 cm (0.25 in.) thick which had been plasma spray coated with a NiCrAl bond coat 0.0762-0.127 mm (0.003-0.005 in.) thick. this specimen was machined to 2.286 cm (0.9 in.) diameter by 0.914 cm (0.36 in.) high cylinder for testing. The complete seal system specimen was machined from an erosion specimen which was sprayed on a Hastelloy-X substrate 0.254 cm (0.1 in.) thick. The specimen was machined to a 2.54 cm (1 in.) diameter by 0.635 cm (0.25 in.) high cylinder.

Both specimens were tested using the comparative cut bar method. A specimen was placed between two Inconel 702 reference standards of known thermal conductivity with thermocouples at the interfaces. The test stack was placed between the plates of an upper heater, auxiliary heater and a lower heat sink. A reproducible load was applied to the top of the complete system to achieve a uniform interface contact. A guard tube which could be heated or cooled was placed around the system and the interspace and surroundings were filled with an insulating powder. By adjusting the heaters and heat sink temperatures, a constant temperature distribution was maintained in the system. Radial heat losses were reduced to negligible values by keeping the guard tube temperature close to the average temperature of the sample. Temperatures at various locations in the system were recorded when equilibrium conditions were attained at average specimen temperatures of 373K (212F), 673K (752F), 1073K (1472F) and 1473K (2192F) during heatup. Measurements were also recorded at 973K (1292F) and 473K (392F) during cool down. The thermal conductivity of each specimen was calculated using:

$$K_s = 1/2 \frac{(X_s)}{(T_s)} \frac{(K_{R1} T_{R1})}{(X_{R1})} + \frac{(K_{R2} T_{R2})}{(X_{R2})}$$

where: K = thermal conductivity
X = thickness
T = temperature difference
S = specimen
R₁ = top reference
R₂ = bottom reference

Thermal conductivities of the sprayed coatings were then calculated using the resistance method:

$$K_c = \frac{X_c}{\frac{X_s}{K_s} - \frac{X_m}{K_m}}$$

where: c = coating
m = substrate

The NiCrAl bond coat was included as part of the substrate material in this calculation. Results are plotted in Figures 29 and 30. The slightly higher conductivities during cool down are indicative of sintering and densification.

Thermal conductivities of the mixed $\text{ZrO}_2/\text{CoCrAlY}$ intermediate layers were estimated from these results by:

1. Calculating the average thermal conductivity of the composite of the three intermediate layers using:

$$K_I = \frac{X_I}{\frac{X_T}{K_T} - \frac{X_c}{K_c}}$$

where: K_I = composite average thermal conductivity of intermediate layers
 K_T = average thermal conductivity of total coating system
 K_c = thermal conductivity of sprayed ZrO_2 layer
 X_I = intermediate layers thickness
 X_T = total coating thickness
 X_c = ZrO_2 layer thickness

2. Plotting the thermal conductivity against intermediate layer thickness assuming:
 - (a) the thermal conductivity at the ZrO_2 layer-intermediate layer interface is equal to the ZrO_2 layer conductivity,
 - (b) the thermal conductivity at the intermediate layer-metal substrate interface is equal to the substrate conductivity, and
 - (c) the thermal conductivity at the mean thickness of the intermediate layers equals K_I calculated in step 1.
3. The thermal conductivity of each of the intermediate layers was taken as the value of the curve drawn through the foregoing points at the center of each layer.

Estimated thermal conductivities for each of the $\text{ZrO}_2/\text{CoCrAlY}$ layers are shown in Figure 31.

4.3.1.4 Moduli of Elasticity and Rupture

Elastic and rupture moduli were determined on specimens representative of each individual layer of the sprayed $\text{ZrO}_2/\text{CoCrAlY}$ seal system by four point flexure testing. A strain gage, placed at mid span and center of each specimen, was used to measure specimen deflection for room temperature tests. Deflectometer measurement of cross-head deflection was used to determine specimen deflection at elevated temperatures. Test specimens measured $0.254 \times 0.762 \times 3.556$ cm ($0.1 \times 0.3 \times 1.4$ in.) and were prepared similar to that previously described for the thermal expansion specimens.

Room temperature tests were performed on specimens representative of each layer. Elevated temperature characteristics were determined at maximum estimated operating temperatures of 1005K (1350F), 1061K (1450F), 1144K (1600F) and 1589K (2400F) for each of the layers; 40/60, 70/30 and 85/15 ZrO₂/CoCrAlY and 100% ZrO₂ respectively.

Modulus of elasticity was calculated using either of the following formulæ as applicable:

For strain gaged specimens:

$$E = \frac{35 (P/\epsilon)}{4 b h^2}$$

where: E = elastic modulus
P/ε = slope of the load versus strain curve
b = specimen width perpendicular to the load application
h = specimen thickness coincident with the load direction.

For elevated temperature tests where the cross head deflection was measured:

$$E = \frac{S^3 (P/\epsilon)}{8 b h^3}$$

where: S = distance between supports
P/ε = slope of the load versus deflection curve

Modulus of rupture was calculated using:

$$\sigma_u = \frac{3 P S}{4 b h^2}$$

where: σ_u = modulus of rupture (bending strength)
P = maximum load prior to specimen failure

Strain to failure was read directly for strain gaged specimens. For deflectometer measured specimens, strain to failure (ε_u) was calculated using:

$$\epsilon_u = \frac{6h X}{(S-a) (S + 2a)}$$

where: a = 1/2 distance between supports (S/2)
X = deflection at load points at failure (deflectometer reading)

Test results are summarized in Table IX. These results indicate:

1. The strength increases as metal content increases.

2. The strength of the 40/60 $\text{ZrO}_2/\text{CoCrAlY}$ layer and the all ZrO_2 layer decreased with increased temperature. The strength of the remaining $\text{ZrO}_2/\text{CoCrAlY}$ layers increased with increased temperature.
3. The elastic modulus of the $\text{ZrO}_2/\text{CoCrAlY}$ layers increased with metal content but was higher for the all ZrO_2 layer than for the 85/15 $\text{ZrO}_2/\text{CoCrAlY}$ layer.
4. The elastic modulus of the all ZrO_2 and the 85/15 $\text{ZrO}_2/\text{CoCrAlY}$ layers decreased with increased temperature while it increased for the remaining $\text{ZrO}_2/\text{CoCrAlY}$ layers.
5. Strain to failure increased with increasing metal content.

The increased strength and/or elastic modulus with increased temperature displayed by some of the mixed $\text{ZrO}_2/\text{CoCrAlY}$ layers has also been observed in polyphase ceramic materials with strong anisotropic expansion properties and may be linked to the occurrence of internal ruptures and recombinations as cited by Buessern⁽⁵⁾.

4.3.2 Thermal Stability

Thermal stability and oxidation resistance of four specimens representative of the abradable ZrO_2 surface layer and each of the three $\text{ZrO}_2/\text{CoCrAlY}$ intermediate layers of the sprayed $\text{ZrO}_2/\text{CoCrAlY}$ seal system were evaluated in isothermal furnace tests in air. Specimens, $0.254 \times 1.27 \times 3.81$ cm ($0.1 \times 0.5 \times 1.5$ in.), were prepared similarly to those used in the thermal expansion tests. Each specimen was measured, weighed and then exposed to estimated maximum operating temperatures for each respective layer, i.e. 1005K (1350F), 1061K (1450), 1144K (1600F) and 1589K (2400F) for the 40/60, 70/30, 85/15 $\text{ZrO}_2/\text{CoCrAlY}$ and the all ZrO_2 layers, respectively. Weight and dimensional changes were measured at 20 hour intervals and at the conclusion of the 100 hour test. Percent changes in specimen weight, volume and linear dimensions were calculated. Results are plotted in Figures 32 through 37.

The dimensional stability of each layer is anisotropic. The greatest change occurs in the direction normal to the substrate plane (through the coating thickness). Dimensional changes parallel to the substrate plane were approximately isotropic. The anisotropic behavior of the $\text{ZrO}_2/\text{CoCrAlY}$ composite layers is attributed to oxidation of the metal constituent which has greater surface area parallel to the substrate plane. Shrinkage of the ZrO_2 layer is attributed to sintering.

Initial weight loss experienced by the ZrO_2 layer is attributed to loss of residual moisture in the test specimen despite normal drying procedures.

4.3.3 Residual Stresses

Residual stress distribution in an erosion specimen was calculated from strain data measured on the back surface of the metal substrate. The specimen backing was strain gaged and, following zero adjustments of the gage instrumentation, the specimen was placed in the

fixture shown in Figure 38 which allowed the specimen to be held without application of force during grinding operations. The sprayed coating was incrementally machined away using a 100 grit diamond wheel and material removal rates no greater than 0.0508 mm (0.002 in.) per pass. After removal of each increment, the specimen was removed from the fixture and strain readings were recorded. This procedure was repeated until the sprayed structure was removed completely.

Residual stress distribution through the as-sprayed specimen was calculated by iteratively computing the stress necessary to cause the measured strain at the substrate surface contributed by each increment as it was added to the substrate and previously added increments. The stress in previously added increments was corrected for the added deflection.

Calculated residual stress distribution is shown in Figure 39. Compressive prestress is shown in two of the intermediate layers. It should be noted that the deflections measurements from which the stresses were calculated were less than the nominal measuring accuracy of the equipment used and, therefore, the noted stresses shown may be of marginal accuracy. Room temperature stresses in the ZrO_2 layer up to 73% of the average strength of this layer is indicated. No single stress free temperature exists for the calculated distribution.

4.4 ANALYSIS

As previously discussed, the most cost effective approach to seal design and development is to establish system capability analytically and conduct selected tests to substantiate the analytically predicted capability. Since material properties were not available at the initiation of this program, this approach was not possible within the time constraints of this program. However, thermal stress analyses were performed on the abrasability specimen configuration for the thermal cycle used in the thermal fatigue tests after material properties were determined. The analytical results were correlated with experimental results to substantiate the validity of the analysis. A typical gas turbine engine application of the layered system was also analytically evaluated.

4.4.1 General Approach

Existing two-dimensional finite element thermal and elastic stress computer programs were used to calculate steady state and transient temperature and stress distributions through the seal. Bread slice sections through the center of the seal as illustrated in Figure 40 were modeled to describe the specific seal system geometry, elemental breakup, material properties and boundary conditions. Two-dimensional steady state and transient temperature distributions through the seal in the axial and circumferential sections were calculated. Then two-dimensional stress distributions for thermal distributions at selected time points were computed by the stress program. Three-dimensional stresses were estimated by extrapolation of this two-dimensional information.

Two stress programs were used, a plane stress finite element elastic analysis program which assumes zero stress in the out of plane direction and a generalized plane strain finite element elastic analysis program which assumes plane sections remain plane. The plane stress program was used to analyze stresses in the circumferential section of the thermal fatigue test

specimen and both the circumferential and the axial sections of the engine specimen. The generalized plane strain program was used to analyze the axial section stresses in the thermal fatigue test specimen since it computes stresses which correlate very closely with three-dimensional stresses in all three planes. Experience has shown that applicability of the generalized plane strain program is restricted to configurations with aspect ratios greater than two. It, therefore, was not considered applicable for the engine seal which had an aspect ratio approaching unity.

Three-dimensional stresses were estimated in the thermal fatigue test specimen by assuming the axial stresses computed by the generalized plane strain program equal to three-dimensional values. The stresses at the intersection of the axial and circumferential sections analyzed were assumed identical. The generalized plane strain program values were compared with the appropriate plane stress program values at this intersection and used to establish a correction factor for the plane stress program output. This factor was then applied to the circumferential section stresses to estimate three-dimensional stress values. Since a one-dimensional temperature distribution was assumed (discussed later), stresses in circumferential planes parallel to the plane analyzed were estimated by ratioing the calculated stresses by the value of the axial section stresses at the center (initial intersection) with the axial section stresses at the intersection with the new plane.

Three-dimensional stresses were estimated in the engine seal by applying the following formulas at the intersection of the axial and circumferential sections:

$$\sigma_{3DA} = \sigma_A + \left(\frac{\nu}{1-\nu} \right) \sigma_C$$

and:

$$\sigma_{3DC} = \sigma_C + \left(\frac{\nu}{1-\nu} \right) \sigma_A$$

where: σ_{3DA} = three-dimensional stress in axial direction
 σ_{3DC} = three-dimensional stress in circumferential direction
 σ_A = two-dimensional stress in axial direction
 σ_C = two-dimensional stress in circumferential direction
 ν = Poisson's ratio

The ratio of two-dimensional to three-dimensional stress in the circumferential and axial directions was applied to the computed two-dimensional stresses in their respective sections to obtain estimated three-dimensional stress distributions. Stress distributions in other planes were then estimated in the same manner as used for the thermal fatigue test specimen since a one-dimensional circumferential temperature profile was assumed as discussed later.

4.4.2 Thermal Fatigue Test Specimen Analysis

The abrasability configuration test specimen was modeled and analyzed using the actual thermal cycle measured on the ZrO_2 and substrate surfaces shown in Figure 15. A one-dimensional radial temperature distribution through the specimen was assumed. An optical

pyrometer scan of the surface indicated that the surface temperature distribution was uniform within 111K (200F). Temperatures at the three substrate surface points were nearly the same.

Stresses were calculated for thermal distributions at idle and SLTO steady state conditions and at 20.5 seconds into the accel (heatup) and 17.5 seconds into the decel (cool down) portions of the thermal cycle, the points of maximum and minimum total thermal gradients through the specimen, respectively. Measured average seal layer thicknesses and material properties discussed earlier were used. Linear interpolation with respect to temperature was assumed through average measured values for elastic modulus, rupture strength and strain-to-failure data. Stresses were assumed symmetric about the center of the specimen in the circumferential and axial directions.

Results of these analyses are summarized in Figures 41 through 48. Maximum principal stresses in the planes of the sections were used as the basis for evaluating critical stress locations since it was assumed that the sprayed materials would behave in a brittle manner and fail due to exceeding the tensile strength.

Maximum principal stresses were found to generally be parallel to the substrate except near the edges where the radial stress component became significant at some cycle points. Generally radial stresses were very low.

Analytical results indicate that the stresses in the ZrO_2 layer exceed the strength of the material in the central portion of the seal at the surface at the 17.5 sec. decel point (Figure 47) and at the edge of the specimen at the ZrO_2 layer interface with the 85/15 ZrO_2 /CoCrAlY layer at SLTO (Figure 46). However, because of the non-linearity of the stress-strain relationship, the strain-to-failure was exceeded only at the 17.5 sec. decel point. Stresses in the 40/60 ZrO_2 /CoCrAlY layer also exceed the rupture strength of the material at the interface with the substrate at SLTO, but the strain associated with the stress was within the strain-to-failure.

Since calculated stresses were induced by thermal strains, rupture would not be predicted until the strain-to-failure was exceeded. On this basis, radial cracks in the central portion of the ZrO_2 layer was predicted to initiate at the seal surface during decel. Laminar cracks were not predicted on the basis of these analyses.

Residual stresses were not incorporated in these analyses because they were small in comparison to the estimated thermal stresses. In addition, since one stress free temperature does not exist for this system, incorporation of residual stresses would require modification to the current analytical program. Such effort was beyond the scope of this program.

In summary, thermal stress analysis results would have predicted the radial cracking observed in thermal fatigue tested specimens due to stress rupture during the first cool down. Laminar cracking due to thermal stresses alone would not have been predicted, but might have been caused by stress redistribution due to radial cracking and/or combined residual and thermal

stress effects. Other possible contributors to the laminar fracture mechanism are dimensional instability effects in the sprayed material and non-uniform temperature profiles over the seal specimen surfaces. Some non-uniformity of the circumferential temperature profile on the ZrO_2 surface was observed during testing. Whether this non-uniformity, which was approximately 111K (200F) between the center and the ends, with the center being hotter, was the cause or the result of the laminar cracking is unknown.

Both analytical and experimental results indicate the presence of excessive tensile stresses in the ZrO_2 layer. Modifications to the seal system geometry and/or processing to reduce or preferably eliminate the tensile stresses in the ZrO_2 layer without jeopardizing the satisfactory performance of the intermediate layers is considered necessary to achieve acceptable thermal fatigue performance.

4.4.3 Engine Application Analysis

The performance of the sprayed $\text{ZrO}_2/\text{CoCrAlY}$ seal system evaluated experimentally in this program was evaluated analytically in a gas turbine application on the basis of thermal stresses. A typical first stage high pressure turbine blade tip seal was selected jointly with the NASA Project Manager for this program. Necessary modifications were made to the bill-of-material seal segment design to permit application of the sprayed coating system within current engine clearance specifications. The seal segment configuration analyzed is shown in Figure 49.

A typical idle to SLTO and return to idle gas path and cooling air thermal and flow cycle was assumed. Temperature distributions through the seal were calculated using the two-dimensional finite element thermal analysis program with typical engine film heat transfer coefficients at steady state and selected times during the transient portions of the cycle. A two-dimensional temperature distribution was calculated in the axial plane. This distribution was assumed to be identical at all axial sections through the seal segment. Figure 50 shows the temperature profile on the ZrO_2 and substrate surfaces of the seal segment at the hottest spot.

Thermal stresses were calculated in the axial and circumferential directions using the plane stress finite element elastic analysis program. The circumferential section through the hot spot was selected for analysis since maximum thermal gradients are experienced through this plane and, therefore, maximum thermal stresses would be expected. Stresses were calculated at steady state idle and SLTO conditions and at 6 second accel and 12 second decel transient points where the maximum and minimum total thermal gradients occurred, respectively.

Results were similar to the results obtained for the thermal fatigue test specimen except that the ZrO_2 layer stresses were higher and the difference between axial and circumferential stresses were not as pronounced. The critical stress conditions occurred at the 12 second decel point. Figures 51 through 53 show calculated temperature and maximum principal stress distributions in the engine seal segment at the 12 second decel point.

Thermal fatigue cracking similar to that experienced by the thermal fatigue test specimens would be predicted for this sprayed $\text{ZrO}_2/\text{CoCrAlY}$ seal system in a typical gas turbine engine application based on the results of these analyses.

4.5 CYCLIC CRACK PROPAGATION STUDY

Experience under this program and other related programs indicates that improved thermal fatigue resistance is required for high temperature ceramic blade tip seal systems to perform satisfactorily in gas turbine engine applications. Two possible approaches toward improving the thermal fatigue resistance of the sprayed graded layered Y_2O_3 stabilized $\text{ZrO}_2/\text{CoCrAlY}$ seal system are modification of the seal materials to inhibit crack initiation and growth and/or geometric optimization of the seal configuration to minimize thermal stresses.

The current thermal/structural analyses techniques used by P&WA have demonstrated the capability of predicting the possibility of failure in graded ceramic seals systems during the first few thermal cycles of their life until cracking initiates. However, no reliable method of projecting long-term life exists. A study to evaluate the application of cyclic crack propagation theory in flawed structures to the sprayed $\text{ZrO}_2/\text{CoCrAlY}$ seal system and to identify structural improvements to the seal system to provide increased thermal cracking resistance was performed.

4.5.1 Literature Survey

An extensive literature search and review of past investigators' work to assess the state-of-the-art of crack initiation and propagation in brittle materials and possible application of current theory to the sprayed $\text{ZrO}_2/\text{CoCrAlY}$ seal system was performed. Twenty-eight articles, References 6 to 33, were reviewed.

Fracture in ceramics does not involve a simple extrapolation of the techniques found useful in determining the lives of most metals. Ceramics are brittle, which means they do not exhibit plastic behavior; in particular they do not exhibit strain hardening. In both ductile and brittle materials, failure initiates from the largest flaw since stress concentration increases with flaw size. In ductile materials a large number of flaws participate in the failure due to strain hardening occurring at the crack tips, forcing further loading to be taken up by the next largest flaw, therefore, it is the average of these flaws rather than the size of the largest flaw which controls failure. In ceramic materials, the largest initial flaw propagates unstably and, in theory, secondary flaws have no effect. This has the unfortunate consequence that strength becomes a function of size as well as material properties since the probability of encountering a flaw of critical length increases with specimen size. Conversely, the statistical variance of strength in a ceramic specimen of a given size is extremely high.

The lack of strain hardening also complicates fatigue analysis. No one has postulated a mechanism such as the theory upon which the Goodman/Soderberg S-N curves are based (which depend only on mean stress, stress range, and material strength) for brittle materials.

Strong arguments have been made that, in the absence of plastic flow, such a mechanism is improbable. Thus, the only avenue apparently open for fatigue investigations in brittle materials is the most basic — the determination of the growth characteristics of individual cracks.

Stable crack propagation mechanisms that depend on static, rather than cyclic, stress fields have been proposed by several investigators (References 6, 7, 8, 16 and 17). These depend on thermally induced processes such as grain boundary sliding, diffusion, and grain boundary dissolution. Although the latter can be significant even at room temperature in materials with large amounts of silica at the grain boundaries (which is not the case with the sprayed ZrO_2 materials), as a rule none of these processes is active at temperatures where the ceramic still retains a sizeable portion of its room temperature strength. Therefore, none of these mechanisms is expected to apply to the materials in the sprayed $\text{ZrO}_2/\text{CoCrAlY}$ seal system in the temperature range of interest to this program.

Nevertheless, mechanically induced crack propagation is still believed to be a controlling factor in sprayed ceramic seal cyclic failure. Three plausible mechanisms were identified:

1. Static fracture during the first cycle due to local stresses exceeding the strength of the seal material at that point,
2. A quasistatic fracture which occurs in the same manner as the first mechanism, but has the additional driving force of material shrinkage or growth with time, and
3. Progressive crack interaction, which is considered the most likely, in which cracks that form and stabilize in one part of the thermal cycle act during later portions of the cycle to redistribute stresses around other cracks which would have been otherwise stable. These latter cracks can then act in a reciprocal manner to encourage further growth of the first cracks or to precipitate additional cracks during the next thermal cycle. This process would continue in a stepwise manner until enough cracks join together to cause material spallation. An interesting aspect of this mechanism is that it requires a stress field which varies in a complex manner with time so that cracks in various directions and locations are encouraged to propagate at different parts of the cycle. A four-point bend specimen would never exhibit such a mechanism, but a thermally cycled seal certainly could.

4.5.2 Analytical Application of Theory

Cyclic temperature and thermal stress fields in an uncracked sprayed $\text{ZrO}_2/\text{CoCrAlY}$ engine seal were defined through the use of the two-dimensional finite element analyses described earlier. Areas of stress approaching or exceeding the material strength at one or more thermal cycle points were singled out and broken up more finely. Cracks were then introduced in these areas approximately perpendicular to the direction of the maximum principal stress. The plane stress program was then rerun to evaluate the effect of the cracks on stress

distribution. It should be noted that in this analysis the introduction of cracks did not significantly affect the temperature distribution until the advanced stages of crack growth, at which time crack tip temperatures will decrease somewhat.

Because of restraints in the computer program, the crack tip area could not be simulated in fine enough detail to obtain the absolute value of crack tip stresses. Therefore, a simple block geometry with an elemental breakup identical to the seal model in the vicinity of the crack was modeled and run for several different crack lengths with a uniform applied stress. Both stiff and flexible edge constraints, simulating internal and edge locations respectively, were evaluated. Crack tip stress to applied stress ratio ($\sigma_{\text{tip}}/\sigma_{\text{applied}}$) versus crack length (a) was plotted and compared to theoretical results as shown in Figure 55.

$$\frac{\sigma_{\text{theoretical}}}{\sigma_{\text{applied}}} = \frac{K_{\text{IT}}}{K_{\text{IC}}} = \left(\frac{a}{a_0} \right)^{1/2}$$

where:

$$\begin{aligned} K_{\text{IT}} &= \sigma_{\text{applied}} \sqrt{\pi a} \\ K_{\text{IC}} &= \sigma_{\text{applied}} \sqrt{\pi a_0} \\ a_0 &= \text{initial flaw length} \end{aligned}$$

As shown in Appendix A, $\sigma \propto K_I$. Comparison of the computed crack tip stress to the theoretical stress showed the finite element analysis to be of the right order of magnitude. Hence, a correction factor could be applied to the more complicated seal system program results under the assumption that the ratio of the finite element crack tip stress to the stress intensity factor ($K_I = \sigma_{\text{applied}} \sqrt{\pi a}$), for a given crack length and element breakup in the vicinity of the crack, is relatively independent of geometry and stress distribution. Favorable comparison of the corrected crack tip stress at the interface with the theory of Strangman¹⁴ gave encouragement that the assumption was correct.

The simple direct criterion of crack extension with $K_I \geq K_{\text{IC}}$, originally proposed by Griffith, as applied by Irwin was used as the criterion for crack extension. The biaxial and triaxial criteria of Sih⁹ and Drucker and Rice¹⁰ were rejected due to questions raised in the literature concerning the general applicability of such criteria (References 11 and 12) and the apparent lack of a mechanism for Mode II, shear stress in the direction of the crack opening (edge sliding) and Mode III, shear stress perpendicular to the direction of the crack opening (tearing), crack extension in brittle materials. It was postulated that since brittle material failure depends primarily on maximum principal stress, and since shear stresses can be resolved into principal stress components, crack propagation in ceramics can be dealt with using Mode I (membrane stress propendicular to the direction of the crack opening) data. However, a note of caution is issued here, that in spite of the theoretical justification for neglecting K_{II} and K_{III} , the Griffith-Irwin criterion does not automatically control fracture and requires experimental verification for this application.

The selected crack extension criterion was applied to the cracks in an iterative manner, breaking elements ahead of the crack in a direction approximately perpendicular to the maximum principal stress until the crack tip stress intensity factor (K_I) dropped below the critical stress intensity factor (K_{IC}). The iterative distribution of cyclic stress is shown in Figures 55 through 57. For simplicity the values are left in terms of maximum principal two-dimensional stress rather than stress intensity factor. No loss of information results since $K_I \propto \sigma_{tip}$ and $K_{IC} \propto \sigma_u$ and, hence, the criterion $K_I \geq K_{IC}$ can be replaced by $\sigma_{tip} \geq \sigma_u$, as shown in Appendix A. Stresses at the crack tip have been corrected per Figure 54. It was assumed that the strain must exceed the strain to failure to initiate cracking but that the corrected stress at the crack tip need only exceed the strength of the material to propagate the crack. The center-to-center crack distribution was estimated to be 2.54 mm (0.1 in.) using the mud-flat theory developed by P&WA which provides a statistically consistent redistribution of stresses as cracking proceeds.

Although it is projected that these center cracks will stabilize after the first thermal cycle rather than lead to immediate material spallation, it is believed that they will propagate by the progressive crack interaction mechanism introduced earlier. Although no data is available to allow quantitative predictions, the propensity for crack propagation by the mechanism depends on the probability of nucleating cracks other than those tracked by the finite element analysis in areas where the stress is fairly high, but below the mean strength of the material. The probability of nucleating cracks in most ceramics fits the empirical relation proposed by Weibull and modified by McClintock¹³:

$$p = 1 - e^{-X}$$

Where: $X = \frac{(S_1 - S_L)^m}{(S_0 - S_L)}$

- p = probability of nucleating a crack at a given grain boundary or within a given grain.
- S_1 = stress level imposed on the crack tip
- m = a positive empirical constant, normally between 3 and 10
- S_L = an empirical constant similar to S_e (endurance limit) in S-N theory
- S_0 = an empirical constant, approximately equal to the material's mean strength

For $m = 3$ and $S_L \approx 0$ (common values for ceramics), this means there is still a 35% probability of nucleating cracks at a grain boundary even if the stress is only 75% of the mean strength. Therefore, since several grain boundaries are within the sphere of influence of a propagating crack at any given time, the probability of cracks cyclically propagating by progressive crack interaction for $\sigma \approx 0.75 \sigma_u$ is high. The stresses shown in Figure 51 are of roughly this magnitude, and crack propagation can be expected to occur rather quickly.

Experimental evidence as shown in the picture of the thermal shock specimen in Figures 18 through 20 qualitatively verifies the results of the analysis. One or several cracks form in the central portion of the seal, extend to the interface, and are then forced to turn, branch, or

stop by the higher strength of the intermediate layer and the changing direction of the principal stresses. Once the cracks are turned so they run parallel to the interface, the direction of the maximum principal stress and the high strength of the intermediate layer work together to keep them parallel. Some of these cracks propagate rapidly and some don't depending on the flaw density in their vicinity, which will influence the probability of secondary crack nucleation as discussed earlier.

Edge crack stresses are seen to be lower than center crack stresses, and the probability of crack initiation and propagation is therefore less. Edge stresses can be effectively increased by as much as a factor of four by edge discontinuities as shown in Figure 58, but even this would not be expected to cause edge failure in the average seal with this configuration. If edge cracks do occur, analysis shows them to be stable, i.e., the tips propagate to regions of low stress and then stop.

4.5.3 Methods of Increasing Cyclic Life

The benefits of strain hardening — less statistical variation of strength, high strain-to-failure, and stable crack propagation — can be artificially introduced into ceramics by a dispersion of non-homogeneities such as second phase particles, pores, and microcracks. These interruptions in the continuity of the matrix act to lower the stress concentration at the tip of a crack by blunting it or by absorbing crack strain energy through elastic deformation of the material ahead of the tip. On the negative side, non-homogeneities also provide new crack initiation sites and generally lower K_{IC} and σ_u . However, for constant deformation problems such as occur in thermal stress, this is not a serious liability since the increased strain-to-failure (ϵ_f) means a lower effective modulus and hence lower K_I for a given thermal field. Proper choice of the size, shape, and distribution of the nonhomogeneities can be expected to significantly decrease K_I/K_{IC} in spite of a lower K_{IC} value.

Lange¹⁵ proposed a widely accepted criteria for cracks forming around and tangent to the surface of second phase particles. The particles separate from the matrix and/or form microcracks in their vicinity when

$$(\sigma + \sigma_\alpha)^2 R > C$$

Where: σ = applied stress
 σ_α = particle/matrix mismatch thermal stress created during cooldown from fabrication
 R = particle radius
 C = unknown constant function of the particle shape and particle/matrix physical properties

Once matrix separation occurs, the hole encompassing the particle can be expected to behave much like a pore. This is generally good if a crack was already present, since the stress concentration function $g(a)$ in the equation $K_I = \sigma \times g(a)$ is approximately equal to $\sqrt{\pi} a$ for a through-crack in an infinite plate, while it is significantly lower than this for a pore. However, if a crack was not already present, then creating a pore is harmful since a stress concentration site now exists where there was none before. A similar competition between phenomena must

be considered when establishing particle shape. Spherical particles produce pores with the lowest stress concentration and, for most applications, would absorb incoming cracks the best and lower K_{IC} the least. However, in more punishing applications, the stress concentration may still not be low enough to prevent crack propagation, and the mechanism of preventing failure must shift from halting cracks to mechanically holding together the cracked sections of the part. This may be accomplished by incorporating long fibers, hollow semi-spheres, or thistle-shaped particles.

Quantitative analysis to determine optimum particle parameters is prevented by our lack of knowledge concerning the factor C in Lange's equation. We can, however, set forth an efficient analytical/experimental procedure to optimize the incorporation of particles to inhibit crack propagation.

1. Initially use spherical particles since they are the most easily understood.
2. To prevent a decrease in K_{IC} , choose particle radius R such that $g(R) = \sqrt{\pi a_0}$.
3. Choose particle α such that $\sigma_\alpha^2 R > C$ so that beneficial microcracks are formed which make the matrix more compliant. This will require trial and error.
4. Choose particle $E > E_{\text{matrix}}$ and $\sigma_\mu > \sigma_\mu \text{ matrix}$ so that cracks will tend to stop at a particle or form a pore around it rather than go through it.
5. Initially space particle centers two diameters apart, at which distance their crack stress fields will not interact extensively (St. Venant's principle), slowing progressive crack interaction, and yet the particles are close enough to work together to stop wide crack fronts.
6. Test the resulting microstructure under the thermal stress field expected in service. If microcracks initiate at the particles, make them smaller. If wide crack fronts propagate easily past the particles, make them closer together. If cracks appear to propagate rapidly by progressive crack interaction due to cracks initiated by the particles, make them further apart. If insufficient microcracks form during fabrication, make α and E_{part} larger. If cracks propagate through particles rather than around them, make σ_μ particle higher.
7. If design iterations based on step 6 fail to sufficiently slow crack propagation, try the odd-shaped particles mentioned earlier, using the same criteria for particle size, distribution, and properties given for spherical particles, except choosing $\alpha_{\text{part}} \approx \alpha_{\text{matrix}}$ and $E_{\text{part}} \approx E_{\text{matrix}}$ to maintain as much matrix/particle continuity as possible.

Pores¹⁹ may be used in the same manner as second phase particles to impede crack growth, and the same tradeoffs apply. Pores have an advantage over second phase particles in that they lower effective modulus to a larger extent and hence the matrix is more compliant

at the crack tip and less likely to propagate cracks. However, pores do not provide a mechanism for the formation of beneficial microcracks. More importantly, the shape of a pore is much more difficult to control than that of a second phase particle, and hence they are not as effective in lowering stress intensity at a crack tip, which prefers a crack inhibitor to be perfectly spherical. Odd-shaped pores cannot act, as odd-shaped particles do, to mechanically hold the matrix together, and in fact may actually aid crack propagation by providing an automatic extension for cracks that reach them while maintaining or even increasing the stress concentration function of the crack, $g(a)$. In short, pores are better than no nonhomogeneities at all, but are a poor choice compared to second phase particles unless they are desired for other characteristics such as increased seal abrasability.

Microcracks have been mentioned as beneficial because they substantially increase the matrix compliance ahead of a propagating crack (References 20 through 24.) By increasing the surface energy associated with crack extension, they allow the strain energy at the tip of the crack to be dissipated at such a high rate that crack extension becomes energetically unsupported. However, microcracks can act as macrocrack nucleation sites if they are too large or too close together. Hasselman also points out that they may be initially unstable under thermal stress unless their lengths at the end of fabrication satisfy the criterion (for plane stress):

$$l_m \geq (6 \pi N)^{-1/2}$$

Where: l_m = the crack length at the end of fabrication

N = the number of cracks per unit area in the plane of non-zero stress

To maintain as high a value of K_I as possible, such instability should be avoided if possible by making microcracks just large enough to satisfy the criterion. Thermal shock, ultrasonics, and second phase particles are some of the mechanisms used to create or extend microcracks. N is not generally a parameter available for optimization, but, according to Reference 21, is a function of material properties only and hence something that must be accepted and worked around.

Claussen (Reference 25) suggested using dispersed monoclinic ZrO_2 as a microcrack generator, and reported significant success. The monoclinic ZrO_2 undergoes a phase transformation and accompanying shrinkage upon cooldown from fabrication and creates finely dispersed microcracks within the ZrO_2 second phase particles. However, it is questionable whether this is an ideal method of generating microcracks since it is desirable to nucleate such cracks within the matrix as well as within the second phase ZrO_2 particles. A fine enough dispersion of the particles may minimize this negative aspect of the technique.

Development of the plasma spray application techniques to fabricate the structural improvements discussed would require an iterative approach and would be costly. Achieving controlled nonhomogeneities (i.e., controlled size, shape and distribution) in a plasma sprayed structure would be very difficult. Addition of second phase particles to the matrix material powders is feasible, but as-deposited shape and distribution may prove to be highly variable, especially if the size and/or density of the second phase particles are significantly different from the matrix material.

It should be noted that the model which was used to establish structural characteristics to inhibit crack initiation and propagation has been proposed but is not yet substantiated. The model should be substantiated before proceeding with the relatively costly effort to produce the configuration defined to improve the crack inhibiting capability.

An approach combining experimental and analytical methods is required to substantiate the model. A number of sub-scale seal specimens would be subjected to closely controlled, repeatable simulated engine thermal cycles. At predetermined intervals, selected specimens would be withdrawn from the test for sectioning and analysis to determine the extent of any damage. Accompanying structural analysis would be used to determine the changes in the stress field due to the frequency of both major and minor cracks and any possible plasticity. Results would be correlated with the model and appropriate modifications and/or new theories of damage mechanisms would be postulated.

To support the analysis, measurement of the room temperature stress state of the seal system, both as fabricated and after the first thermal cycle, would be necessary. In addition more complete thermal/mechanical properties would be required to permit more accurate modeling. These would include thermal expansion coefficients to higher temperatures, modulus of elasticity and ultimate strength at intermediate as well as end points, Poisson's ratio, and creep properties at operating temperatures.

As a final note on the enhancement of cyclic life, it should be pointed out that, although nonhomogeneities when properly used can be very effective crack inhibitors, the straight-forward concept of making the stress field at the crack tip compressive through in-process prestressing is believed to be the most powerful method of decreasing the sensitivity of a component to fatigue. This technique has been used with success for years by the pressure vessel industry, among others, and provides the extra bonus in dealing with ceramics of taking advantage of their high compressive/tensile strength ratio (~ 8). This should be utilized to the fullest possible extent before experimentation with microstructural optimization begins.

Since process modifications, such as preheating or prestressing the metal substrate or post fabrication heat treatment, to generate compressive residual stresses in the as-fabricated system are fairly straight forward and relatively low risk, this approach should be given priority over the higher risk approaches of microstructural modifications.

4.6 GEOMETRIC OPTIMIZATION OF THE LAYER STRUCTURE

Optimization of the seal system geometry is one method of improving the thermal fatigue resistance of the sprayed $\text{ZrO}_2/\text{CoCrAlY}$ seal system. Since geometric optimization will not affect the properties of the ceramic it can be accomplished without affecting abrasability or erosion characteristics. Many factors, including seal size and shape, sprayed material layer thicknesses and properties, externally applied loads, and method of supporting the seal, will dictate the optimum configuration for a particular application. Obviously, the iterative experimental approach to arrive at an optimum seal configuration would be both time consuming and expensive due to the large number of variables involved. Therefore, once

again, the most cost and time effective approach is to optimize the seal configuration analytically and verify the analytical results by selected experimental testing.

The optimization study conducted under this program determined a configuration which would minimize thermal stresses in the thermal fatigue test specimen by using materials of the baseline sprayed $\text{ZrO}_2/\text{CoCrAlY}$ seal system but varying thicknesses of the sprayed material layers and the metal substrate. The optimized configuration defined was then fabricated and rig tested to evaluate abrasability, erosion and thermal fatigue characteristics. Abrasability and erosion tests were conducted primarily to obtain data with regard to performance repeatability. Selected specimens were sectioned and metallographically analyzed to verify the configuration and microstructure of the seal system and identify initiation sites and evaluate the extent of thermal fatigue cracking.

4.6.1 Analysis

The thermal cycle and "hot spot" film heat transfer coefficients used for the engine seal segment analysis discussed earlier was used to compute the temperature distribution in the seal specimen for each of the configurations evaluated. A one-dimensional temperature distribution through the specimen was assumed as done for the analysis of the thermal fatigue test specimen.

Thermal stresses for twelve different seal configurations shown in Table X were evaluated. Prior analyses of the baseline (thermal fatigue test specimen) configuration and engine seal configuration had indicated that maximum stresses in the ZrO_2 layer occur at the center of the specimen in the circumferential direction during the point in the decel portion of the thermal cycle when the thermal gradient was minimum. For this reason it was assumed that an analysis of the 12 second decel point in the circumferential plane only would be sufficient for the optimization study.

The results of these analyses are summarized in Table XI. Figure 59 identifies the location of the temperatures and stresses shown in Table XI. Each individual sprayed material layer and substrate thickness was arbitrarily varied independently in configurations 1 through 5 while the remaining layers were maintained identical to the baseline configuration. Combining these results with the baseline configuration results permitted evaluating the effect of thickness changes to each individual layer on stress distribution in the circumferential plane through the seal system.

Configuration 6 was selected on the basis of preliminary calculations which indicated approximately equal average thermal growths of each layer and the substrate at SLTO.

Analysis of the results from configurations 1 through 6 indicated stresses would be minimized by increasing the ZrO_2 layer thickness and reducing the 70/30 and 40/60 $\text{ZrO}_2/\text{CoCrAlY}$ layers and the substrate. The results of the analyses are not necessarily contrary to results of metallography described in Section 4.2.3 which showed that the specimen with the thinner ceramic layer performed better in thermal fatigue testing. The difference in thermal fatigue test results could have been attributable to the described microstructural differences rather than the ceramic layer thickness variation.

The thickness shown in configuration 8 were selected for evaluation. However, concern over the effect of reduced substrate thickness on thermal deflection also led to the analysis of configuration 7 with the baseline substrate thicknesses.

As predicted, the 12 second decel stresses in configuration 8 were significantly lower than any of the previously analyzed configurations. The thermal deflection of configuration 8 was slightly greater than configuration 7, but, surprisingly, both configurations 7 and 8 had significantly less thermal deflection than the baseline configuration. Therefore, configuration 8 was initially selected as the optimized configuration and thermal stresses at the other thermal cycle points were computed. As shown in Table XI, this revealed that the maximum ZrO_2 layer stress for this configuration would occur at the ZrO_2 layer interface with the intermediate layer at SLTO.

Configurations 9 and 10 were then analyzed at both 12 second decel and SLTO to further evaluate the effects of coating layer and substrate thickness variations on stress distributions at both cycle points. Analysis of these results indicated configuration 12 should result in approximately equal maximum thermal stresses at the surface and interface of the ZrO_2 layer during the thermal cycle. However, the effect of substituting additional 40/60 ZrO_2 /CoCrAlY layer thickness for the 70/30 ZrO_2 /CoCrAlY layer was not clear and there was a fabrication processing and reduced cost advantage to reducing the number of layers in the sprayed coating. Therefore, configuration 11 was also analyzed.

Review of the data indicated the expected results for configuration 12. Configuration 11 surface stresses were slightly lower than configuration 12 while the interface stresses were slightly higher. After consideration of the processing and cost advantages, configuration 11 was selected with the approval of the NASA Project Manager for fabrication for verification testing. The analysis demonstrated that the ZrO_2 layer and metal substrate thicknesses were geometry parameters which effected the ZrO_2 layer stresses the most.

4.6.2 Verification Tests

Abradability and erosion specimens were fabricated to configuration 11 specifications using the same plasma spray parameters, techniques and equipment employed for fabrication of the baseline ZrO_2 /CoCrAlY seal system. (Because of manufacturing process control variations in the ZrO_2 layer thickness actually obtained was greater than targeted).

Abradability and erosion rig tests were run using the same rigs and test procedures employed for earlier testing of the baseline system. Test conditions and results are listed in Tables XII and XIII. The volume wear ratio was slightly lower and erosion rate slightly higher than exhibited by the baseline system tested at the same conditions, indicating slightly better abrasability and slightly poorer erosion resistance. It is interesting to note that these results correlate with the hardness measurements. The specimens of the optimized configuration were softer on the R_{545Y} scale than the baseline specimens.

There was a large difference in hardness between the abrasability (70.3) and the erosion (45.6) specimens. Both specimens were sprayed in the same ring at the same time and there was no visual evidence of defects such as laminar cracking that might account for this difference.

The erosion specimen delaminated at the ZrO_2 layer interface with the intermediate layer, Figure 60, after the second five minute exposure period. Inspection of the fracture surfaces raises questions regarding the soundness of the interlayer bond since the fracture occurred cleanly at the interface except for a few spots of pullout in the ZrO_2 layer. Further investigation of the interlayer bond strength should be pursued since the laminar cracking in this vicinity which also resulted from thermal fatigue testing could be attributable to a low bond strength.

Another condition of interest exhibited by the erosion specimen was the extent of thermal cracking. As shown in Figure 61, fairly extensive thermal cracking occurred on the specimen surface but only one crack propagated through the ZrO_2 layer.

Two abrasability specimens were thermal fatigue tested using the same thermal cycle used for baseline system tests. Test results are summarized in Table XIV. Both specimens survived 100 thermal cycles without failure but did develop radial and laminar cracks as shown in Figures 61 and 62. Radial cracks initiated in the first few cycles but did not appear to widen to the same extent as in the baseline system specimens. Laminar cracks could not be detected until removal of the specimen from the holding fixture at completion of the test, therefore, the time of initiation is unknown. The extent of laminar cracking on the second specimen tested was greater than on the first as may be seen by comparison of Figures 61 and 62.

One specimen, No. 6, was sectioned in the axial and circumferential directions and metallographically examined to determine the extent of thermal cracking and to identify crack initiation sites or conditions which may have contributed to thermal cracking. As shown in Figures 63 and 64, radial cracks initiated at the ZrO_2 surface in the central portion of the specimen and propagated only partially through the ZrO_2 layer. Laminar cracks initiated at the edge in the overspray or pyramid area of the ZrO_2 layer and propagated a short distance along the ZrO_2 layer interface. These results were very encouraging in that, for the first time, the evidence indicates that radial cracks can be arrested in the ZrO_2 layer by design of the seal system and that laminar cracks may not be extensions of the radial cracks. Analysis of pyramiding effects on thermal stress distributions in a related program using estimated material properties indicate that pyramiding of the spray material can increase radial stresses at the edges by an order of magnitude or more. This could be the cause of the laminar cracking.

In addition to the thermal fatigue specimens an as-sprayed erosion specimen was also metallographically evaluated, primarily to determine the actual sprayed thickness in comparison with the targeted configuration. Metallurgical evaluation of both specimens indicated average thicknesses of the 40/60 and 85/15 $\text{ZrO}_2/\text{CoCrAlY}$ layers were very close to the 0.762 mm (0.030 in.) target and that variation in the thickness in both the axial and circumferential directions was relatively small. However, average thickness of the ZrO_2 layer was greater than the 2.286 mm (0.090 in.) target. The minimum to maximum thickness in the axial direction was relatively large, 2.616 mm (0.103 in.) to 3.302 mm (0.130 in.). Thickness measurements for the erosion and thermal fatigue tested abrasability specimens are summarized in Tables XII and XIII, respectively.

Porosity and metal volume fractions of each layer were determined for the as-sprayed erosion specimen by the point count method. Results, summarized in Table XIV, are in good agreement with values obtained on the baseline configuration thermal fatigue tested specimens shown in Table VII except the metal volume of the 85/15 ZrO₂/CoCrAlY layer which is almost double earlier values.

Microstructural comparison of the optimized specimen with the earlier baseline specimens fabricated under this contract and NAS3-18565 indicated the ZrO₂ layer was similar to the NAS3-18565 specimen, i.e., large ZrO₂ agglomerate and pores. Other layers appeared similar to all previous specimens. Figure 65 shows typical microstructure of each layer for the thermal fatigue tested specimen. It is also typical for the erosion specimen.

4.6.3 Conclusions and Recommendations

Analytical results indicate that the maximum thermal stresses can be reduced by approximately 40% in the ZrO₂ layer by layer thickness optimization with the constraint of using the materials used in the baseline sprayed ZrO₂/CoCrAlY seal system. Further stress reduction may be possible through modification of the thermal/mechanical properties of the intermediate layers and/or substrate by changing ZrO₂ and CoCrAlY ratios and/or changing the metallic constituent in the ZrO₂/metal layers or the substrate. It is doubtful, however, that sufficient thermal stress reduction could be achieved through this optimization effort to eliminate the possibility of tensile stress cracking. But, any gain in this direction, especially if it significantly reduces the total cyclic stress range, should greatly enhance the probability of success when combined with other methods of inhibiting crack initiation and propagation such as manufacturing techniques discussed earlier.

The thermal stress analysis was compared with the results of thermal fatigue testing. The geometry of the fabricated specimen, because of the need for improved spray process control, compared more closely to configuration 8. For that reason, the stresses for configuration 8 were considered. As shown in Table XI the maximum stress, considering two dimensional stresses in the circumferential plane, occurred in the ZrO₂ at the intermediate layer interface. Test results showed radial cracks originated at the surface. The difference in location of cracking and the maximum stress could have resulted from the simplifying assumption used in the analysis. Interaction of residual stresses, the added effect of axial stresses, as well as circumferential and axial variations in thickness and surface temperature distribution could have contributed to a change in location of maximum stress.

Initiation of laminar cracking resulting from thermal fatigue testing was not predicted by the analysis performed. It is possible that modification of the configuration analyzed to include pyramiding at the edge would have predicted the laminar cracking. Elimination of the pyramiding by grinding back the specimen edges prior to testing is recommended for all future tests to eliminate the effects of spray material pyramiding.

Thickness variations had very little effect on the seal system surface temperatures for the same boundary conditions in the hot gas and cooling air. Internal temperatures, however, are significantly affected, especially by the ZrO₂ layer thickness. The plasma spray fabrication process requires further evaluation and refinement to define and control the causes of hardness and microstructural variations noted and to obtain better uniformity and control of layer thickness.

REFERENCES

1. "Continued Development of Abradable Gas Path Seals," Shiembob, L. T., NASA CR 134879 (1975).
2. "Development of Abradable Gas Path Seals," Shiembob, L. T., NASA CR 134689 (1974).
3. "A Study of Erosion Phenomena, Part I," Bitter, J.G.A., Wear, 6, (1963) 5-21.
4. "Erosion By a Stream of Solid Particles," Neilson, J. H. and Gilchrist, A., Wear, 11, (1968) 111-122.
5. "Internal Ruptures and Recombinations in Anisotropic Ceramic Materials," Buessern, W. R., Mechanical Properties of Engineering Ceramics, Interscience (1961).
6. "Crack Propagation and Fracture in Silicon Carbide," Evans and Lange, J. of Matl. Sci. (1975).
7. "Static Fatigue of Ceramic Materials," Gulden, NTIS AD-786-231.
8. "High Temperature Slow Crack Growth in Ceramic Materials," Evans, A.G., NTIS Com-74-10476.
9. "A Fracture Criterion for 3D Crack Problems," G. Sih, Engr. F.M. (1974).
10. "Plastic Deformation in Brittle and Ductile Fracture," Drucker and Rice, Engr. F.M. (1970).
11. "Exploratory Development of Fracture Mechanics of Composite Materials," Cruse, T., NTIS AD/A-001-609.
12. "A Unified Approach to Elastic/Plastic Fracture Mechanics," Neale and Townley, Berkeley Nuclear Labs (Britain) RD/B/N3358.
13. "Principal Stress Effects on Brittle Crack Statistics," McClintock and Mayson, ASME AMD V.16.
14. "Thermal Fatigue of Coated Super-Alloys," Strangman and Hopkins, Amer. Cer. Soc. Annual Meeting, May 1975.
15. "Criteria for Crack Extension and Arrest in Residual, Localized Stress Fields Associated with 2nd Phase Particles," Lange, NTIS AD-776190.
16. "Crack Propagation in Ceramic Materials Under Cyclic Loading Conditions," Evans and Fuller, Met. Trans., January 1974.

17. "A Model for Crack Propagation in Polycrystalline Ceramics," Evans and Graham, *Acta Met.*, November 1974.
18. "Application of Fracture Mechanics Theory to Thermal Shock Resistance of Brittle Materials," Hasselman, D., A.F. Rpt. #SAMSO-TR-72-64.
19. "Effect of Porosity on Thermal Stress Fracture," Coble and Kingery, *J. Am. Cer. Soc.*, January 1955.
20. "Fracture Toughness of Partially Stabilized ZrO_2 in the System $CaO-ZrO_2$," Green, Nicholson, Embury, *J. Am. Cer. Soc.*, V 56, #12.
21. "On the Density of Microcracks Formed During the Fracture of Ceramics," Hoagland, Embury, and Green, *Scripta Meta.* (1975).
22. "Resistance to Crack Propagation in Ceramics Subject to Thermal Shock," Gupta, *J. of Mat. Sci.* (1973).
23. "Experimental Evidence for Thermal Shock Damage Resistance," Nakayama and Ishizuka, *Cer. Bull.* (1966).
24. "Analysis of Strain in Fracture of Brittle Solids with High Densities of Microcracks," Hasselman, *J. Amer. Cer. Soc.*, August 1969.
25. "Fracture Toughness of Al_2O_3 with an Unstabilized ZrO_2 Dispersed Phase," Claussen, *J. Amer. Cer. Soc.*, February 1976.
26. "Proceedings of a Workshop on Non-Destructive Evaluation of Residual Stress," NTIAC-76-2.
27. "Dynamic Fracture of a Beam or Plate in Bending," ASME paper 76-APM-15.
28. "Strength-Size Relationships in Ceramic Materials," Bansal, NTIS AD-A016-835.
29. "Stresses in Bonded Materials with a Crack Perpendicular to the Interface," Cook and Erdogan, *Int. J. Engr. Sci.* (1972).
30. "Two Bonded Half Planes with a Crack Going Through the Interface," *Int. J. of Engr. Sci.* (1973).
31. "The Stress Intensity of a Crack at an Interface Between Two Materials," Lin, AFOSR TR 73-1917.
32. "Growth Characteristics of Two Interacting Cracks," Budaliance and Gupta, *Engr. F.M.* (1976).

33. "Fatigue Damage Analysis and Life Prediction of a Composite Laminate," Heller, Lin, and Swift, AIAA 75-768.
34. Griffith, A.A., Phil. Trans. Roy. Soc. (London), A221 (4), p.163-168 (1920).
35. "Analysis of Stresses and Strains Near the End of a Crack Traversing a Plate," Irwin, G.R., J. Appl. Mech., V24, p.361-364 (1957).

TABLE I
SINGLE BLADE/MULTI BLADE COMPARISON
RIG TEST CONFIGURATION

Modeling Considerations	Single Blade	12 Blade	Typical Commercial Engine (Est.)
Blade Tip Circumference (C)	65.5 cm (25.8 in.)	65.5 cm (25.8 in.)	304.8 cm (120 in.)
Number Blades (n)	1	12	80 active blades*
Blade Tip Spacing (C/n)	65.5 cm (25.8 in.)	5.6 cm (2.2 in.)	3.8 cm (1.5 in.)
Blade Tip Velocity (V)	304.8 m/s (1000 fps)	304.8 m/s (1000 fps)	365.8 m/s (1200 fps)
RPM (N)	26700	26700	7500
Blade Pass Frequency (bpf = 12nV C	467 cps	5600 cps	9600 cps
Mech. Feed Rate (v)	0.0025 mm/s (0.0001 in/sec)	0.152 mm/s (0.006 in/sec)	0.254 mm/s (0.010 in/sec)
Theoretical Chip Thickness (d = v/bpf)	5.463×10^{-8} m/s (2.14×10^{-6} in.)	2.718×10^{-8} m/s (1.07×10^{-6} in.)	2.642×10^{-8} m/s (1.04×10^{-6} in.)
Seal Rub Length (L)	2.54 cm (1 in.)	2.54 cm (1 in.)	50.8 cm (20 in.)
Blade Thickness (1)	0.3175 cm (0.125 in.)	0.3175 cm (0.125 in.)	0.508 cm (0.2 in.)
Total Blade Thickness (nl)	0.3175 cm (0.125 in.)	0.3175 cm (1.5 in.)	40.64 cm (16 in.)
L/nl	8	.67	1.25

*60% of total no blades.

TABLE II
ABRADABILITY TEST SCHEDULE

° K	Temp (° F)	Test Conditions				Baseline System	Modified System
		Tip Speed		Incursion Rate			
		m/s	(ft/sec)	mm/s	(in/sec)		
1366	(2000)	304.8	1000	0.0254	(0.001)	x	
1589	(2400)	304.8	1000	0.0254	(0.001)	x	x
1589	(2400	304.8	1000	0.254	(0.010)	x	
1589	(2400)	304.8	1000	0.00254	(0.0001)	x	x

TABLE III
ABRADABILITY TEST DATA SUMMARY
BLADE MATERIAL: B-1900

Test No.	Hardness, Avg. $R_{0.45Y}$	No. Blades	Test Conditions		Seal Surf. Temp. ($^{\circ}F$) $^{\circ}K$	Interaction Rate (in/sec) mm/s	Penetration Depth (inch) mm	Seal Wear, Max (inch) mm	Seal Specimen		Post Test Information			Blade Wear, Avg. (inch) mm	Heat Discoloration	Pickup (inch) mm	VWR	Remarks
			Blade Tip Dia. (inch) cm	Blade Tip Velocity (ft/sec) m/s					Transfer To Seal	Rub Pattern	Actual Surf. Temp. ($^{\circ}F$) $^{\circ}K$	Max. Surf. Temp. ($^{\circ}F$) $^{\circ}K$	Normal Load, Max. (lb) N					
Sprayed Graded Y_2O_3 Stabilized $ZrO_2/CoCrAlY$																		
1	73.8	12	(8.625) 21.91	(820) 249.9	(2000) 1366	(0.001) 0.0254	(0.030) 0.762	(0.0128) 0.3251	Light Transfer	Continuous	(1940) 1333	(3290) 2083	(6.2) 27.58	(0.0265) 0.6731	Negligible	(~0.381) ~0.015 metal on leading edge at tip	4.57	Deep groove approx. half blade width with little blade wear. slight groove and some spalling other half with heavy blade wear. Axial cracks in rub path, some propagated to edge. Some thermal cracks induced during setup. Lower quarter and top corner of ceramic layer fractured.
2	72.3	12	(8.5) 21.59	(1000) 304.8	(2400) 1589	(0.001) 0.0254	(0.030) 0.762	(0.0181) 0.4597	Light Transfer	Continuous	(2440) 1611	(3245) 2050	(10.1) 44.93	(0.0053) 0.1346	Negligible	(~0.178) ~0.007 metal on leading side at tip	0.318	Axial cracks in rub path, some propagated to edge. Laminar crack at ceramic layer interface on one side. Yellowish discoloration along cracks.
4	72.7	12	(8.5) 21.59	(1000) 304.8	(2400) 1589	(0.0001) 0.00254	(0.030) 0.762	(0.0065) 0.1651	Moderate Transfer ~0.010" buildup at exit end	Continuous	(2430) 1605	(3050) 1950	(7.4) 37.92	(0.0242) 0.6147	Negligible	(~0.330) ~0.013 metal on leading side at tip	16.9	Axial cracks in rub path. Short laminar crack at ceramic layer interface on one side. Small spall at groove exit end.
6	72.8	12	(8.5) 21.59	(1000) 304.8	(2400) 1589	(0.010) 0.254	(0.030) 0.762	None	Heavy transfer ~0.023" buildup at exit end	Continuous	(2455) 1619	(2685) 1747	(18.1) 80.5	(0.0419) 1.0643	Dark Straw at tip	(~0.584) ~0.023 metal on leading side at tip	Indeterminate	Axial crack and one spall in transfer. Short axial hairline cracks along one edge. Laminar crack at ceramic layer interface on same side. Top corner chipped pretest.
Sprayed Graded Y_2O_3 Stabilized $ZrO_2/CoCrAlY$ With Increased Porosity Surface Layer																		
3	68.8	12	(8.5) 21.59	(1000) 304.8	(2400) 1589	(0.001) 0.0254	(0.020) 0.508	(0.0096) 0.2438	Light Transfer	Continuous	(2440) 1611	(3260) 2066	(3.6) 16.01	(0.0023) 0.0584	Negligible	Slight metal on leading side at tip	0.354	Axial cracks in rub path, none propagated to edge. Short laminar crack at ceramic layer interface on one side.
5	74.5	12	(8.5) 21.59	(1000) 304.8	(2400) 1589	(0.0001) 0.00254	(0.020) 0.508	(0.0042) 0.1067	Moderate Transfer ~0.008" buildup at exit end	Continuous	(2435) 1608	(3105) 0.980	(5.5) 24.47	(0.0117) 0.2972	Negligible	(~0.356) ~0.314 metal on leading side at tip	18.4	Axial cracks in rub path, none propagated to edge. Laminar crack at ceramic layer interface on one side.
Sprayed Graded Y_2O_3 Stabilized $ZrO_2/CoCrAlY$ Optimized Configuration No. 11																		
7	70.3	12	(8.5) 21.59	(1000) 304.8	(2400) 1589	(0.001) 0.0254	(0.030) 0.762	(0.025) 0.635	Moderate Transfer	Continuous	(2385) 1580	(>2500) >1644	(4.0) 17.79	(0.003) 0.0762	Negligible	Slight metal on leading side at tip	0.098	Axial and circumferential cracks in rub path propagated to edges. Laminar cracks at ceramic layer interface on one side and one end.

TABLE IV
EROSION TEST SCHEDULE

Test Conditions					Baseline System	Modified System
Temperature		Exposure (Min.)	Impingement Angle			
° K	(° F)		RAD	deg.		
1366	(2000)	20	0.262	(15)	x	
1589	(2400)	20	0.262	(15)	x	x
1589	(2400)	20	1.571	(90)	x	

TABLE V

EROSION TEST DATA SUMMARY

Gas Velocity — 0.35 Mach
 Nozzle to Specimen Distance — 3.81 cm (1.5 in.)

Particulate: Material — Al_2O_3
 Size — 80 Grit
 Flow — 2.72 kg/hr (6.0 lb/hr.)

Test No.	Surface Temp K(F)	Backing Temp K(F)	Impingement Angle RAD (degrees)	R _s 45Y Hardness		Erosion Rate		Specific Erosion (10 ⁻⁴ gm/gm Al ₂ O ₃)	Max. Thick. Change mm(in.)	Remarks
				Avg	(Range)	10 ⁻³ gm/min	10 ⁻³ cc/min			
				Sprayed Graded Y ₂ O ₃ Stabilized ZrO ₂ /CoCrAlY						
1	1366 (2000)	811 (1000)	0.262 (15)	68.2	(62-72)	48.4	9.374	10.8	0.711 (0.028)	Approx. half ceramic layer fractured at 15 min.
2	1584 (2400)	905 (1170)	0.262 (15)	71.0	(67-74)	8.5	1.633	1.87	—	
4	1589 (2400)	889 (1140)	1.571 (90)	73.7	(66-78)	160.7	30.869	35.5	2.54 (0.100)	
Sprayed Graded Y ₂ O ₃ Stabilized ZrO ₂ /CoCrAlY With Increased Porosity Surface Layer										
3	1589 (2400)	890 (1160)	0.262 (15)	64.8	(59-69)	11.1	2.132	2.45	0.305 (0.012)	
Sprayed Graded Y ₂ O ₃ Stabilized ZrO ₂ /CoCrAlY Optimized Configuration No. 11										
5	1589 (2400)	1089 (1500)	0.262 (15)	45.6	(39-62)	16.5	3.169	3.67	—	Complete delamination of ZrO ₂ layer interface after 10 min.

TABLE VI

THERMAL FATIGUE TEST SUMMARY

Config- uration	Test No.	R ₄₅ Y Hardness		Weight Gain		Remarks
		Avg.	Range	gms	%	
Abradability Specimens	1	74.2	67-80	0.0613	0.082	Surface cracks apparent after 15 cycles. "Mud flat" dimensions approx. 0.9525 cm (3/8") x 0.9525 cm (3/8") at center of specimen. Laminar cracks at approx. ceramic layer interface one side and approx. 0.0508 cm (.020") below ceramic layer in intermediate layers other side near center.
	2	74.0	67-82	0.0770	0.102	Surface crack apparent after 4 cycles. "Mud flat" dimensions vary from approx. 0.635 cm (1/4") x 0.9525 cm (3/8") x 0.635 cm (1/2") in center section of specimen. Laminar cracks approx. 0.0762 cm (.030") below ceramic layer interface in intermediate layers both sides near center.
	3	74.2	68-79	0.0089	0.012	Hairline surface cracks apparent after approximately 50 cycles. "Mud flat" size approx. 0.4763 (3/16") x 0.635 cm (1/4"). Fine laminar cracks both sides in ceramic layer just above ceramic layer interface. Fabricated under contract NAS 3-18565.
Erosion Specimens	4	67.8	53-76	0.0553	0.079	Surface cracked into "mud flats" approx. 1.27 cm (1/2") x 1.5875 cm (5/8") to 1.905 cm (3/4") x 1.905 cm (3/4") in less than 25 cycles. Brown and grey spots on surface and one end of ceramic layer - cause not known. Laminar cracking at ceramic interface on thick corner and approx. 0.0762 cm (.030) in intermediate layers on thin corner diagonally opposite.
	5	60.6	46-77	0.0151	0.023	Hairline surface "mud flat" cracks approx. 0.635 cm (1/4") x 0.7938 cm (5/16") apparent after approximately 50 cycles. Laminar cracks at ceramic interface two sides, predominate on one side. Fabricated under contract NAS3-18565.
Configuration No. 11	6	-	-	0.0723	0.114	Surface cracked into "mud flats" approx. 0.9525 cm (3/8") x 0.635 cm (1/2") in center 2/3 of specimen. Laminar cracking at ceramic interface full length of one side and one end and approximately 1/3 length along other side and end.
	7	-	-	0.0384	0.060	Surface cracked into "mud flats" approx. 0.9525 cm (3/8") x 0.635 cm (1/2") or 1.905 cm (3/4"). Laminar cracking full length of all sides at ceramic layer interface.

TABLE VII
AVERAGE LAYER THICKNESSES
THERMAL FATIGUE SPECIMENS
(Z/M = ZrO₂/CoCrAlY)

Layer	NAS3-18565	NAS3-19759
	(Previous Contract) Specimen mm(in)	(Present Contract) Specimen mm (in)
ZrO ₂	1.397 (0.055)	1.651 (0.065)
85/15 Z/M	0.787 (0.031)	0.813 (0.032)
70/30 Z/M	0.762 (0.030)	0.991 (0.039)
40/60 Z/M	0.838 (0.033)	0.787 (0.031)

TABLE VIII
POROSITY* AND METAL VOLUME FRACTIONS OF
THERMAL FATIGUE SPECIMENS
(DETERMINED BY POINT COUNT METHOD)

Specimen	ZrO ₂	85/15 Z/M		70/30 Z/M		40/60 Z/M	
	Porosity %	Porosity %	Metal %	Porosity %	Metal %	Porosity %	Metal %
NAS3-18565 (Previous)	14	10	13	7	37	7	53
NAS3-19759	16	9	14	12	30	5	67

*Porosity results obtained by point count method have been factored by approximately 2 to approximate results rendered through density and analysis of similar structures. The reason for the difference between results of the two methods is unclear. However, pull-out during micropreparation for the metallographic technique (point count) due to incomplete medium infiltration may be a contributing factor.

TABLE IX

**AVERAGE MODULI OF RUPTURE AND ELASTICITY
AND STRAIN TO FAILURE TEST RESULTS**

Material	Test Temperature		Modulus of Rupture		Modulus of Elasticity		Strain To Failure %
	$^{\circ}\text{K}$	$(^{\circ}\text{F})$	10^3N/cm^2	(10^3 psi)	10^3N/cm^2	(10^6 psi)	
40/60 $\text{ZrO}_2/\text{CoCrAlY}$	293	(68)	22.27	(32.3)	5.86	(8.5)	0.82
	1005	(1350)	10.83	(15.7)	9.24	(13.4)	0.39
70/30 $\text{ZrO}_2/\text{CoCrAlY}$	293	(68)	5.63	(8.16)	3.62	(5.25)	0.43
	1061	(1450)	7.03	(10.2)	4.70	(6.81)	0.47
85/15 $\text{ZrO}_2/\text{CoCrAlY}$	293	(68)	4.14	(6.0)	2.54	(3.68)	0.40
	1144	(1600)	4.70	(6.82)	1.86	(2.70)	0.34
ZrO_2	293	(68)	2.82	(4.09)	4.69	(6.8)	0.12
	1589	(2400)	2.24	(3.32)	1.56	(2.26)	0.33

TABLE X

**GEOMETRIC OPTIMIZATION STUDY
CONFIGURATIONS ANALYZED**

Configuration	ZrO ₂		85/15 Z/M		70/30 Z/M		40/60 Z/M		Bond		Mar-M-509	
	mm	(in.)	mm	(in.)	mm	(in.)	mm	(in.)	mm	(in.)	mm	(in.)
Baseline	1.651	(0.065)	0.8128	(0.032)	0.9906	(0.039)	0.7874	(0.031)	0.1016	(0.004)	2.54	(0.100)
No. 1	1.143	(0.045)	0.8128	(0.032)	0.9906	(0.039)	0.7874	(0.031)	0.1016	(0.004)	2.54	(0.100)
No. 2	1.651	(0.065)	1.504	(0.060)	0.9906	(0.039)	0.7874	(0.031)	0.1016	(0.004)	2.54	(0.100)
No. 3	1.651	(0.065)	0.7874	(0.031)	2.032	(0.080)	0.7874	(0.031)	0.1016	(0.004)	2.54	(0.100)
No. 4	1.651	(0.065)	0.8128	(0.032)	0.9906	(0.039)	1.524	(0.060)	0.1016	(0.004)	2.54	(0.100)
No. 5	1.651	(0.065)	0.8128	(0.032)	0.9906	(0.039)	0.7874	(0.031)	0.1016	(0.004)	3.81	(0.150)
No. 6	2.286	(0.90)	0.762	(0.030)	0.381	(0.015)	0.381	(0.015)	0.1016	(0.004)	2.54	(0.100)
No. 7	3.048	(0.120)	0.8128	(0.032)	--	--	0.381	(0.015)	0.1016	(0.004)	2.54	(0.100)
No. 8	3.048	(0.120)	0.8128	(0.032)	--	--	0.381	(0.015)	0.1016	(0.004)	1.27	(0.050)
No. 9	2.286	(0.090)	0.8128	(0.032)	--	--	0.381	(0.015)	0.1016	(0.004)	1.27	(0.050)
No. 10	2.286	(0.090)	0.762	(0.030)	0.381	(0.015)	0.381	(0.015)	0.1016	(0.004)	1.27	(0.050)
No. 11	2.286	(0.090)	0.762	(0.030)	--	--	0.8128	(0.030)	0.1016	(0.004)	1.27	(0.050)
No. 12	2.286	(0.090)	0.762	(0.030)	0.8128	(0.030)	0.381	(0.015)	0.1016	(0.004)	1.27	(0.050)

- Notes: 1. Z/M = ZrO₂ - CoCrAlY, preceding numerals indicate weight ratio of constituents in spray powder.
 2. Bond coat is sprayed NiCrAl material and was analyzed as an integral part of the substrate.

TABLE XI
GEOMETRIC OPTIMIZATION STUDY
SUMMARY OF RESULTS

NOTE: NEGATIVE NOS. INDICATE COMPRESSIVE STRESSES

Config- uration	Thermal Cycle Point	σ_{11}	σ_{12}	σ_{21}	Max 2-D Circumferential Stress, N/cm ²								Temperature, °K						Remarks
					σ_{22}	σ_{31}	σ_{32}	σ_{41}	σ_{42}	σ_{51}	σ_{52}	t_1	t_2	t_3	t_4	t_5	t_6		
Base- line	12 Sec. Decel	5852	2490	-1466	-924	-3321	-559	1158	8004	-5986	-2504	953 (1573)	1203 (1248)	1045 (1150)	950 (1044)	839 (962)	805 (945)	Temps. in paranthesis () are at SLTO for Configs. 1 – 7	
1	12 Sec. Decel	6572	3849	- 785	-623	-2603	-459	1194	8344	-6599	-2548	255 (1568)	1065 (1304)	1038 (1192)	951 (1068)	847 (970)	810 (950)		
2	12 Sec. Decel	6501	1771	-2653	-1139	-3529	-728	1114	8408	-5929	-1872	955 (1575)	1137 (1575)	1052 (1129)	948 (1033)	834 (958)	803 (943)		Circ. deflections: B/L 0.047 mm
3	12 Sec. Decel	7295	2226	-2206	-2155	-6459	- 94	2049	9666	-3374	- 942	962 (1576)	1149 (1298)	1127 (1217)	401 (1031)	837 (957)	805 (943)		
4	12 Sec. Decel	7229	2529	-1977	-1660	-6252	-4387	-7793	9934	-4585	-1378	962 (1575)	1128 (1026)	1099 (1194)	1029 (1102)	837 (959)	802 (944)	Config. 8 0.030 mm 9 0.024 mm	
5	12 Sec. Decel	7547	3610	- 908	-414	-2173	299	1768	8150	-8777	-1349	952 (1573)	1099 (1251)	1058 (1154)	971 (1051)	871 (970)	788 (945)		
6	12 Sec. Decel	5091	3158	- 142	849	1245	2713	4121	8326	-9239	-3555	953 (1574)	1770 (1140)	929 (1041)	881 (999)	828 (960)	799 (944)		
7	12 Sec. Decel	4379	3729	665	2106				7367	-7725	-3167	962 (1578)	983 (1079)	874 (986)		821 (953)	794 (947)		
8	12 Sec. Decel	2941	2502	221	1829				6969	-5994	-4205	962	963	843		784	770		
	Idle	-4200	1768	1109	1777				6115	3454	1946	846	574	509		481	477		
	6 Sec. Accel.	-11347	5565	3196	3630				10377	5204	2784	1510	593	557		560	567		
9	SLTO	-3055	6138	2277	3592				11712	-7757	-5703	1578	1075	981		947	940		
	12 Sec. Decel.	3006	2509	138	1675				6269	-7509	-5342	949	958	844		786	773		
	SLTO	-2541	5242	1769	3345				11477	-7440	-5612	1573	1108	995		953	945		
10	12 Sec. Decel	3188	1825	- 701	452		1427		6410	-7096	-4978	952	995	903	849	789	775		
	SLTO	-2697	4459	889	2297		5415		11484	-7556	-5546	1574	1133	1035	992	952	944		
	12 Sec. Decel	3269	1884	-663	488			-165	6672	-6840	-4780	952	995	903		789	775		
11	Idle	-4340	598	299	1006				3720	6705	2527	1363	842	613	548		485	480	
	6 Sec. Accel.	-11386	3536	2093	2916				9665	10206	4767	2524	1510	646	579	562	569		
	SLTO	-2716	4437	869	2282			5875	11533	-7654	-5621	1574	1133	1035		952	944		
12	12 Sec. Decel.	3545	1235	-1471	-512	-1427	1638		6878	-6023	-4133	956	1034	956	853	790	777		
	Idle	-4169	327	- 61	576	1909	2939		5986	3104	1659	844	630	571	513	483	479		
	6 Sec. Accel	-11335	3180	1790	2648	5501	6123		10326	5100	2668	1510	660	591	558	560	568		
	SLTO	-2757	3690	67	1418	3255	5640		11680	-7510	-5544	1575	1160	1069	989	950	943		

TABLE XI (Cont'd)
GEOMETRIC OPTIMIZATION STUDY
SUMMARY OF RESULTS

NOTE: NEGATIVE NOS. INDICATE COMPRESSIVE STRESSES

Config- uration	Thermal Cycle Point	σ_{11}	σ_{12}	σ_{21}	Max 2-D Circumferential Stress, psi								Temperature, °F				t_5	t_6	Remarks
					σ_{22}	σ_{31}	σ_{32}	σ_{41}	σ_{42}	σ_{51}	σ_{52}	t_1	t_2	t_3	t_4				
Base- line	12 Sec. Decel	8488	3612	-2126	-1340	-4816	- 811	1680	11609	- 8681	-3632	1256 (2372)	1505 (1787)	1422 (1611)	1251 (1420)	1051 (1271)	989 (1242)	Temps. in parenthesis () are at SLTO for Configs. 1 – 7	
1	12 Sec. Decel	9532	5582	-1139	- 903	-3775	- 666	1732	12101	- 9570	-3695	1251 (2363)	1458 (1888)	1409 (1685)	1252 (1463)	1054 (1287)	998 (1251)		
2	12 Sec. Decel	9428	2569	-3848	-1652	-5118	-1056	1615	12194	- 8599	-2715	1268 (2376)	1586 (1866)	1434 (1573)	1246 (1400)	1041 (1264)	985 (1238)		
3	12 Sec. Decel	10580	3228	-3199	-3125	-9367	- 136	2971	14019	- 4893	-1366	1271 (2377)	1608 (1876)	1569 (1730)	1267 (1396)	1047 (1263)	989 (1237)	Circ. deflections: B/L 1.85×10^{-3} in.	
4	12 Sec. Decel	10484	3668	-2868	-2408	-9068	-6363	-11302	14408	- 6650	-1999	1271 (2375)	1571 (1846)	1519 (1689)	1393 (1523)	1046 (1266)	989 (1239)		
5	12 Sec. Decel	10945	5235	-1317	- 601	-3151	433	2564	11820	-12729	-1956	1254 (2372)	1519 (1792)	1445 (1618)	1288 (1432)	1108 (1286)	958 (1242)		Config. 8 1.18×10^{-3} in. 7 0.96×10^{-3} in.
6	12 Sec. Decel	7383	4580	- 206	1231	1805	3935	7427	12075	-13400	-5156	1256 (2374)	1363 (1592)	1213 (1414)	1126 (1338)	1031 (1268)	979 (1239)		
7	12 Sec. Decel	6351	5408	965	3054				10684	-11204	-4593	1271 (2381)	1310 (1482)	1113 (1315)		1018 (1255)	970 (1245)		
8	12 Sec. Decel	4266	3629	320	2652				10107	- 8693	-6098	1272	1273	1057		951	927		
	Idle	- 6092	2564	1609	2577				8869	5009	2823	1063	573	457		406	399		
	6 Sec. Accel.	-16457	8071	4635	5264				15050	7548	4038	2259	608	542		548	561		
9	SLTO	- 4402	8902	3303	5209				16986	-11250	-8271	2381	1475	1306		1245	1233		
	12 Sec. Decel.	4360	3639	200	2429				9092	-10891	-7748	1248	1265	1060		955	932		
	SLTO	- 3685	7602	2566	4852				16645	-10791	-8146	2372	1535	1331		1255	1242		
10	12 Sec. Decel.	4623	2647	-1016	656		2069		9297	-10292	-7220	1254	1331	1166	1069	960	936		
	SLTO	- 3912	6467	1290	3331		7854		16655	-10958	-8043	2374	1580	1404	1326	1253	1240		
	12 Sec. Decel.	4741	2733	- 961	708		- 240		9677	- 9920	-6933	1254	1331	1166		960	936		
11	Idle	- 6294	868	433	1459				5395	9725	3665	1056	643	527		413	405		
	6 Sec. Accel.	-16514	5129	3035	4229				14017	14802	6914	3660	2258	703	583	552	564		
	SLTO	- 3939	6435	1268	3310				8520	16727	-11101	-8153	2374	1580	1404	1253	1240		
12	12 Sec. Decel.	5141	1791	-2134	- 742	-2070	2376		9976	- 8735	-5994	1261	1402	1261	1076	963	938		
	Idle	- 6046	474	- 89	835	2768	4263		8682	4502	2406	1060	674	568	464	409	402		
	6 Sec. Accel.	-16439	4612	2596	3840	7978	8881		14976	7396	3869	2258	728	604	545	549	562		
	SLTO	- 3998	5351	97	2057	4721	8180		16940	-10892	-8041	2376	1628	1464	1320	1251	1238		

TABLE XII

OPTIMIZED CONFIGURATION EROSION SPECIMEN MEASURED LAYER THICKNESS

Layer	1		2		3		4		Average	
	mm	(in)	mm	(in)	mm	(in)	mm	(in)	mm	(in)
Bond Coat	0.1473	(0.0058)	0.1092	(0.0043)	0.1321	(0.0052)	0.0965	(0.0038)	0.1219	(0.0048)
40/60 ZrO ₂ /CoCrAlY	0.8534	(0.0336)	0.7544	(0.0297)	0.7061	(0.0278)	0.5969	(0.0235)	0.7290	(0.0287)
85/15 ZrO ₂ /CoCrAlY	0.6325	(0.0249)	0.7544	(0.0297)	0.7315	(0.0288)	0.6325	(0.0249)	0.6883	(0.0271)
ZrO ₂	3.3071	(0.1302)	3.2101	(0.1264)	3.0277	(0.1192)	2.6111	(0.1028)	3.0404	(0.1197)
Total	4.9403	(0.1945)	4.8285	(0.1901)	4.5974	(0.1810)	3.937	(0.1550)	4.5771	(0.1802)

TABLE XIII

OPTIMIZED CONFIGURATION THERMAL FATIGUE MEASURED LAYER THICKNESS

Layer	TRANSVERSE LOCATION									
	1		2		3		4		5	
	mm	(in)	mm	(in)	mm	(in)	mm	(in)	mm	(in)
Bond Coat	0.1219	(0.0048)	0.1219	(0.0048)	0.1219	(0.0048)	0.1092	(0.0043)	0.0965	(0.0038)
40/60 ZrO ₂ /CoCrAlY	0.7315	(0.0288)	0.7544	(0.0297)	0.7036	(0.0277)	0.7315	(0.0288)	0.5105	(0.0201)
85/15 ZrO ₂ /CoCrAlY	0.7188	(0.0283)	0.8052	(0.0317)	0.7188	(0.0283)	0.7925	(0.0312)	0.9627	(0.0379)
ZrO ₂	2.4663	(0.0971)	2.4892	(0.0980)	2.5984	(0.1023)	2.7203	(0.1071)	2.9032	(0.1143)
Total	4.0386	(0.1590)	5.1707	(0.1642)	4.1986	(0.1653)	4.3536	(0.1714)	4.4729	(0.1761)

Layer	CIRCUMFERENTIAL LOCATION									
	1		2		3		4		5	
	mm	(in)	mm	(in)	mm	(in)	mm	(in)	mm	(in)
Bond Coat	0.1219	(0.0048)	2.1219	(0.0048)	0.1219	(0.0048)	0.0965	(0.0038)	0.1092	(0.0043)
40/60 ZrO ₂ /CoCrAlY	0.780	(0.0307)	0.7544	(0.0297)	0.8153	(0.0321)	0.7188	(0.0283)	0.8052	(0.0317)
85/15 ZrO ₂ /CoCrAlY	0.6934	(0.0273)	0.6934	(0.0273)	0.7315	(0.0288)	0.7544	(0.0297)	0.9017	(0.0355)
ZrO ₂	2.5019	(0.0985)	2.4511	(0.0965)	2.4511	(0.0965)	2.7686	(0.1090)	2.6848	(0.1057)
Total	4.0970	(0.1613)	4.0208	(0.1583)	4.0945	(0.1612)	4.3383	(0.1708)	4.5009	(0.1772)

TABLE XIV

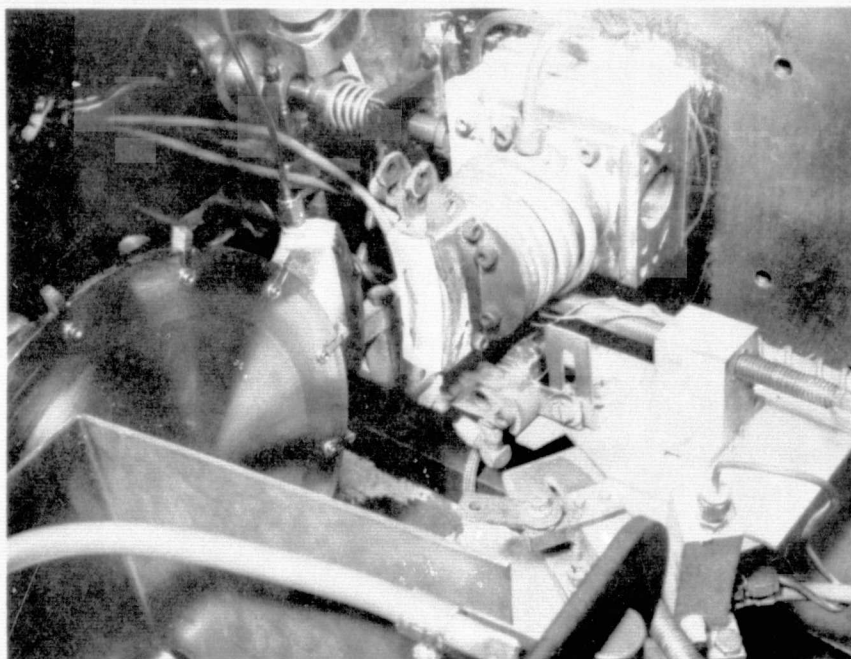
***POROSITY(%) AND METAL CONTENT (V/OM) OF COMPOSITE LAYERS DETERMINED BY A POINT COUNT METHOD FOR AS-SPRAYED OPTIMIZED CONFIGURATION**

Metco 202NS % Porosity	Layer			
	85/15 ZrO ₂ /CoCrAlY		40/60 ZrO ₂ /CoCrAlY	
	% Porosity	v/oM	% Porosity	v/oM
15	9	23	5	61

*The porosity results obtained by point count have been factored by 2 to approximate results rendered through density analysis of similar structures. While the reason for the difference in results of the two methods is unclear, pull-out during micropreparation for the point count procedure due to incomplete medium infiltration may be a factor.

	MATERIAL *	DESIGN
		THICKNESS
		MM (IN.)
NOTES: * - NUMERALS INDICATE SPRAY POWDER WEIGHT PERCENT YSZ & CoCrAlY YSZ = Y_2O_3 STABILIZED ZrO_2 (19% YTTRIA)	YSZ	1.651/1.397 (0.065/0.055)
	85/15 YSZ/CoCrAlY	0.889/0.635 (0.035/0.025)
	70/30 YSZ/CoCrAlY	0.889/0.635 (0.035/0.025)
	40/60 YSZ/CoCrAlY	0.889/0.635 (0.035/0.025)
	NiCrAl	0.127/0.0762 (0.005/0.003)
	Mar-M-509	2.794/2.286 (0.110/0.090)

Figure 1 Plasma Sprayed Graded Layered Y_2O_3 Stabilized ZrO_2 /CoCrAlY Seal System



Note: Near side heating torch not shown.

Figure 2 High Temperature Abradability Test Rig

ORIGINAL PAGE IS
OF POOR QUALITY

SEAL TEMP. — 1589K (2400F)
NO. BLADES — 12
BLADE MAT'L. — PWA 1455
BLADE TIP TKNS. — 0.3175 CM (0.125 IN.)

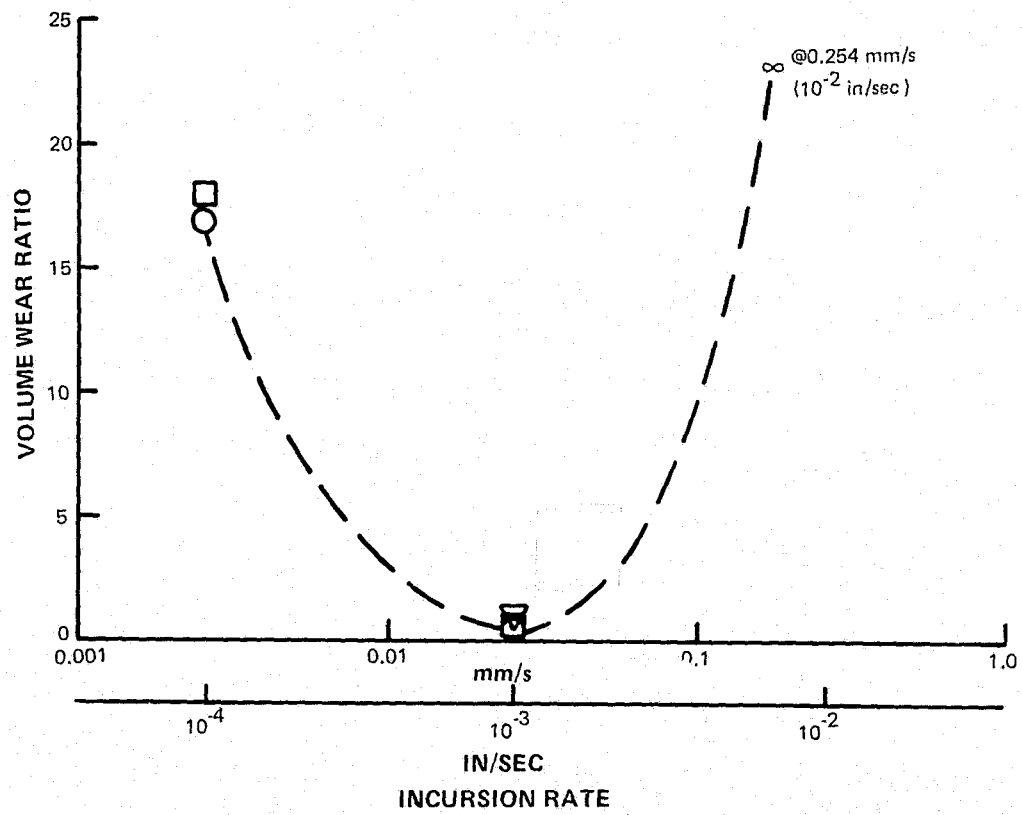
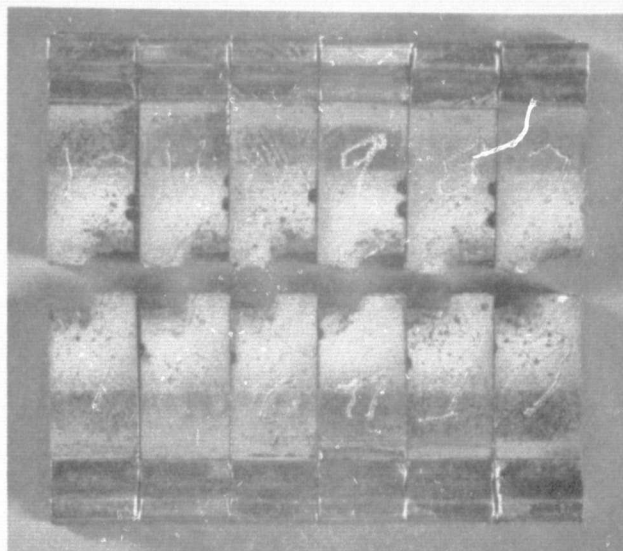
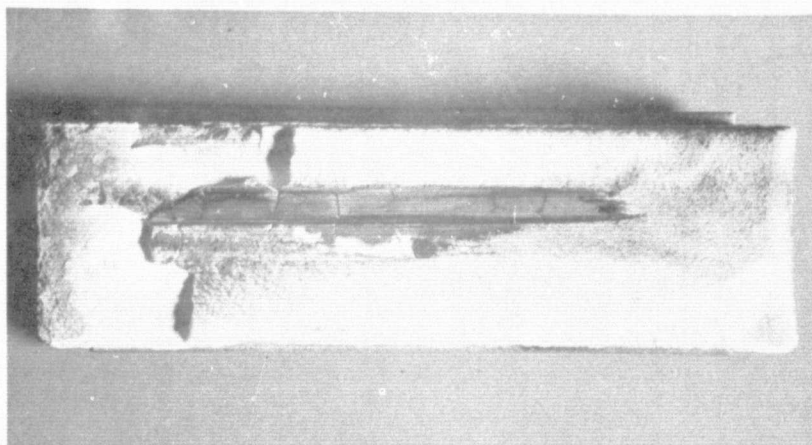


Figure 3 Abradability Sensitivity to Incursion Rate



Note: Leading face of blades shown.

Figure 4 Abnormal Blade Tip Wear (Abradability Test No. 1)



Rub Direction

Note: Spallation at lower end and upper corner due to thermal shocking while setting test conditions. Excessive windage necessitated approx. 8 heating and cooling cycles before achieving test conditions.

Figure 5 Test Specimen (Abradability Test No. 1)

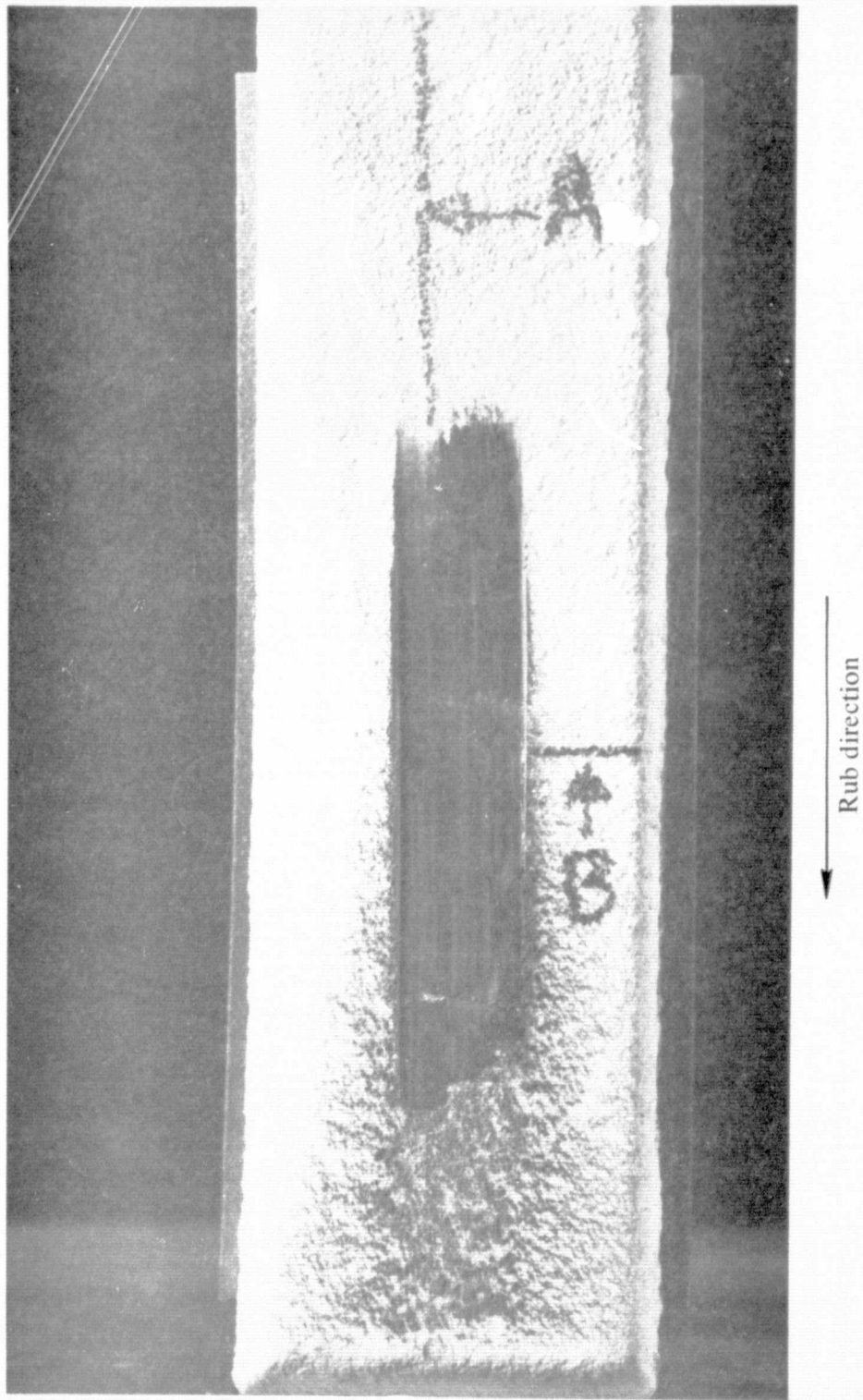


Figure 6 Axial Cracks in Rub Path, (Abradability Test No. 3)

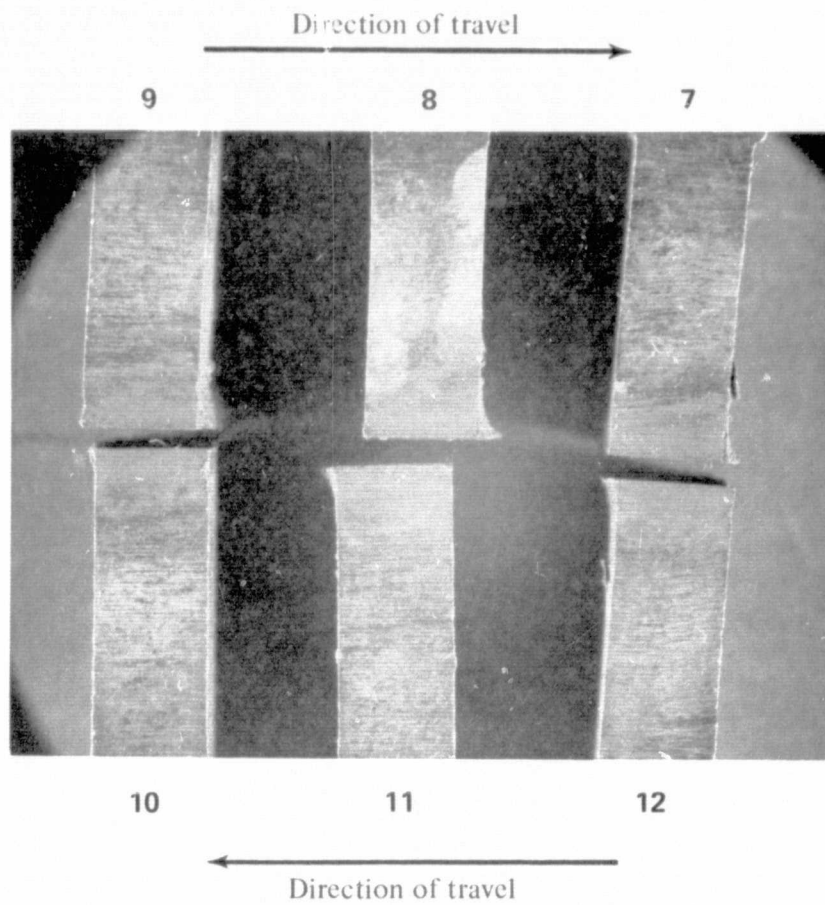


Figure 7 *Metal Pickup on Leading Side of Blades, (Abradability Test No. 6)*

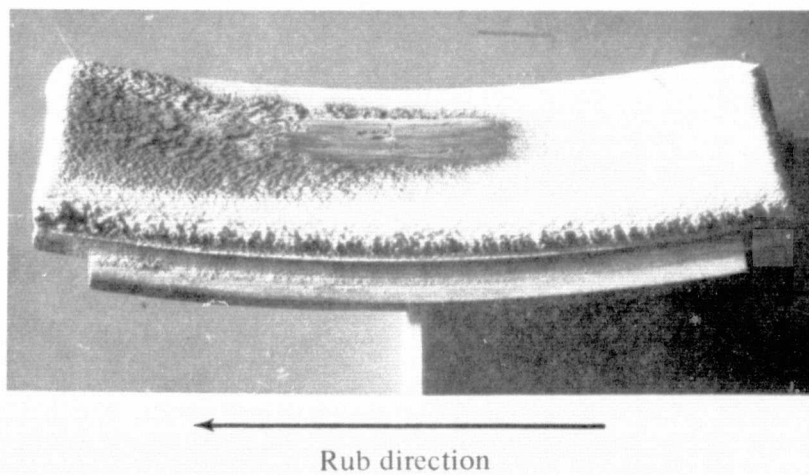
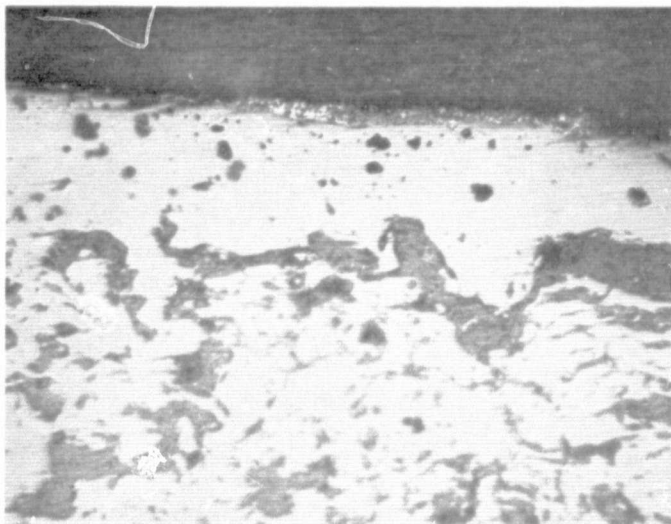


Figure 8 *Metal Deposits on Seal Specimen Downstream of Rubbed Area, (Abradability Test No. 6)*



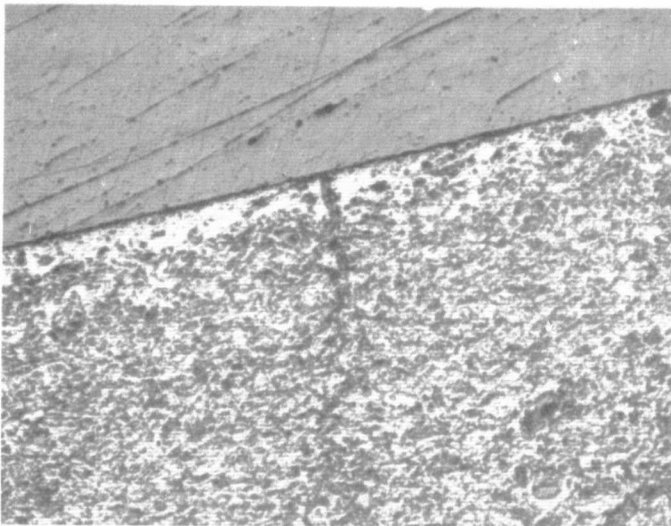
500X

A

Densification observed at surface
of rub path .002-.004 in.

Deposit (transfer) remnants also
observed at surface approx.
.00024 in. thick

Rub direction 
Observation direction 



100X

B

Densification observed along length
of rub path

Crack origin appears to be at surface



Rub direction 
Observation direction 

Figure 9 Metal Transfer and Seal Densification in Rub Path, (Abradability Specimen No. 3)

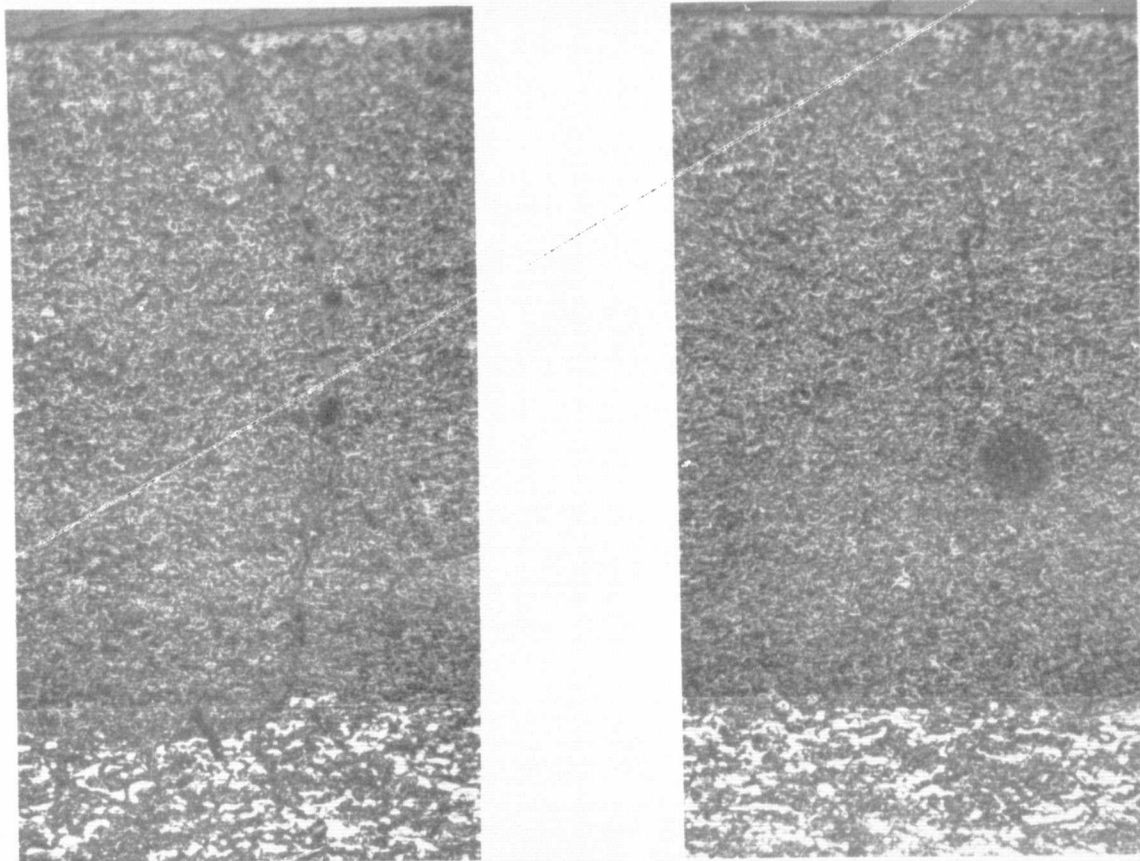


Figure 10 Typical Cracks in Circumferential Section, (Abradability Test No. 3)

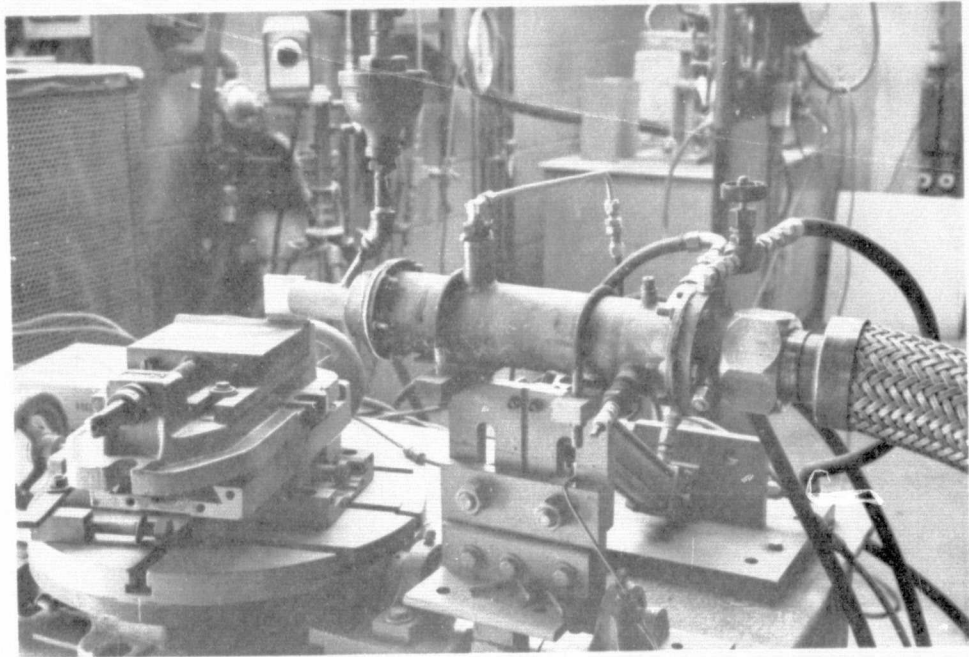


Figure 11 Hot Particulate Erosion Rig

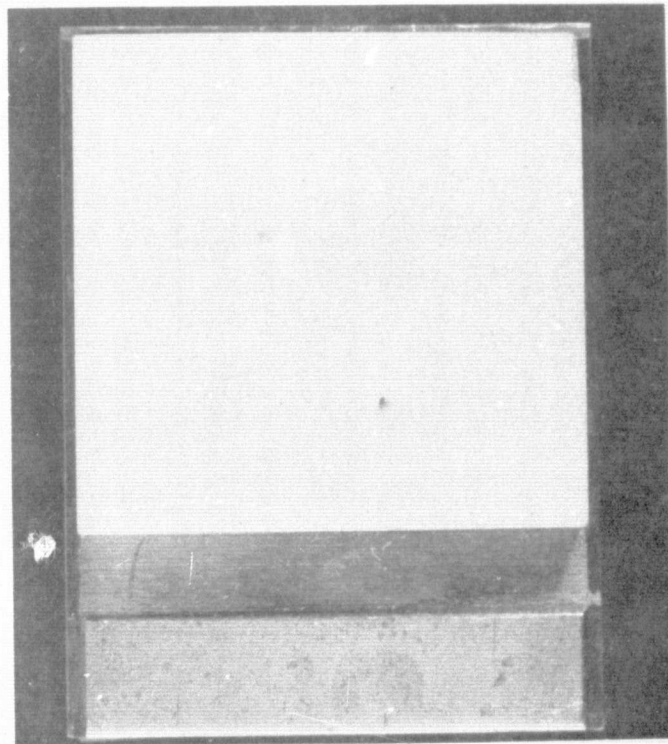
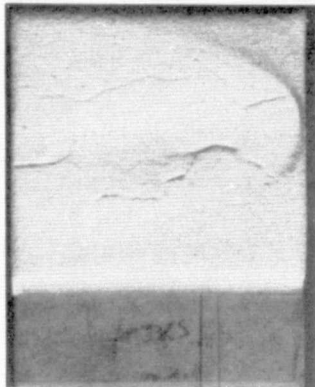


Figure 12 Erosion Test Specimen

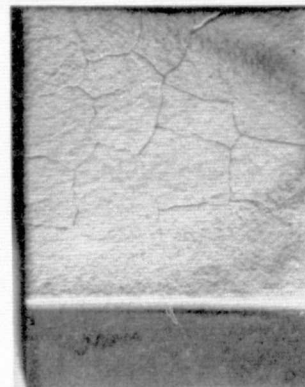
TEST CONDITIONS:

SURFACE TEMP. — AS NOTED
 IMPINGEMENT ANGLE — AS NOTED
 PARTICULATE — NO. 80 GRIT Al_2O_3
 PARTICULATE FLOW — 6.0 LB/HR.

TEST DURATION — 20 MIN.
 GAS VELOCITY — 0.35 MACH.
 NOZZLE DIAMETER — 0.75 IN.
 STANDOFF DISTANCE — 1.5 IN. @ Q

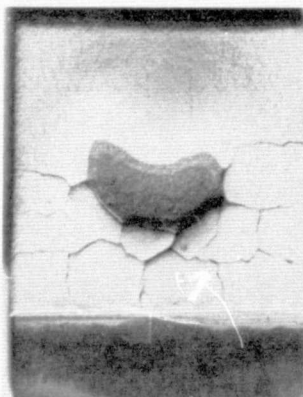


2000°F 15°
TEST NO. 1



2400°F 15°
TEST NO. 2

TOP HALF OF CERAMIC LAYER
 DELAMINATED AND SPALLED AT
 INTERMEDIATE LAYER INTERFACE
 AFTER 15 MINUTES.



2400°F 90°
TEST NO. 4

BOTTOM HALF OF CERAMIC LAYER
 FRACTURED AT INTERMEDIATE LAYER
 INTERFACE WHEN ACCIDENTALLY
 DROPPED POST TEST.



2400°F 15°
TEST NO. 3

INCREASED POROSITY SURFACE
 LAYER.

Figure 13 Tested Erosion Specimens

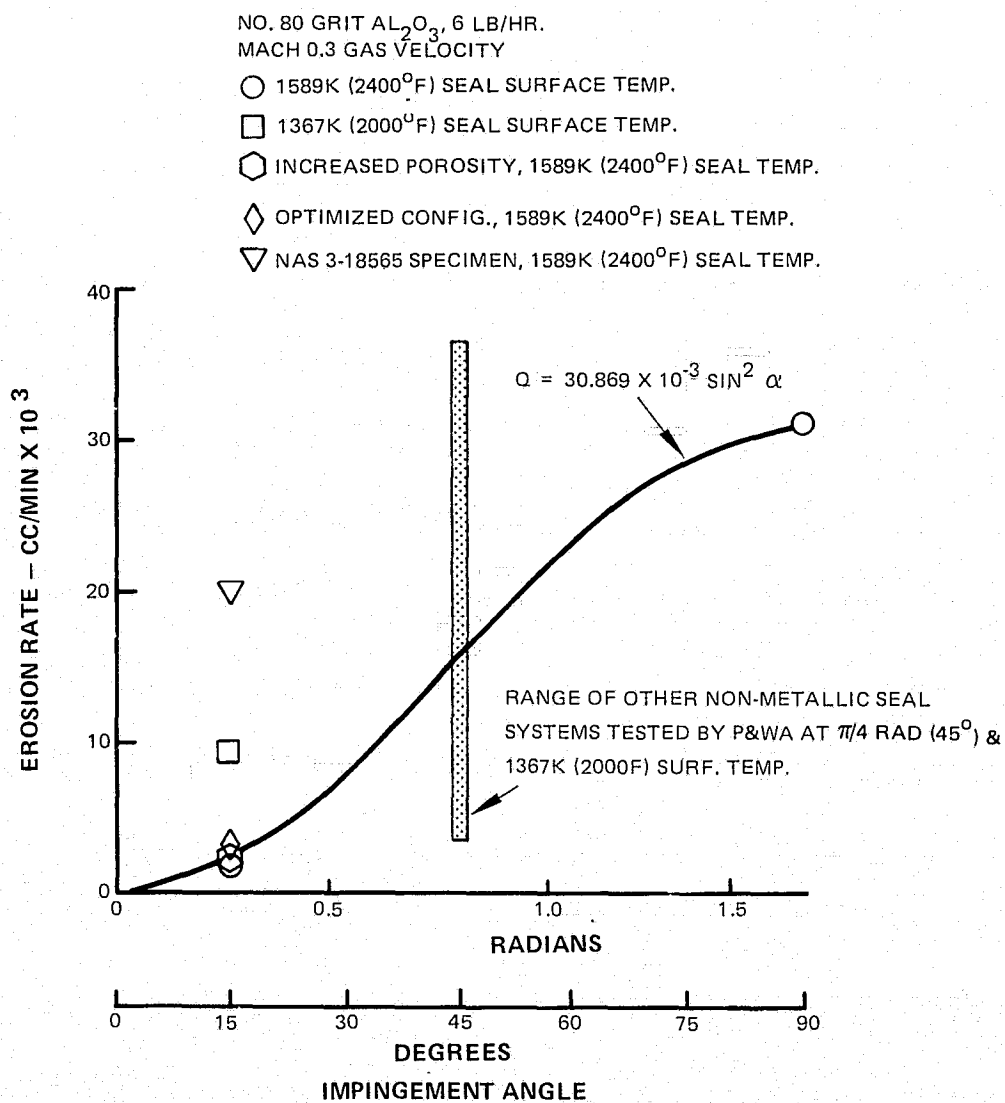


Figure 14 Erosion Test Data Correlation

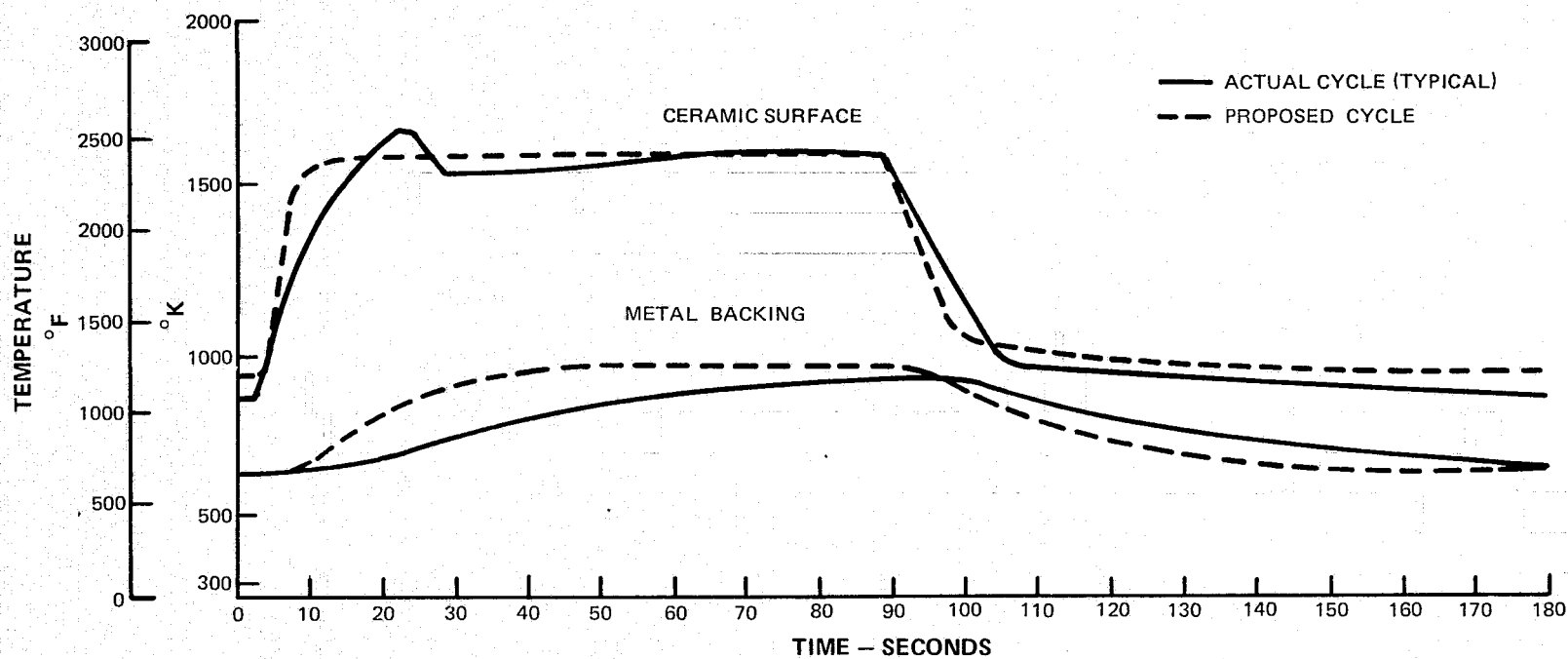


Figure 15 Thermal Fatigue Test Cycle, Abradability Specimen

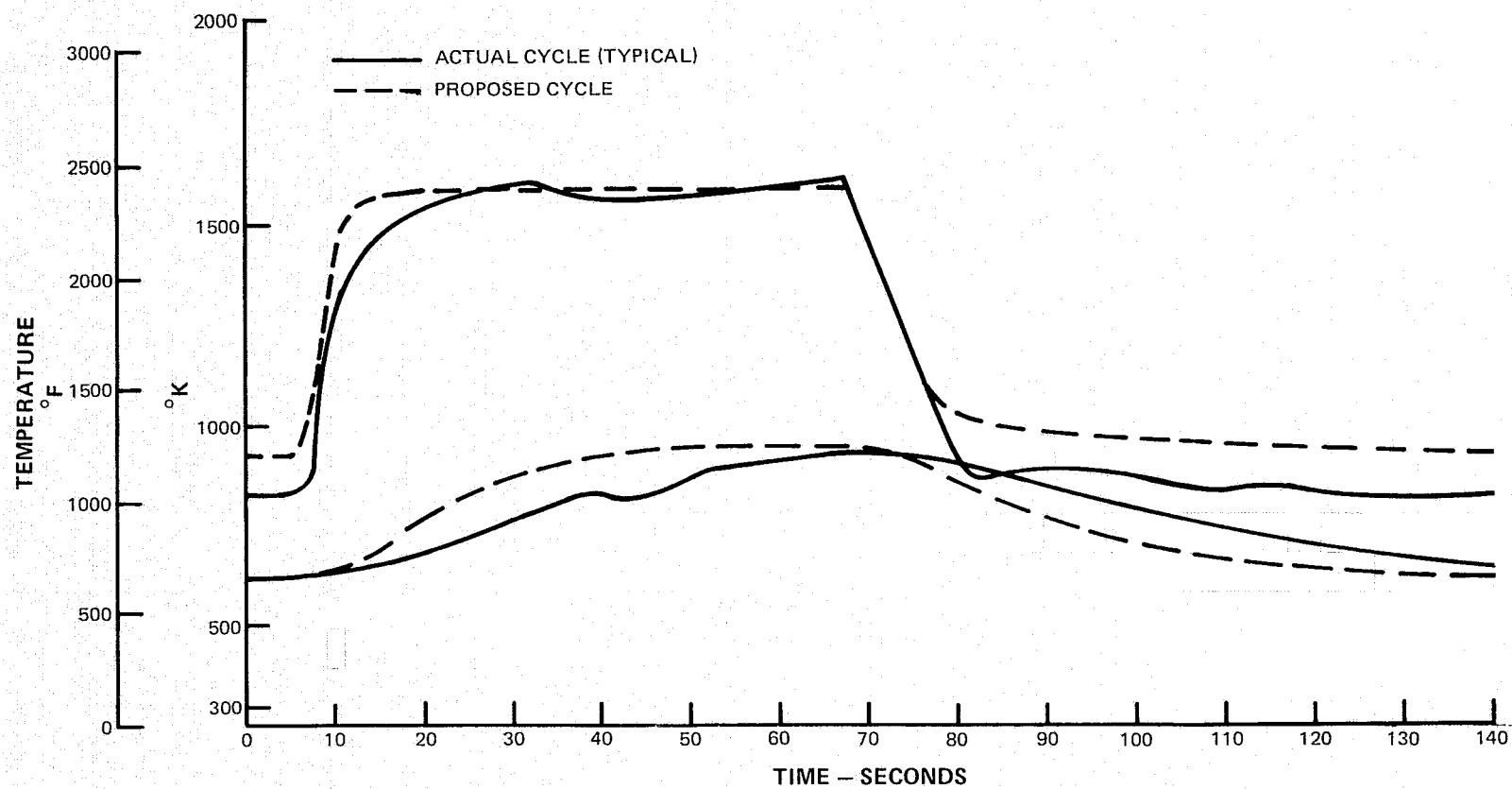
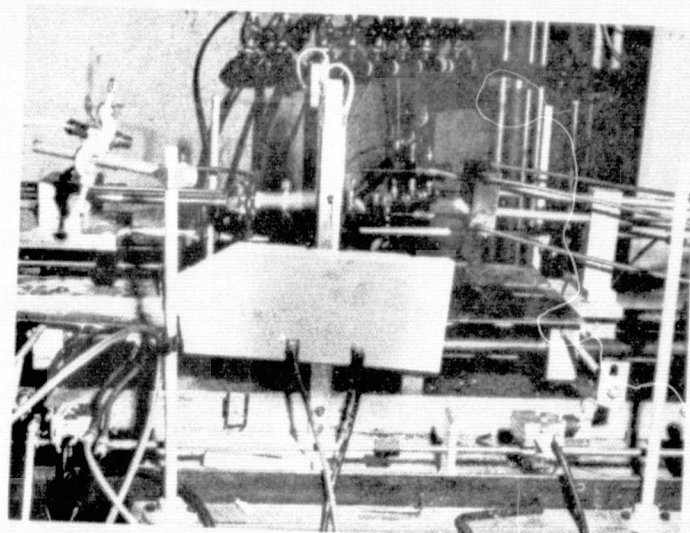
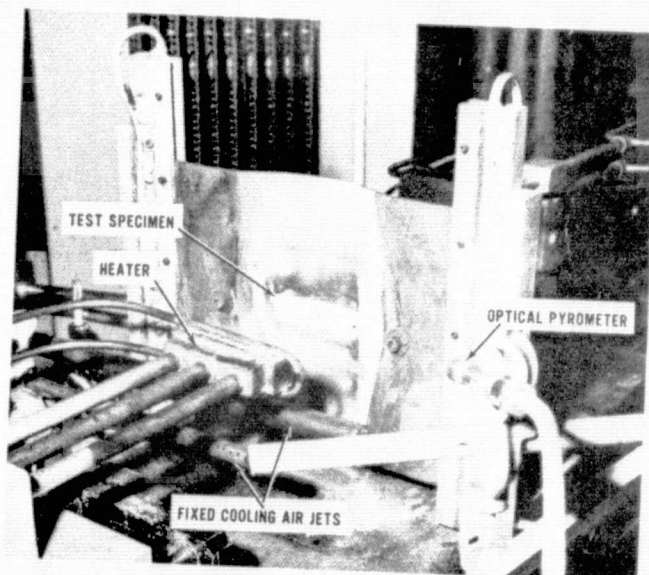


Figure 16 Thermal Fatigue Test Cycle, Erosion Specimen

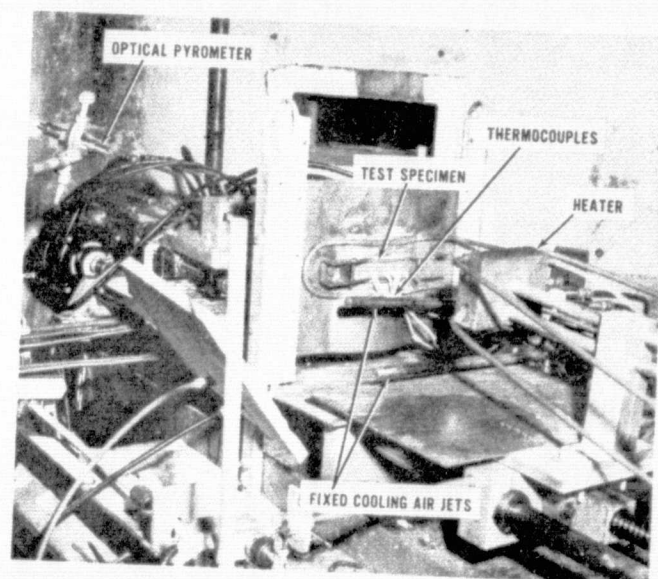


(X-43729-A)



FRONT VIEW

(X-43732-A)



BACK VIEW

(X-43731-A)

Figure 17 Thermal Fatigue Test Rig

ORIGINAL PAGE IS
OF POOR QUALITY

THERMAL CYCLE:

MAX. TEMP.: SURFACE - 1617°K (2450°F) BACK - 944°K (1240°F)
MIN. TEMP.: SURFACE - 839°K (1050°F) BACK - 600°K (620°F)
MAX. GRADIENT: 1142°K (1595°F) @ 24 SEC. INTO HEATUP
CYCLE DURATION: HEATING - 88 SEC. COOLING - 92 SEC.
NO. CYCLES: 100

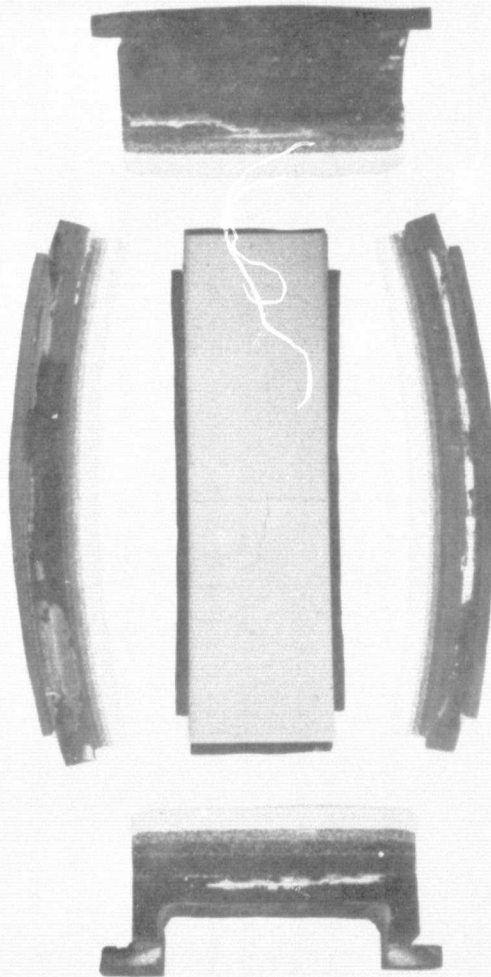


Figure 18 Thermal Fatigue Specimen (Test No. 1)

THERMAL CYCLE:

MAX. TEMP.: SURFACE — 1600°K (2420°F) BACK — 917°K (1190°F)
MIN. TEMP.: SURFACE — 855°K (1080°F) BACK — 630°K (675°F)
MAX. GRADIENT: 1236°K (1765°F) @ 20 SEC. INTO HEATUP
CYCLE DURATION: HEATING — 96 SEC. COOLING — 84 SEC.
NO. CYCLES: 100

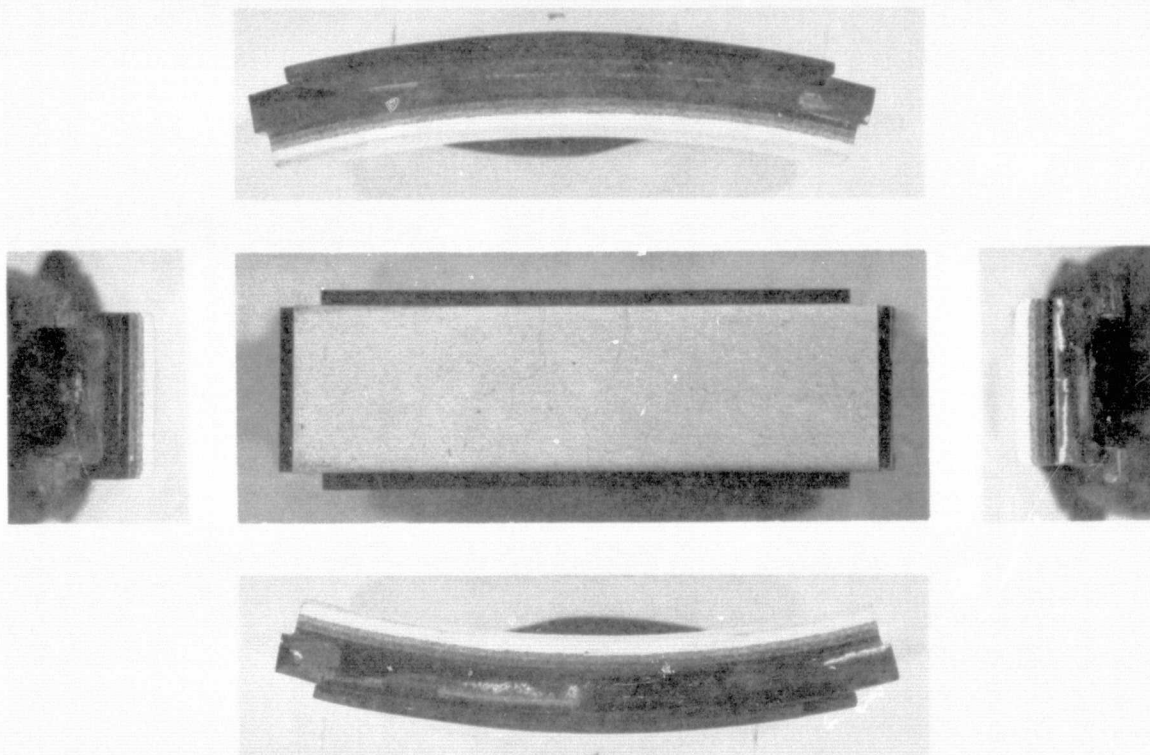


Figure 19 Thermal Fatigue Specimen (Test No. 2)

ORIGINAL PAGE
OF POOR QUALITY

THERMAL CYCLE:
MAX. TEMP.: SURFACE — 1644° K (2500° F) BACK — 939° K (1230° F)
MIN. TEMP.: SURFACE — 867° K (1100° F) BACK — 644° K (700° F)
MAX. GRADIENT: 1136° K (1585° F) @ 20 SEC. INTO HEATUP
CYCLE DURATION: HEATING — 85 SEC. COOLING — 95 SEC.
NO. CYCLES: 100

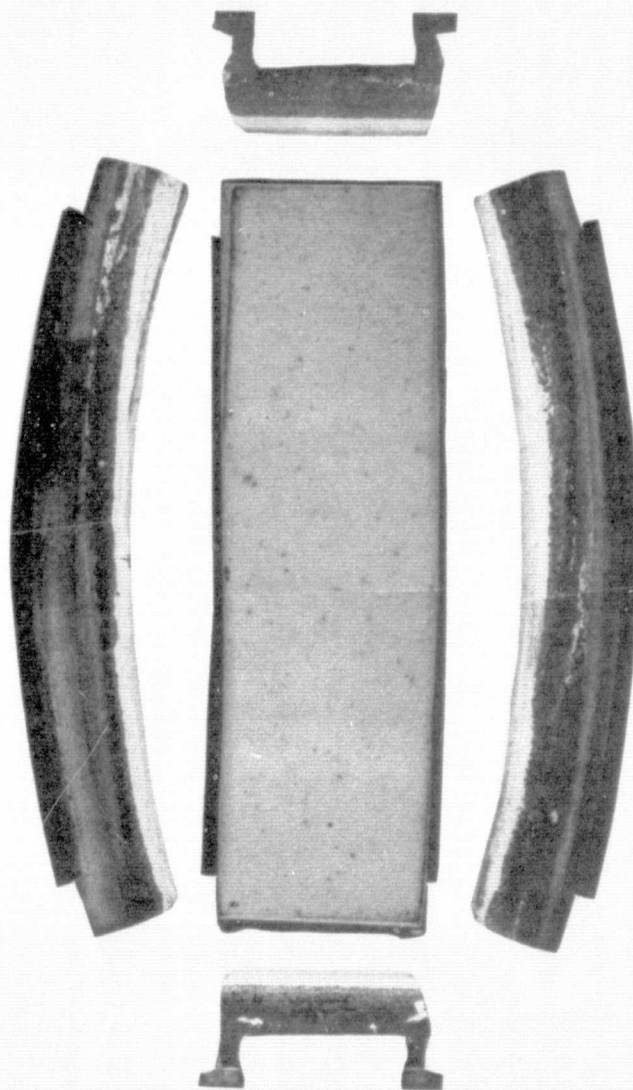


Figure 20 Thermal Fatigue Specimen (Test No. 3)

THERMAL CYCLE

MAX. TEMP.: SURFACE - 1555°K (2340°F) BACK - 922°K (1200°F)
MIN. TEMP.: SURFACE - 811°K (1000°F) BACK - 644°K (700°F)
MAX. GRADIENT: 1030°K (1395°F) @ 22.5 SEC. INTO HEAT UP
CYCLE DURATION: HEATING - 75 SEC. COOLING - 68 SEC.
NO. CYCLES: 100

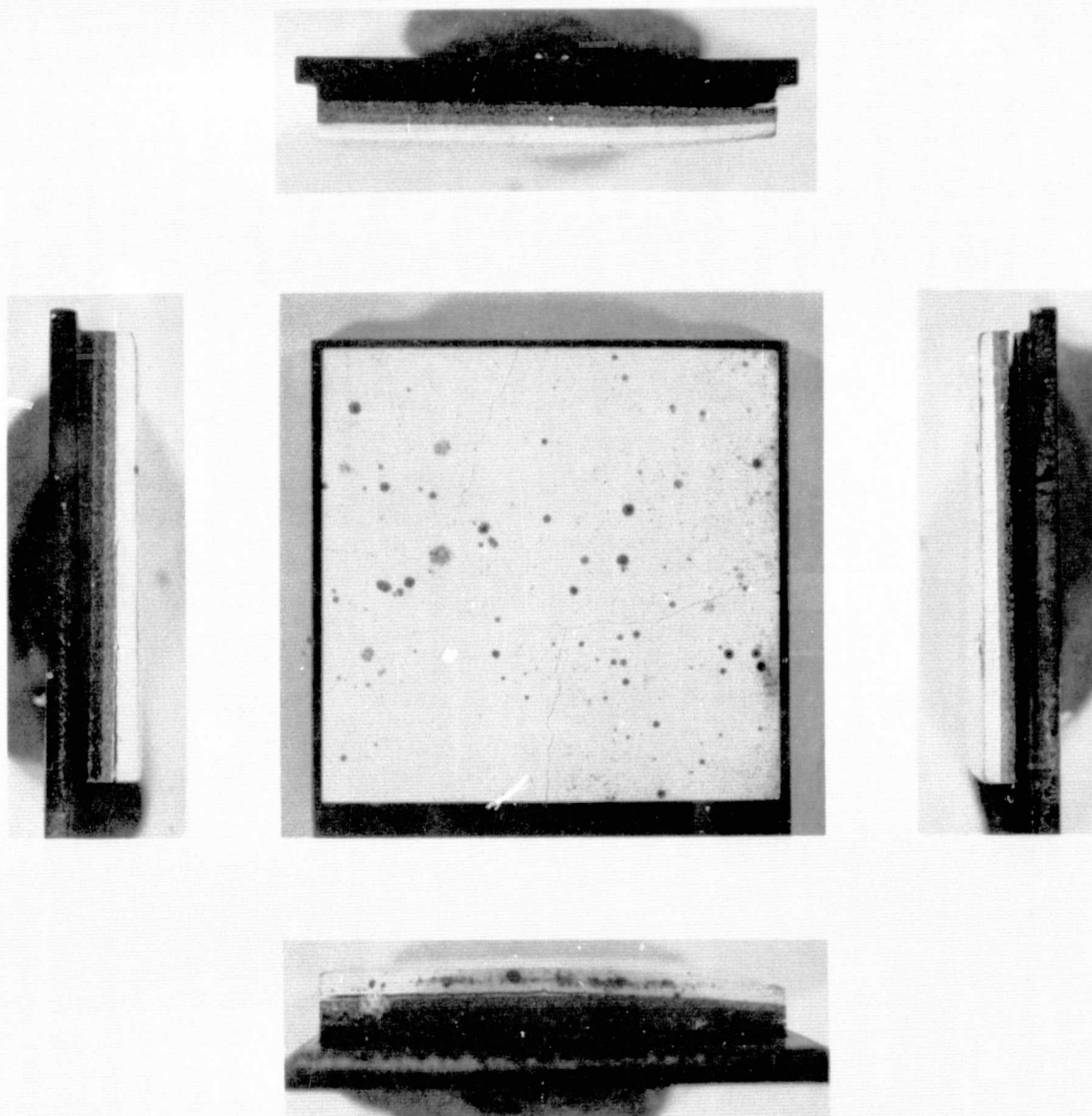


Figure 21 Thermal Fatigue Specimen (Test No. 4)

THERMAL CYCLE:

MAX. TEMP.: SURFACE — 2695°K (2440°F) BACK — 1465°K (1210°F)

MIN. TEMP.: SURFACE — 1275°K (1020°F) BACK — 617°K (650°F)

MAX. GRADIENT: 1119°K (1555°F) @ 17.5 SEC. INTO HEATUP

CYCLE DURATION: HEATING — 63 SEC. COOLING — 80 SEC.

NO. CYCLES: 100

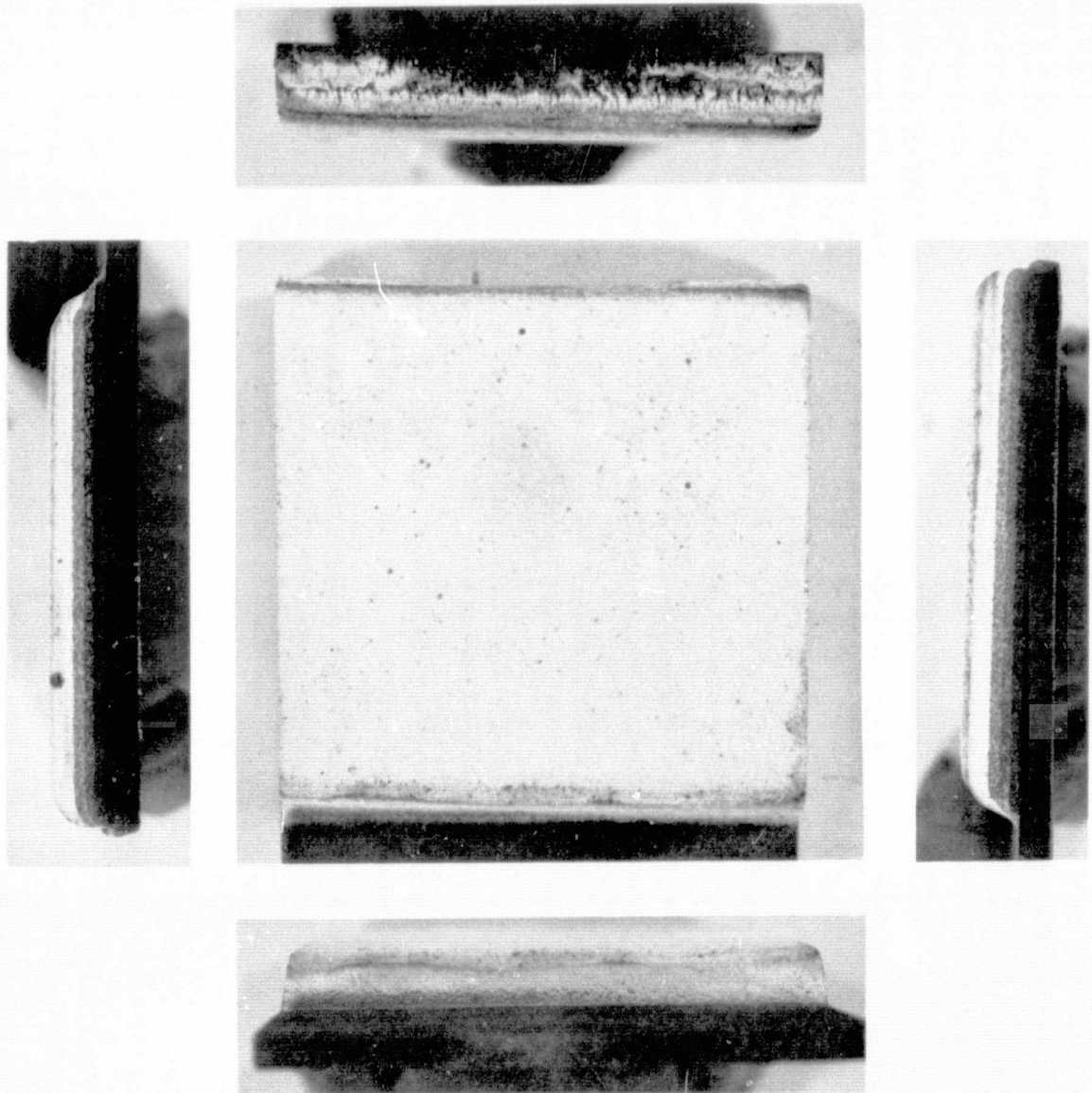
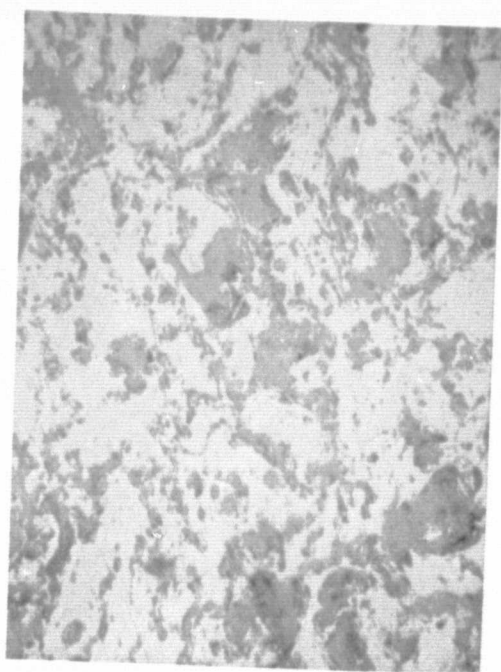
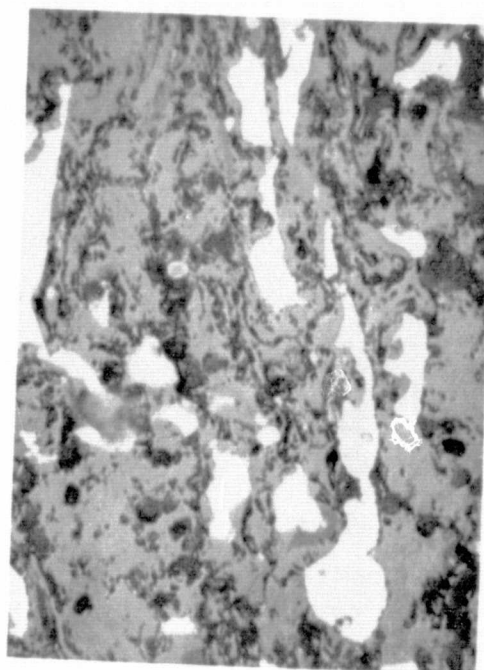


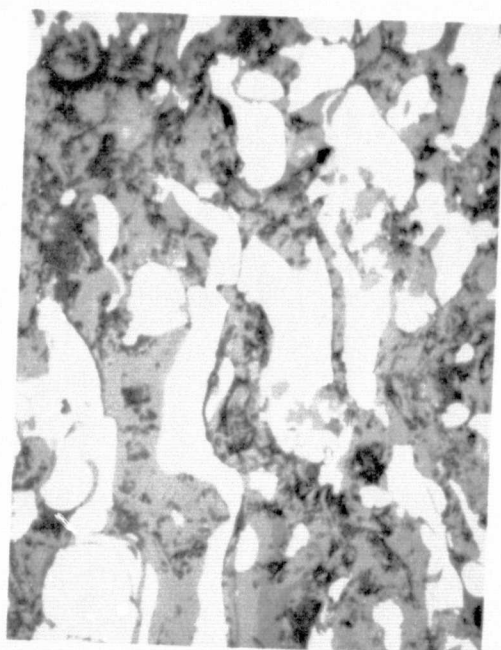
Figure 22 Thermal Fatigue Specimen (Test No. 5)



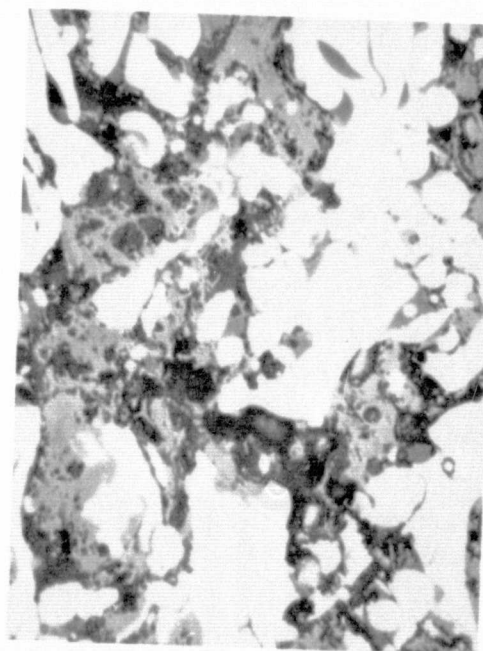
ZrO₂



85/15 YSZ/CoCrALY



70/30 YSZ/CoCrALY



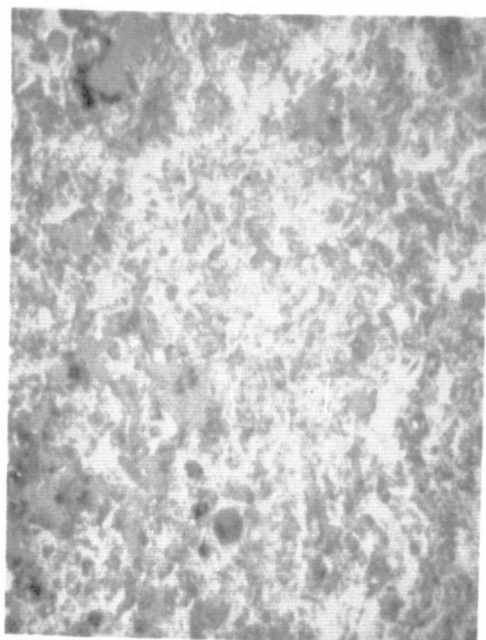
40/60 YSZ/CoCrALY

500X

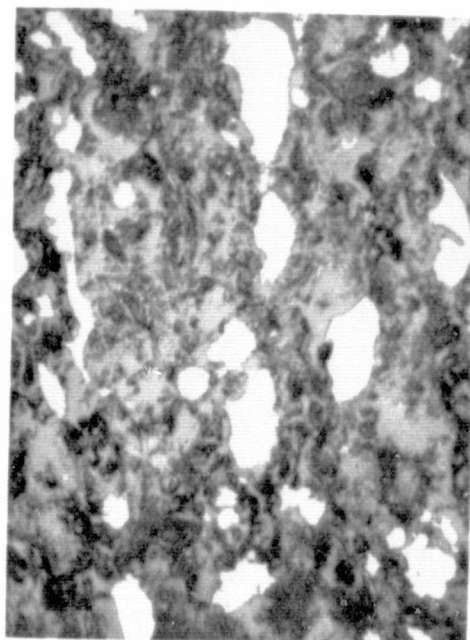
20% REDUCTION

Figure 23 Microstructure of NAS3-18565 Specimen

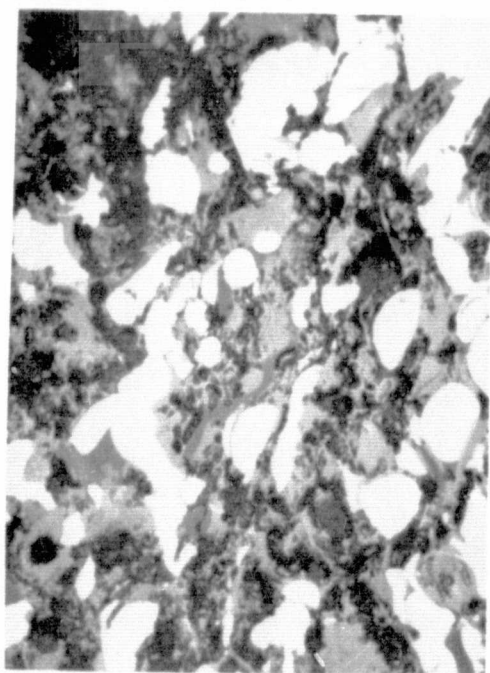
ORIGINAL PAGE IS
OF POOR QUALITY



ZrO_2



85/15 $\text{ZrO}_2/\text{CoCrAlY}$



70/30 $\text{ZrO}_2/\text{CoCrAlY}$



40/60 $\text{ZrO}_2/\text{CoCrAlY}$

500X

20% REDUCTION

Figure 24 Microstructure of NAS3-19759 Specimen

ORIGINAL PAGE IS
OF POOR QUALITY

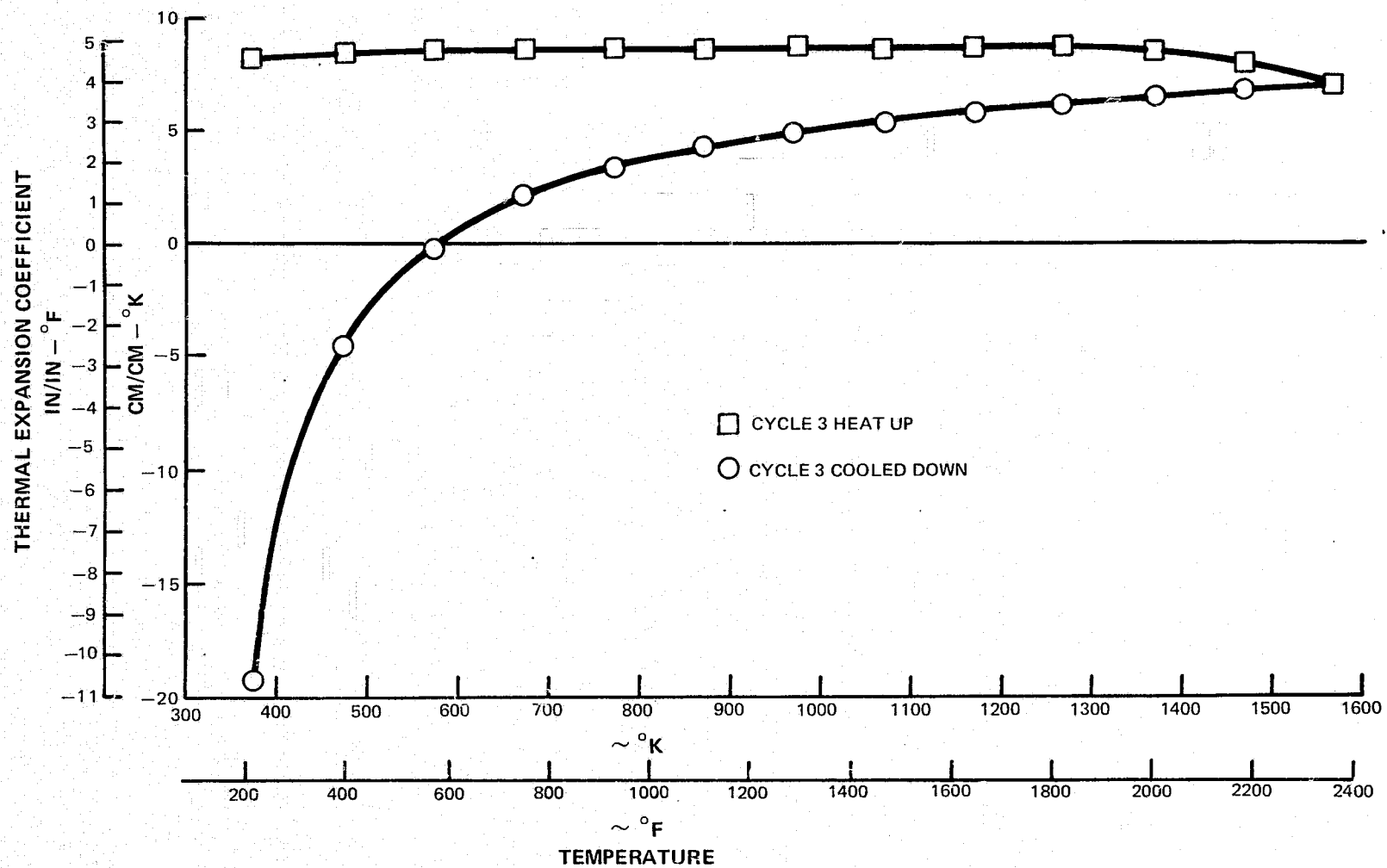


Figure 25 Sprayed ZrO_2 , Mean Coefficient of Thermal Expansion from $293^{\circ}K$ ($68^{\circ}F$)

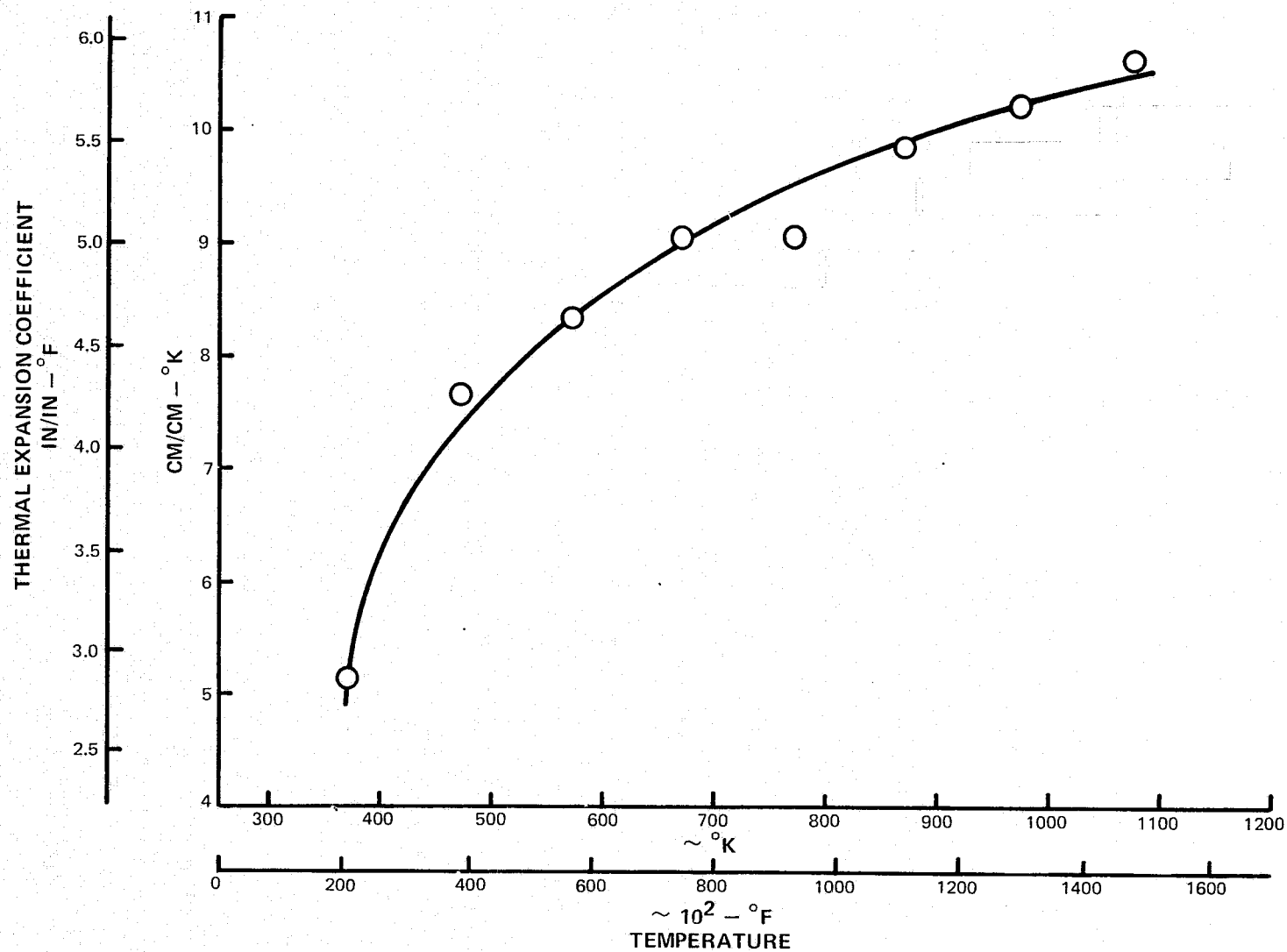


Figure 26 Sprayed 85/15 ZrO₂/CoCrAlY Mean Coefficient of Thermal Expansion from 293°K (68°F)

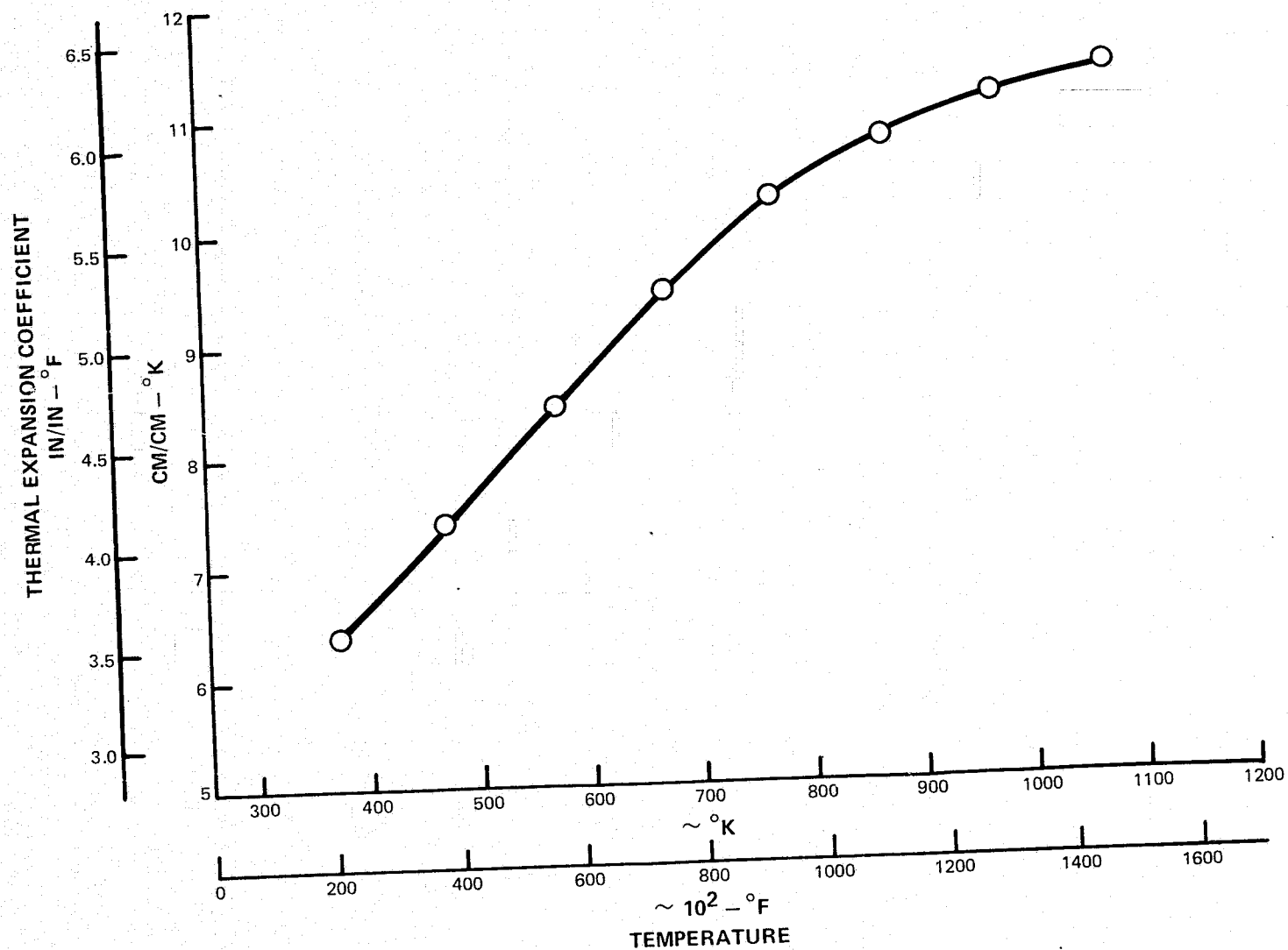


Figure 27 Sprayed 70/30 $ZrO_2/CoCrAlY$ Mean Coefficient of Thermal Expansion from 293°K (68° F)

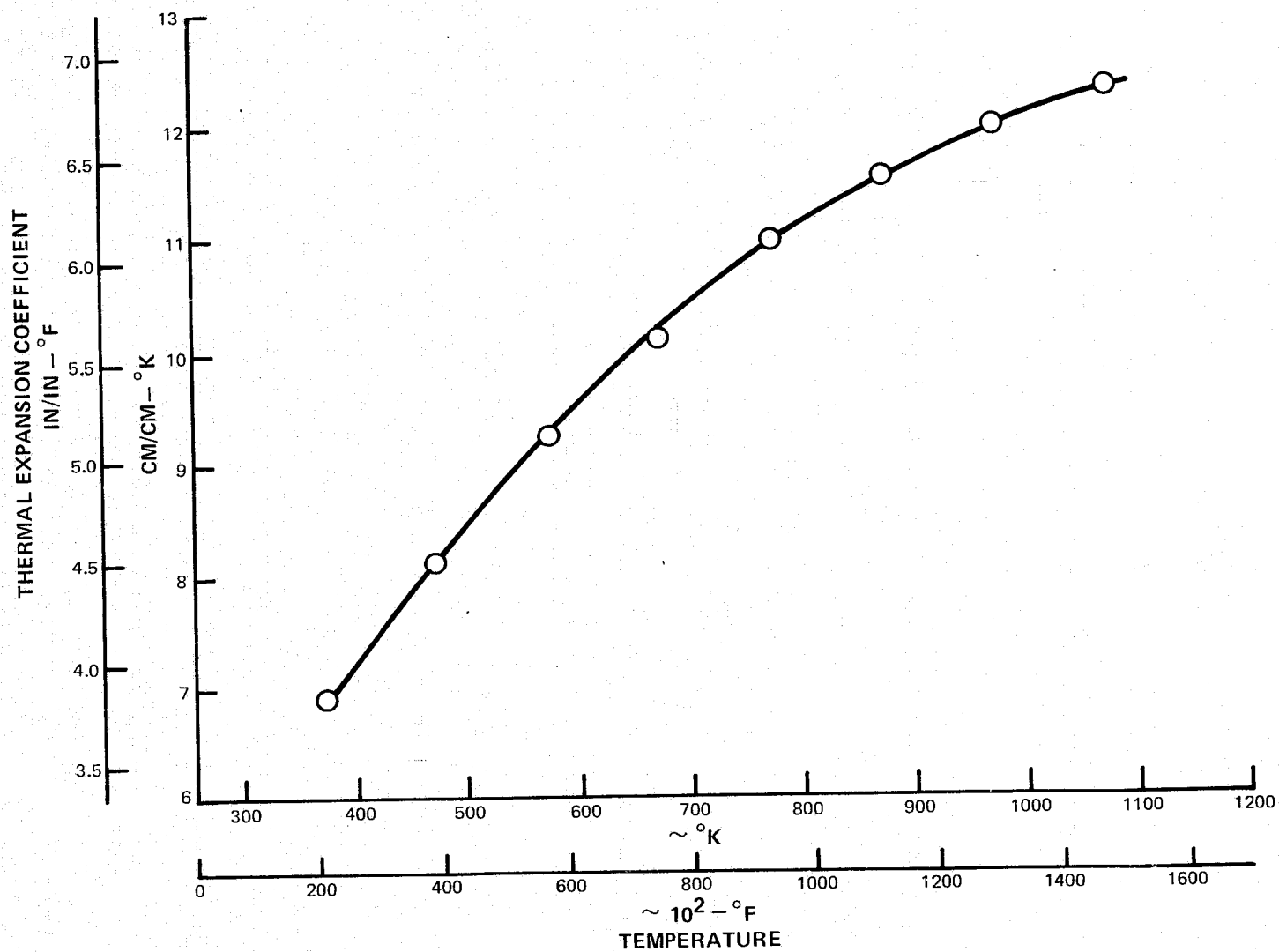


Figure 28 Sprayed 40/60 ZrO₂/CoCrAlY Mean Coefficient of Thermal Expansion from 293° K (68°F)

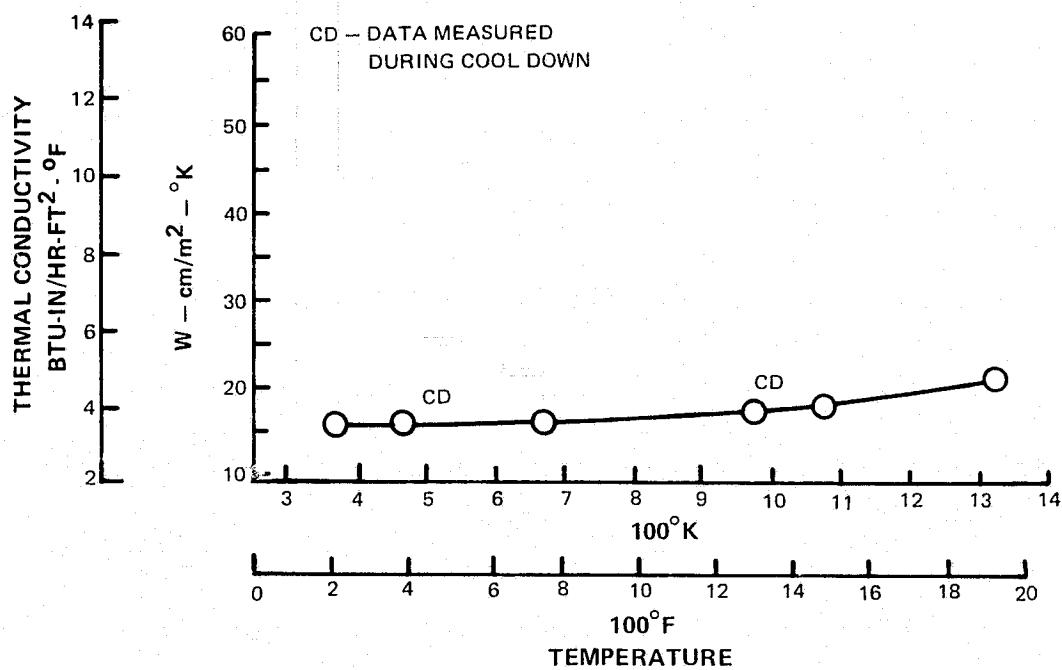


Figure 29 Thermal Conductivity of Sprayed ZrO_2 Layer

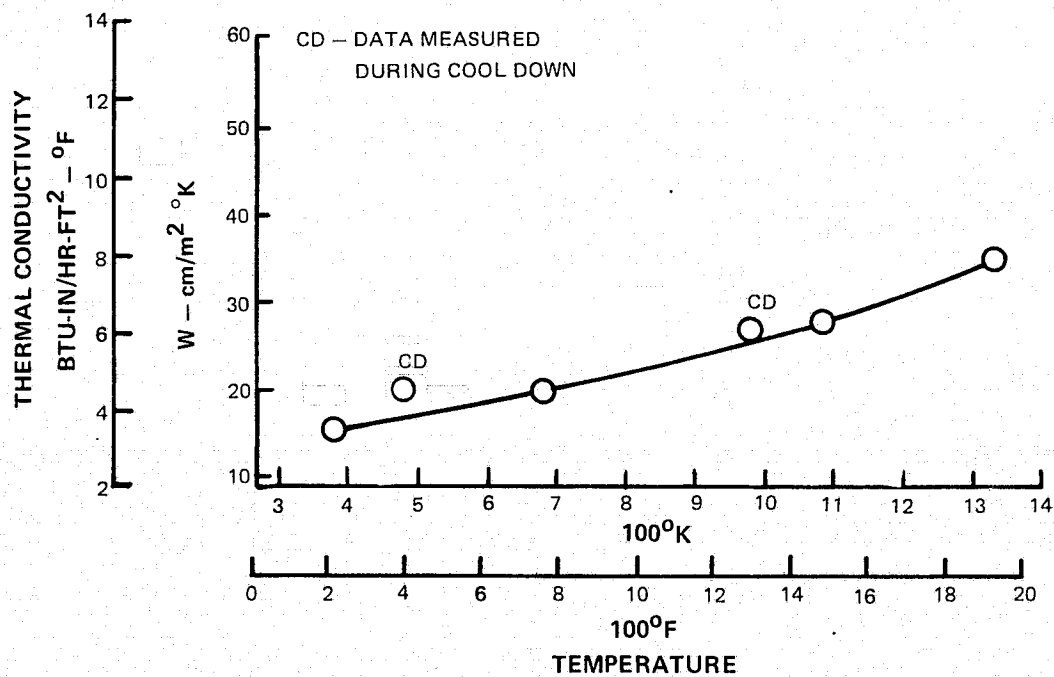


Figure 30 Thermal Conductivity of Composite Sprayed $ZrO_2/CoCrAlY$ Seal Coating

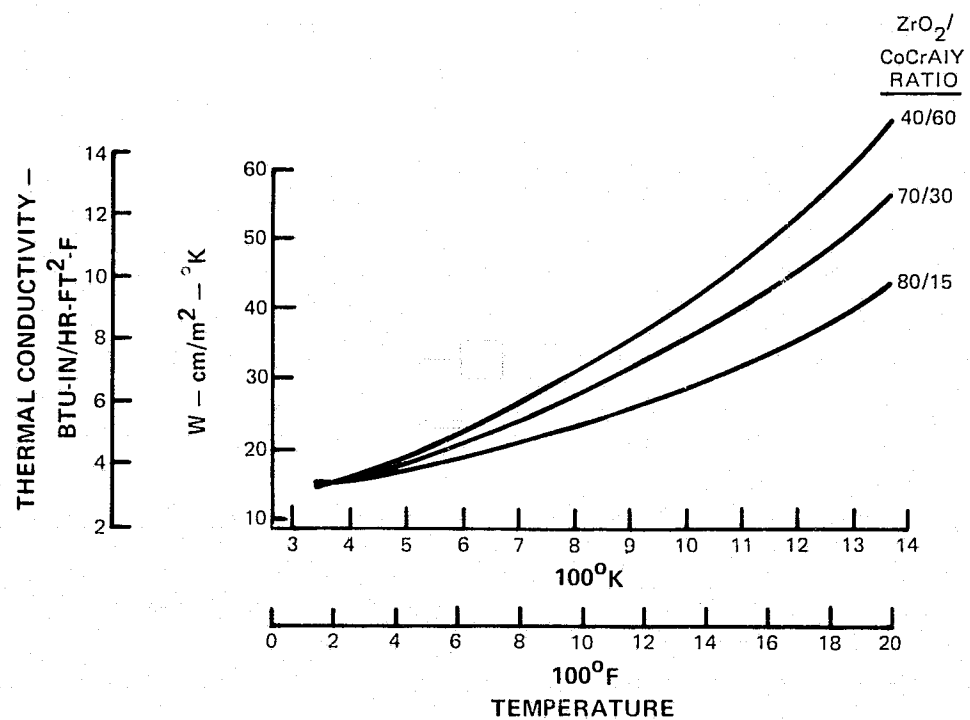


Figure 31 Estimated Thermal Conductivities for Mixed $ZrO_2/CoCrAlY$ Layers

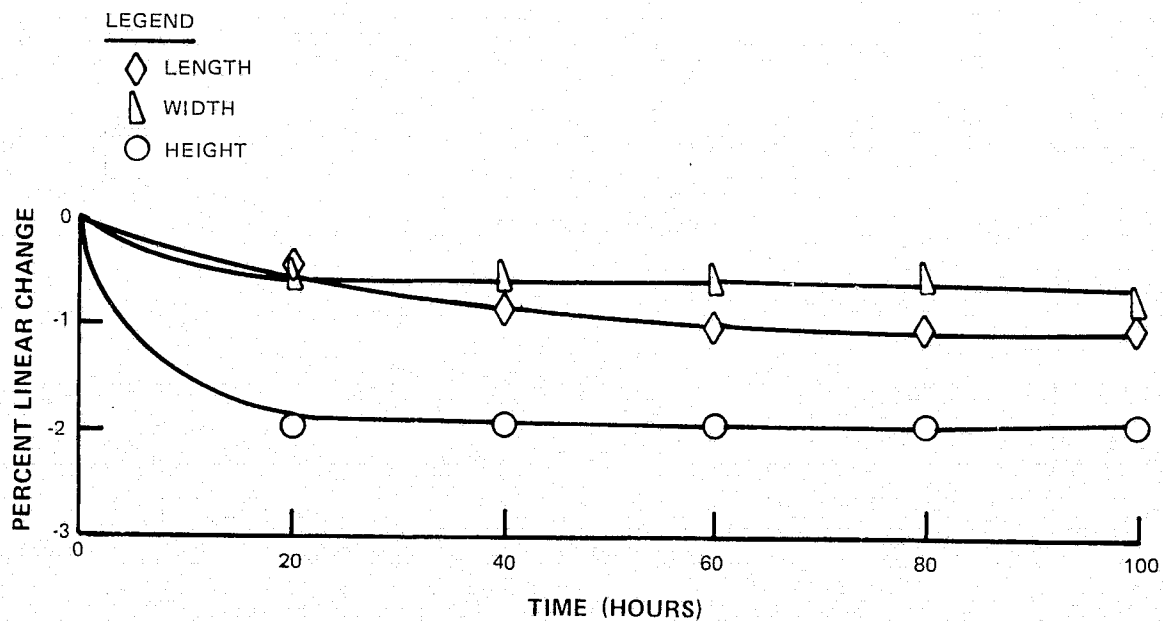


Figure 32 Linear Change Due to Thermal Exposure at $1589K$ ($2400F$), ZrO_2 Layer

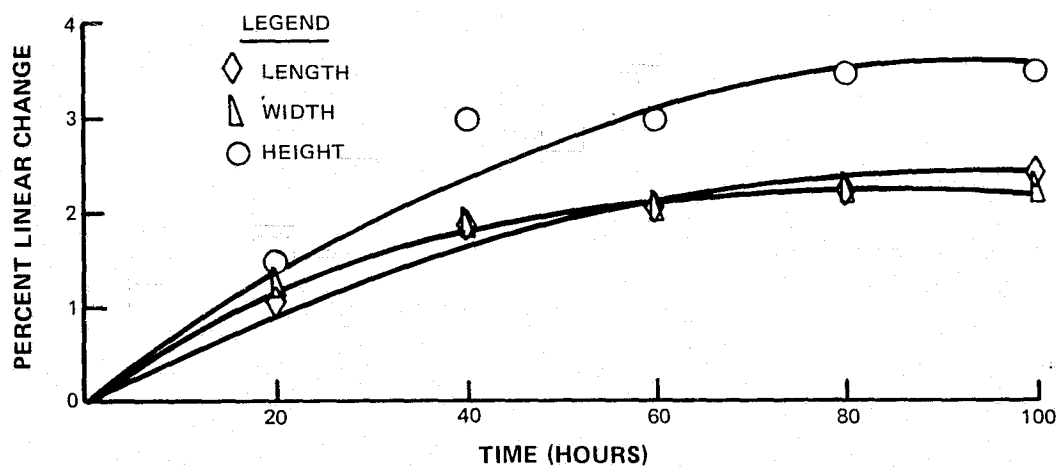


Figure 33 Linear Change Due to Thermal Exposure at 1144K (1600F), 85/15 ZrO₂/CoCrAlY Layer

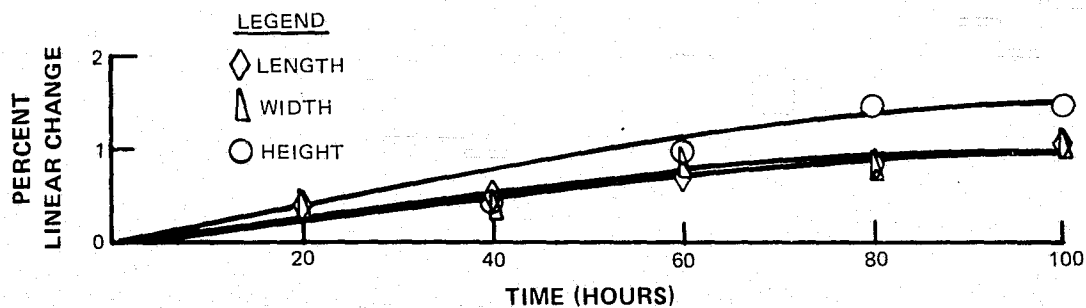


Figure 34 Linear Change Due to Thermal Exposure at 1061K (1450F), 70/30 ZrO₂/CoCrAlY Layer

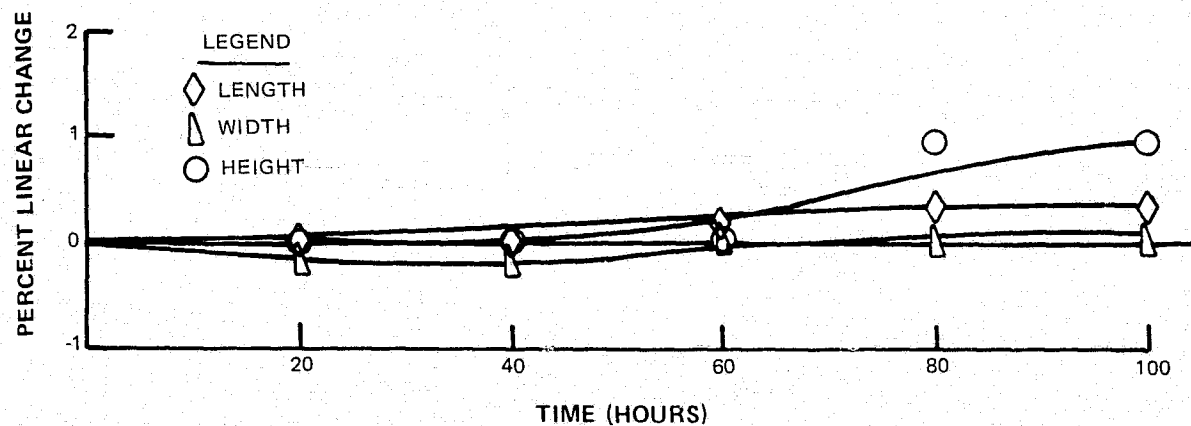


Figure 35 Linear Change Due to Thermal Exposure at 1005K (1350F), 40/60 ZrO₂/CoCrAlY Layer

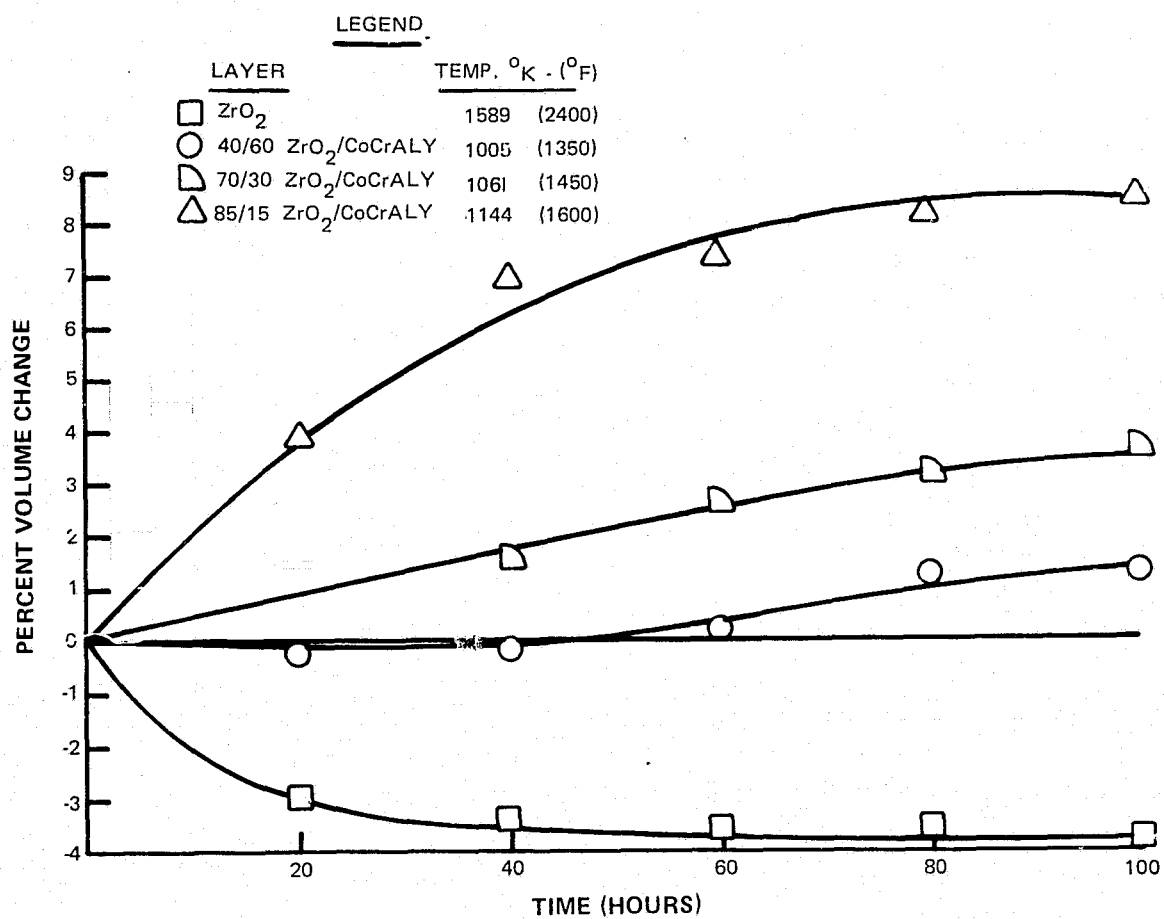


Figure 36 Volume Change Due to Thermal Exposure

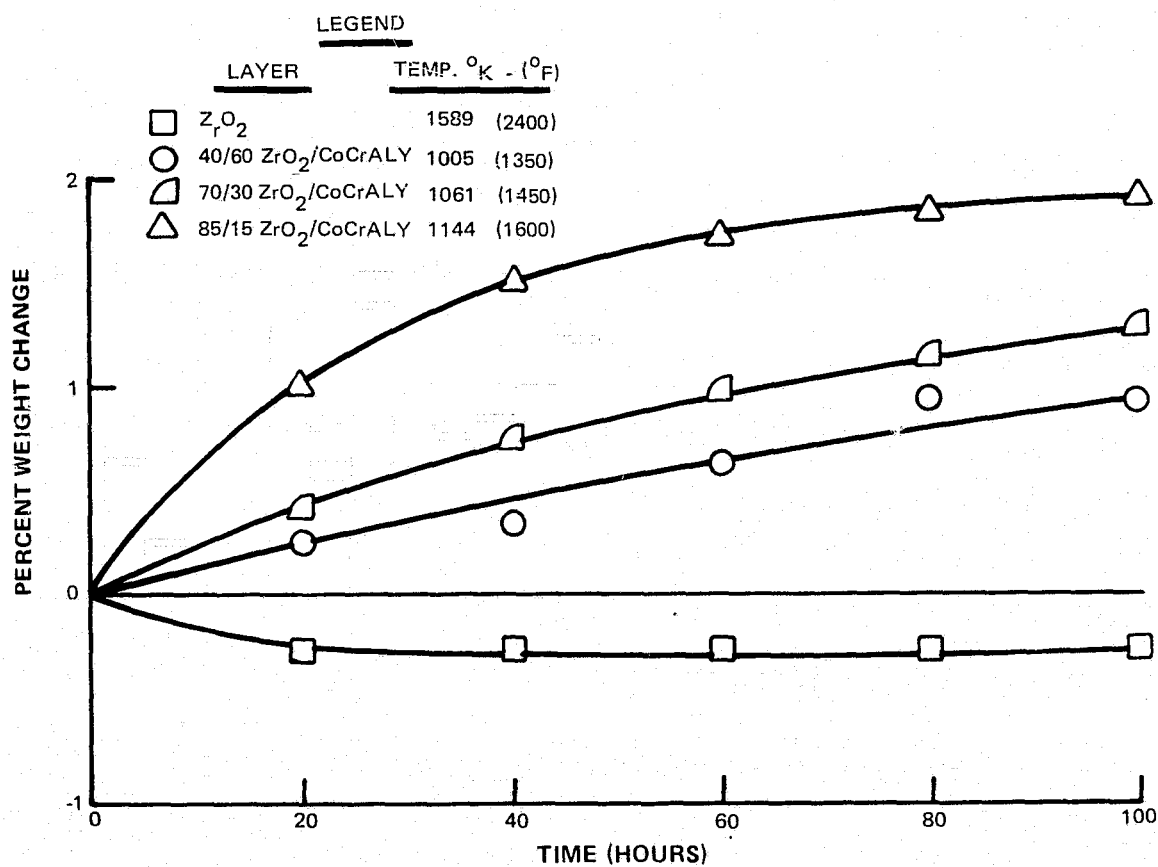


Figure 37 Weight Change Due to Thermal Exposure

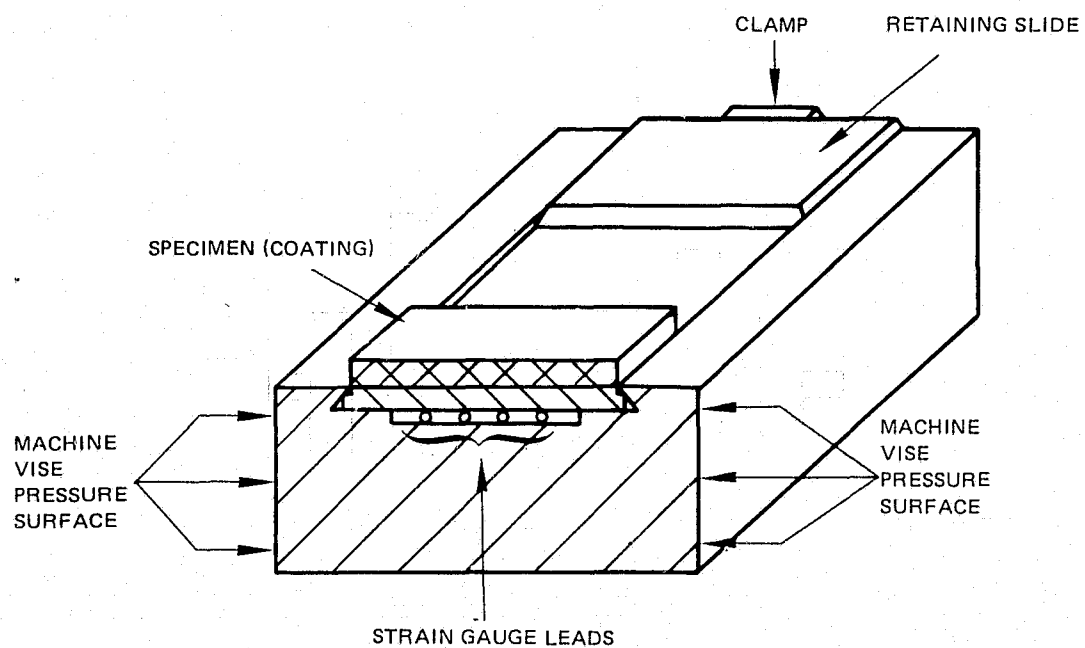


Figure 38 Residual Stress Machining Fixture

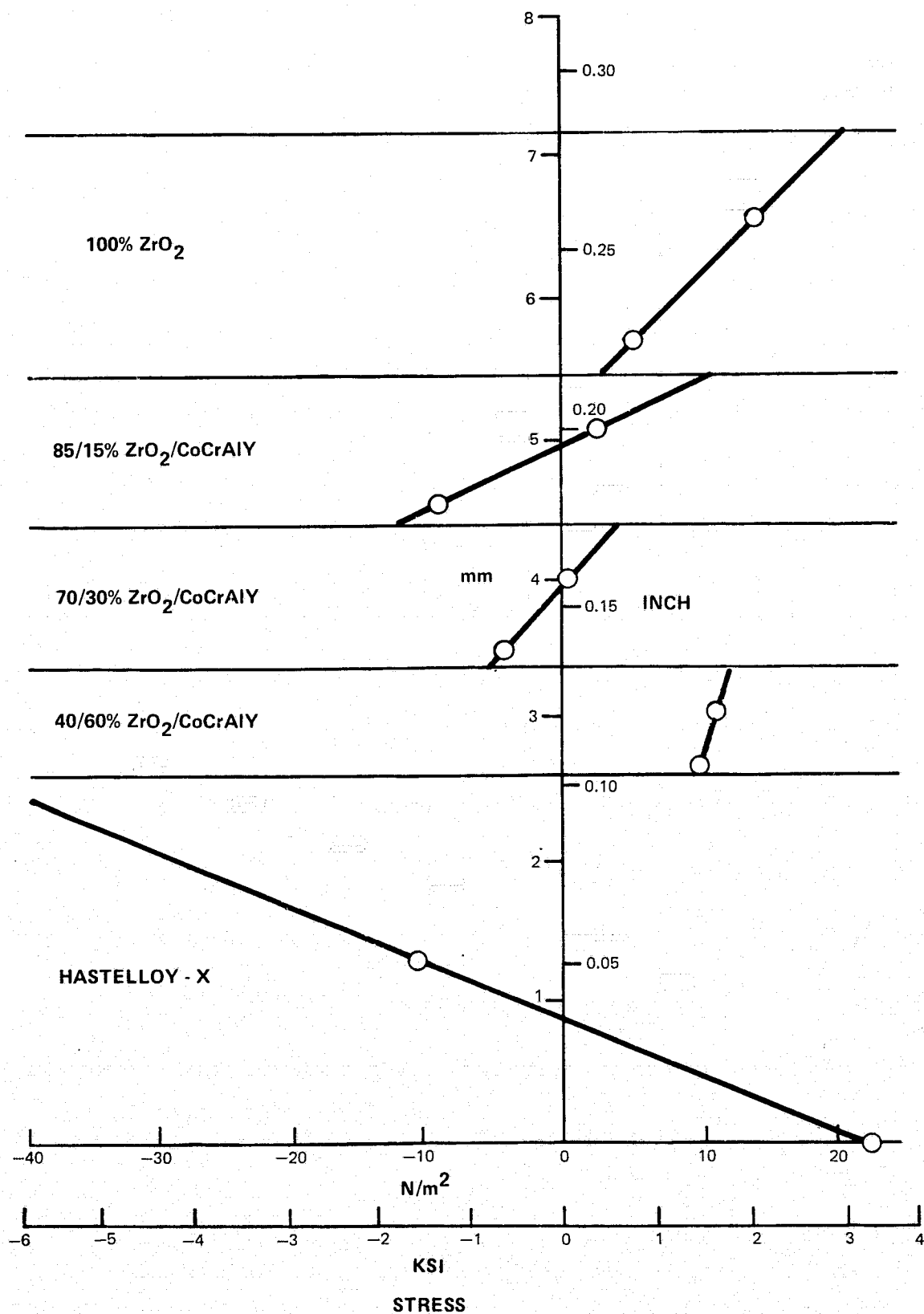


Figure 39 Residual Stress Distribution in Plasma Sprayed ZrO₂/CoCrAlY Erosion Specimen

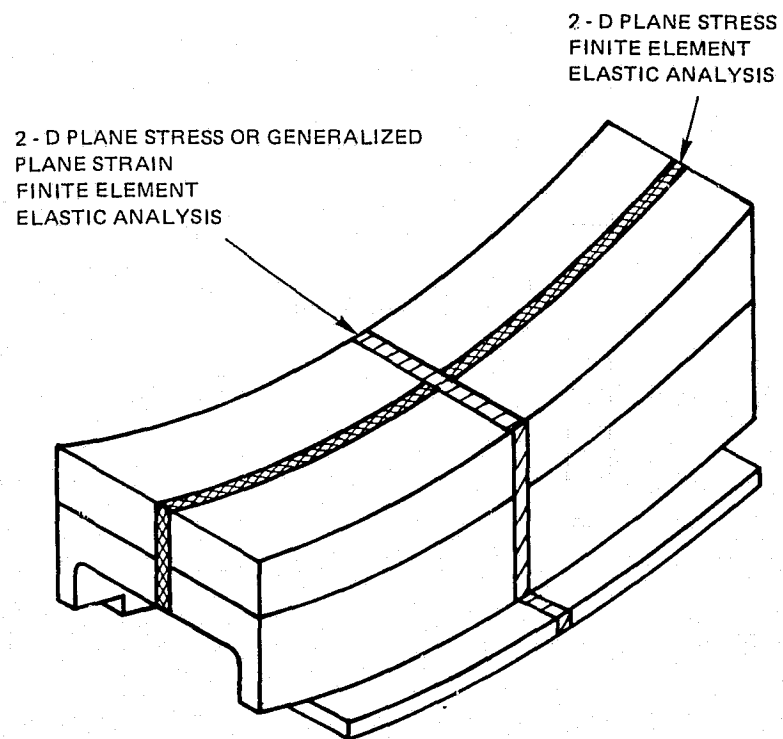


Figure 40 Analytical Approach

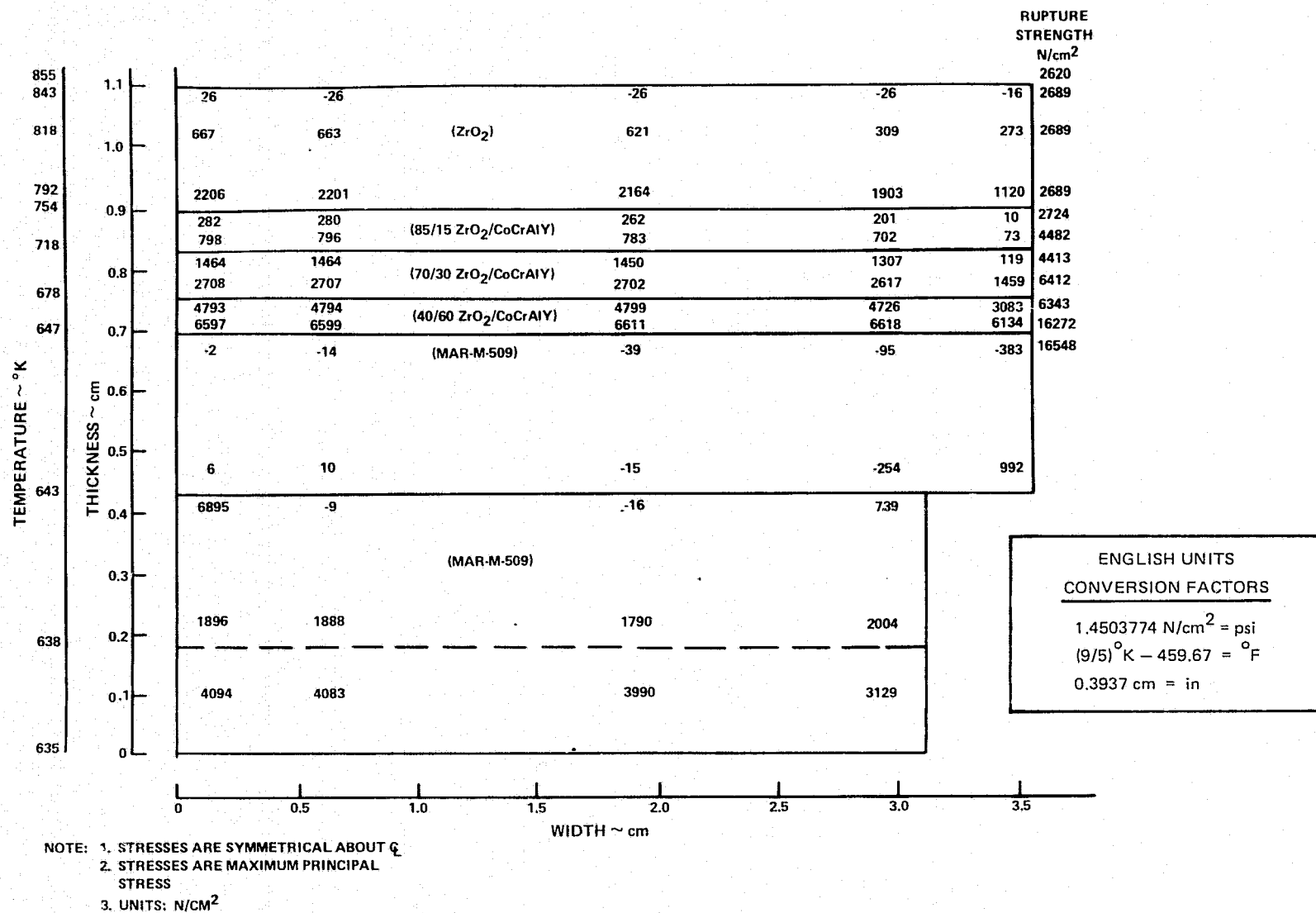
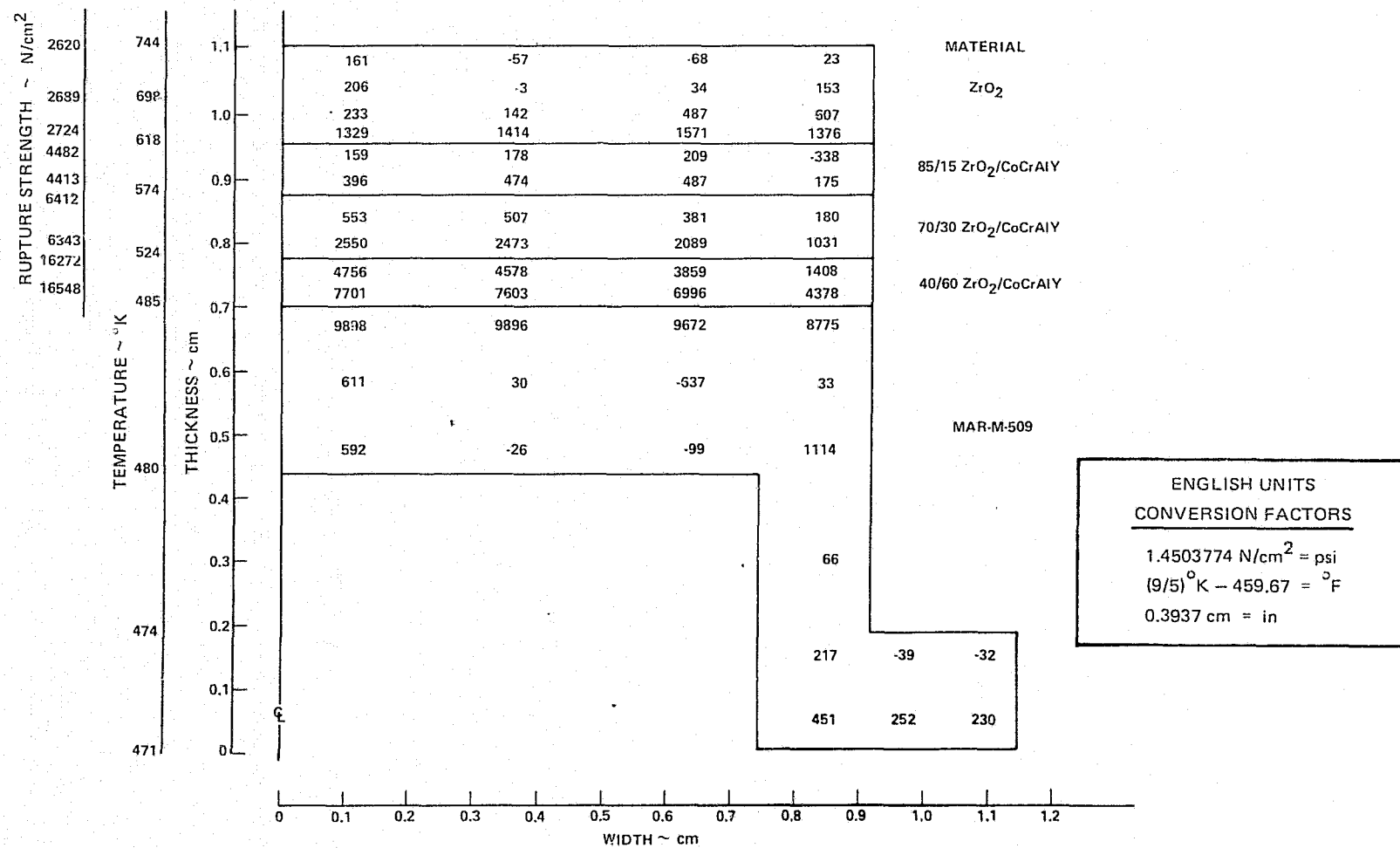
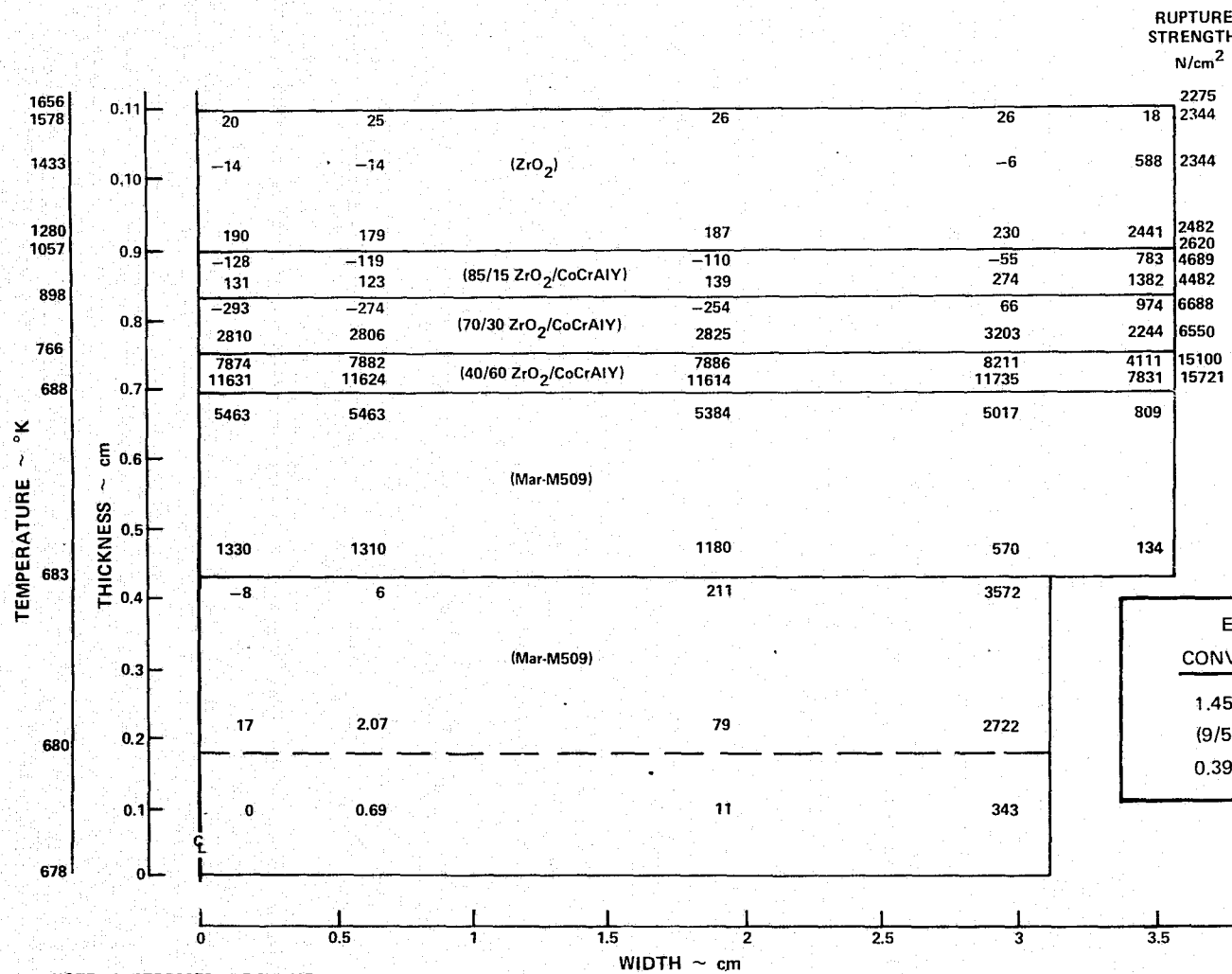


Figure 41 Thermal Fatigue Test Specimen Maximum Principal Circumferential Stresses at Idle



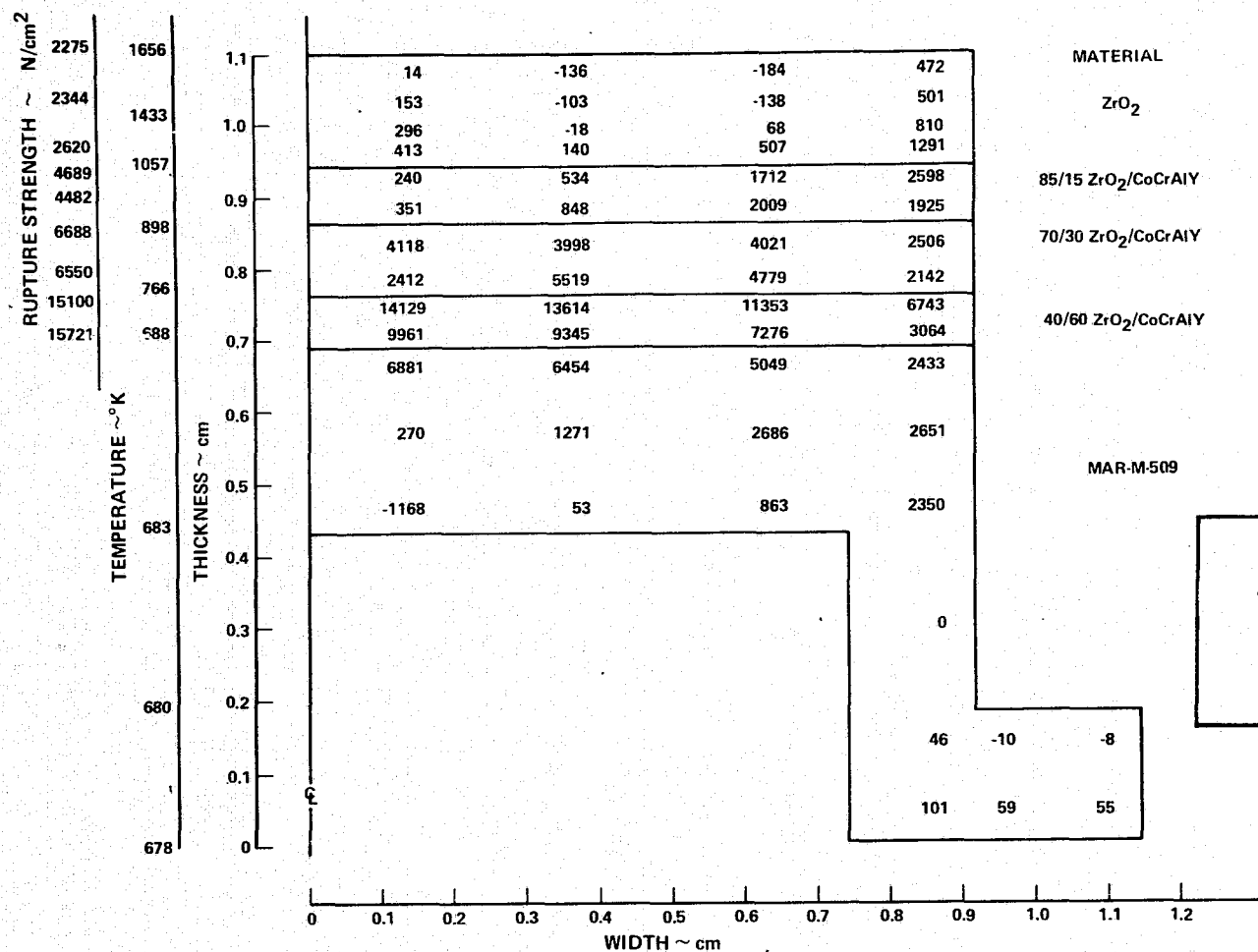
NOTE: 1. STRESSES ARE SYMMETRICAL ABOUT CL
2. NEGATIVE VALUES INDICATE COMPRESSIVE STRESSES
3. UNITS: N/CM²

Figure 42 Thermal Fatigue Test Specimen Maximum Principal Axial Stresses at Idle



NOTE: 1. STRESSES ARE SYMMETRICAL ABOUT \bar{C}
 2. STRESSES ARE MAXIMUM PRINCIPAL STRESS
 3. UNITS: N/CM²

Figure 43 Thermal Fatigue Test Specimen Maximum Principal Circumferential Stresses at 20.5 Sec. Accel.



NOTE: 1. STRESSES ARE SYMMETRICAL ABOUT Q
 2. NEGATIVE VALUES INDICATE COMPRESSIVE STRESSES
 3. UNITS: N/CM²

Figure 44 Thermal Fatigue Test Specimen Maximum Principal Axial Stresses at 20.5 Sec. Accel.

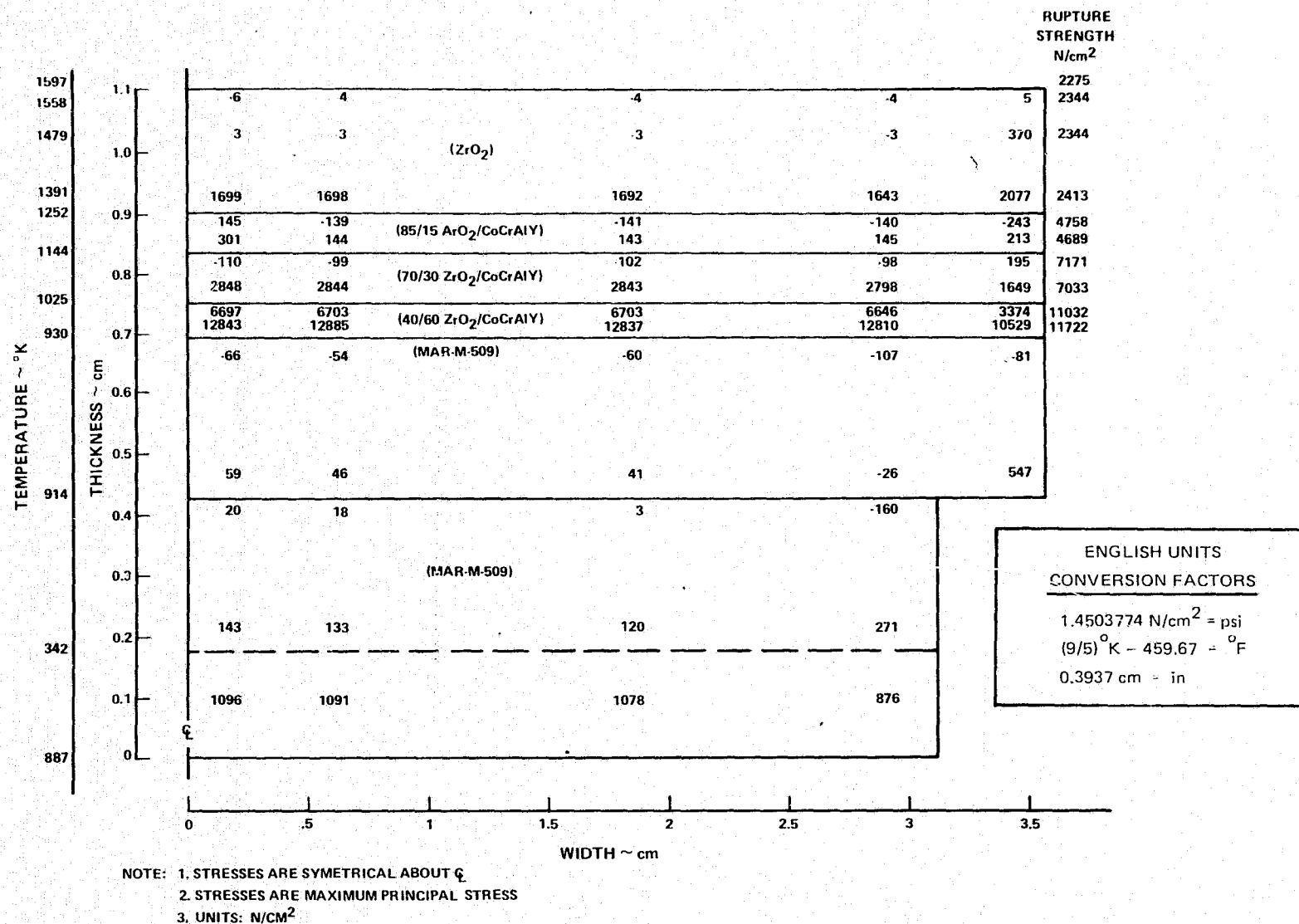
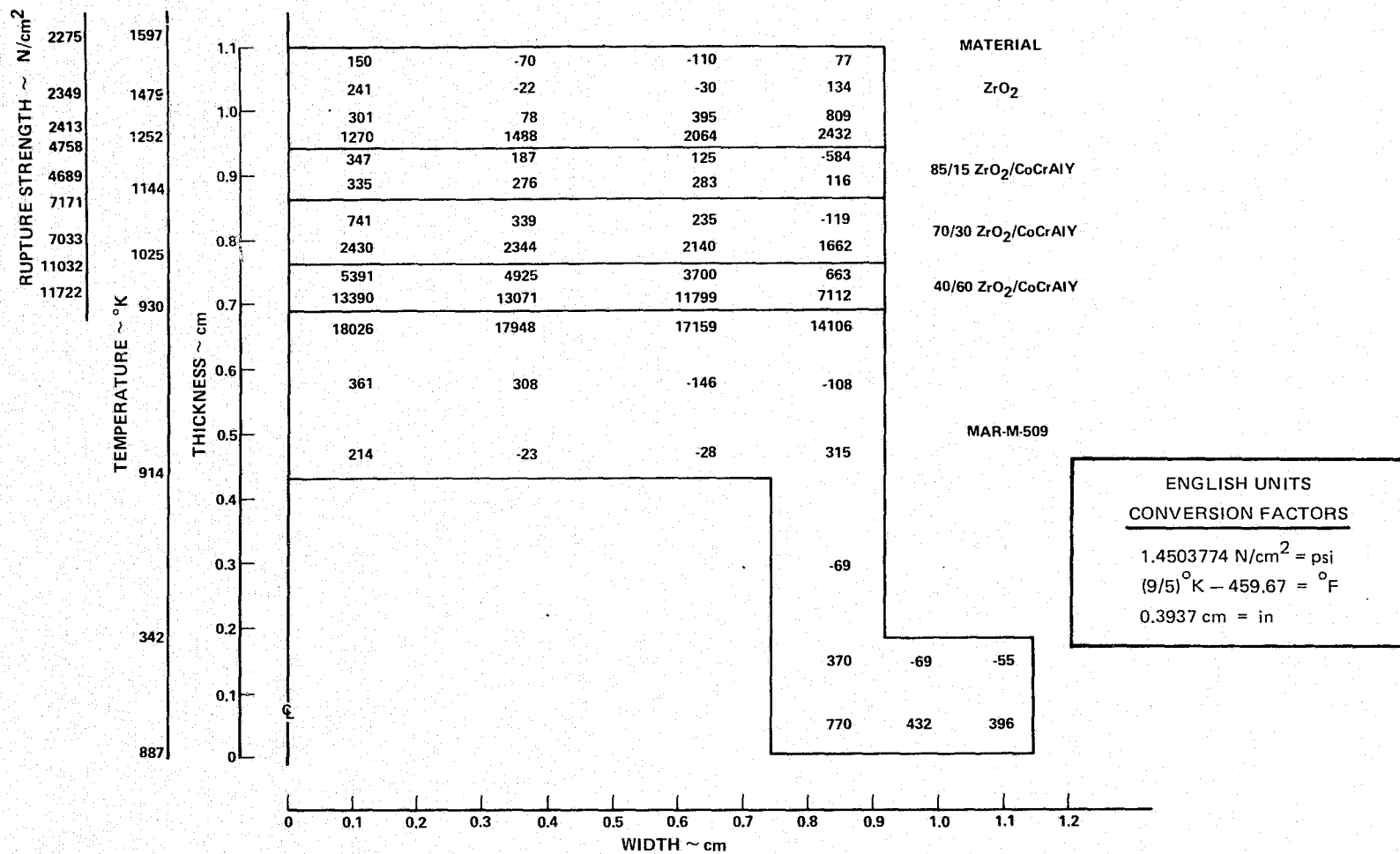
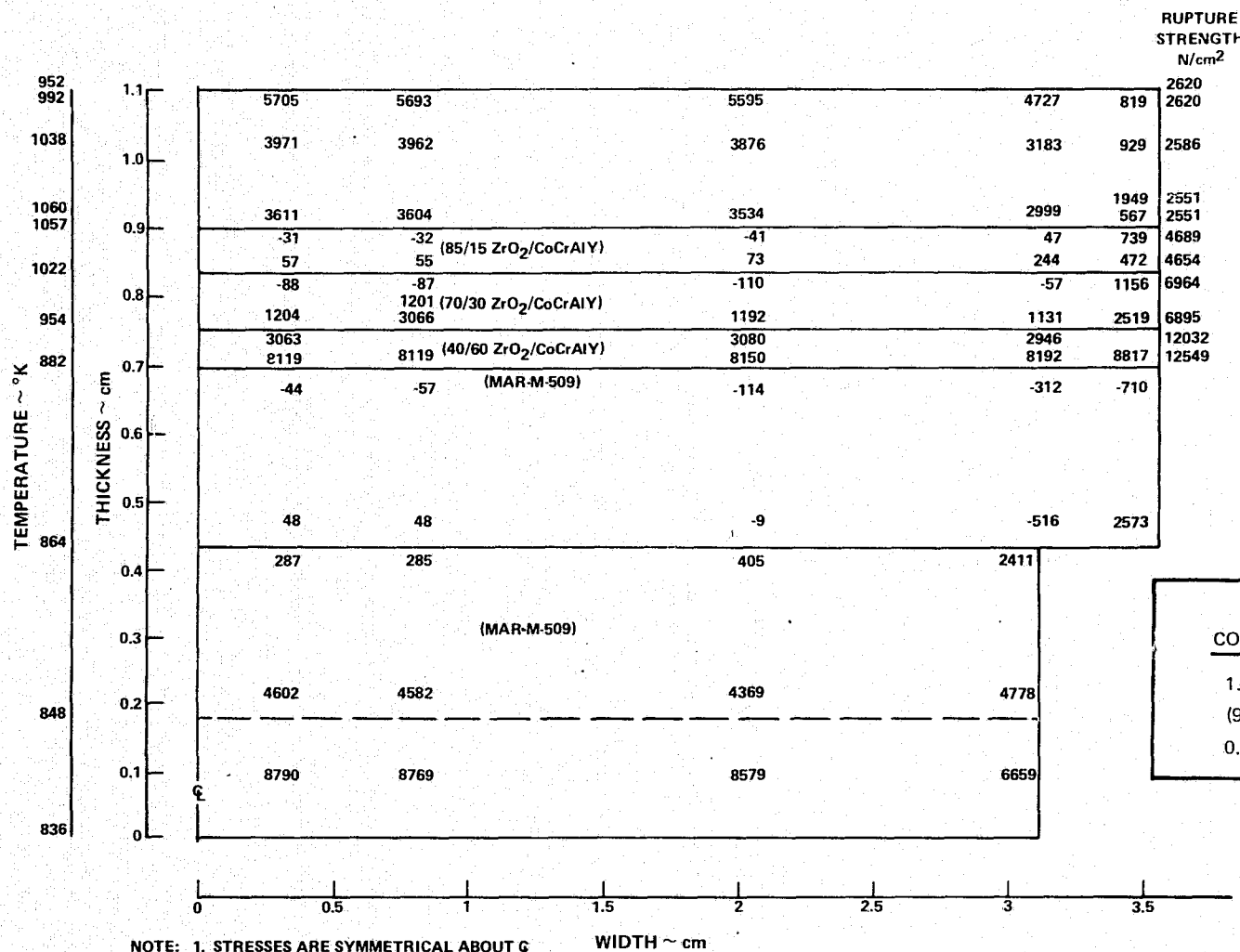


Figure 45 Thermal Fatigue Test Specimen Maximum Principal Circumferential Stresses at SLTO



- NOTE: 1. STRESSES ARE SYMMETRICAL ABOUT Q
 2. NEGATIVE VALUES INDICATE COMPRESSIVE STRESSES
 3. UNITS: N/CM²

Figure 46 Thermal Fatigue Test Specimen Maximum Principal Axial Stresses at SLTO



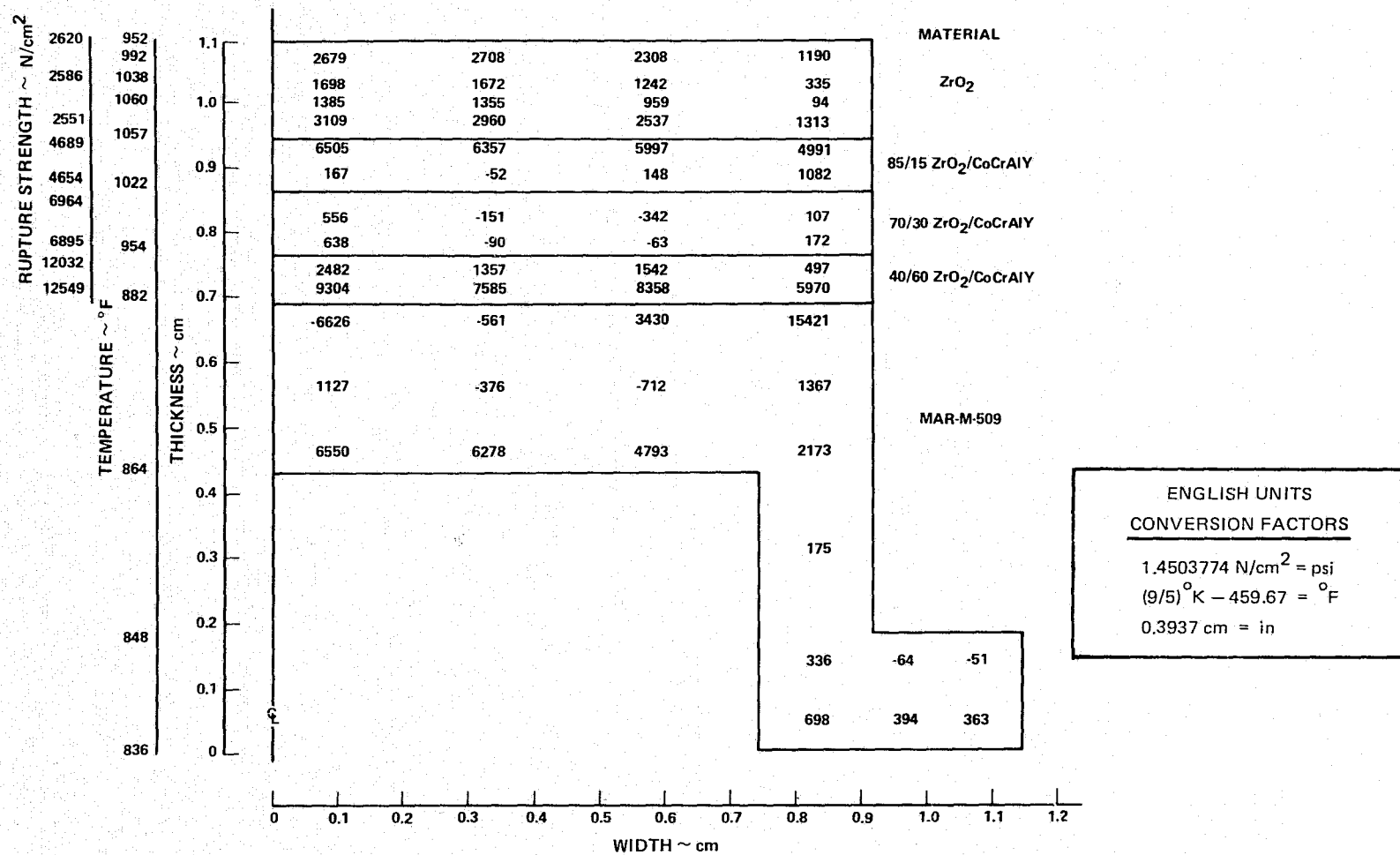
ENGLISH UNITS
CONVERSION FACTORS

$$1.4503774 \text{ N/cm}^2 = \text{psi}$$

$$(9/5) ^\circ\text{K} - 459.67 = ^\circ\text{F}$$

$$0.3937 \text{ cm} = \text{in}$$

Figure 47 Thermal Fatigue Test Specimen Maximum Principal Circumferential Stresses at 17.5 Sec. Decel.



NOTE: 1. STRESSES ARE SYMMETRICAL ABOUT \bar{Q}
 2. NEGATIVE VALUES INDICATE COMPRESSIVE STRESSES
 3. UNITS: N/CM²

Figure 48 Thermal Fatigue Test Specimen Maximum Principal Axial Stresses at 17.5 Sec. Decel.

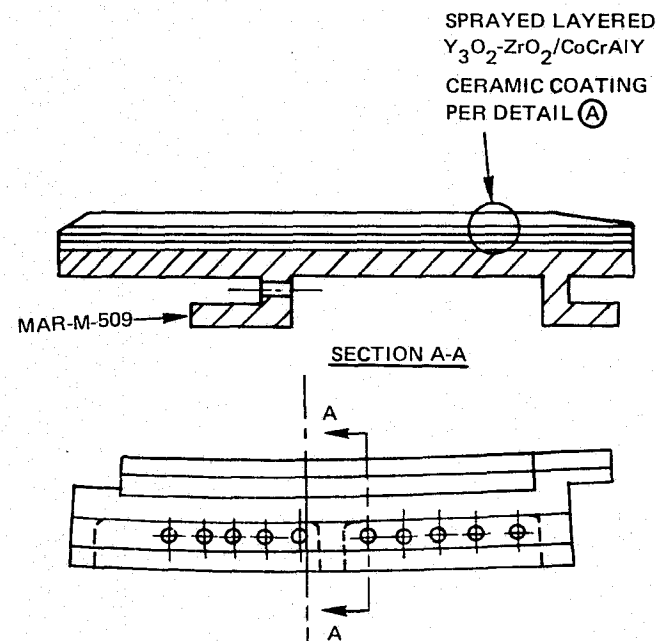
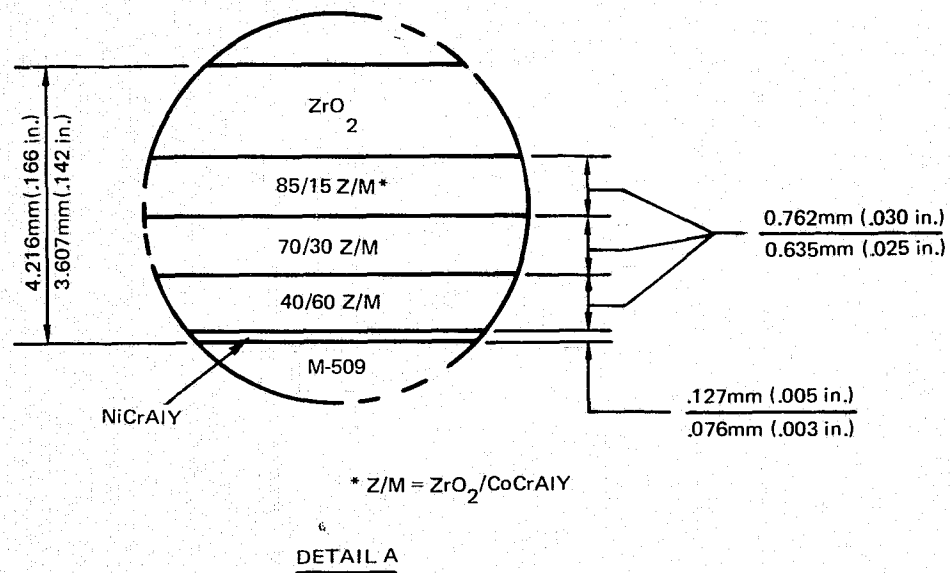


Figure 49 Typical Engine Seal Segment

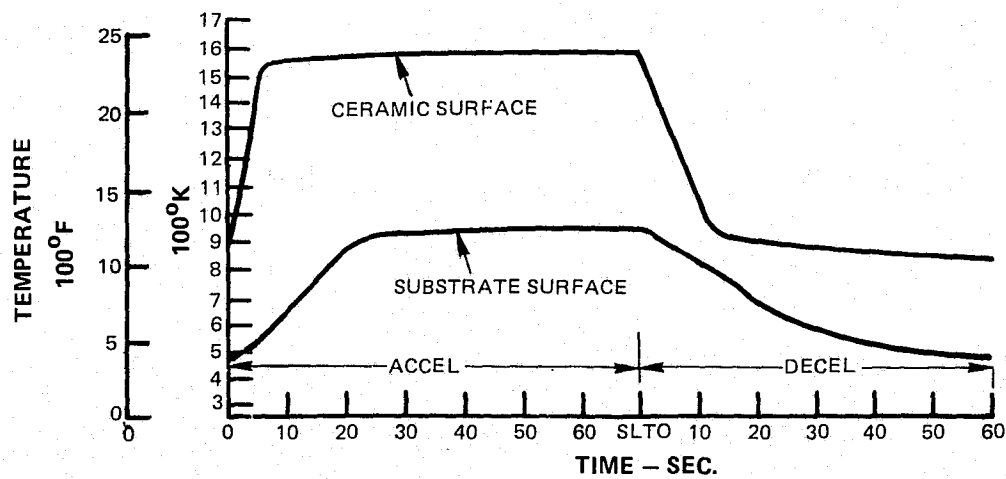
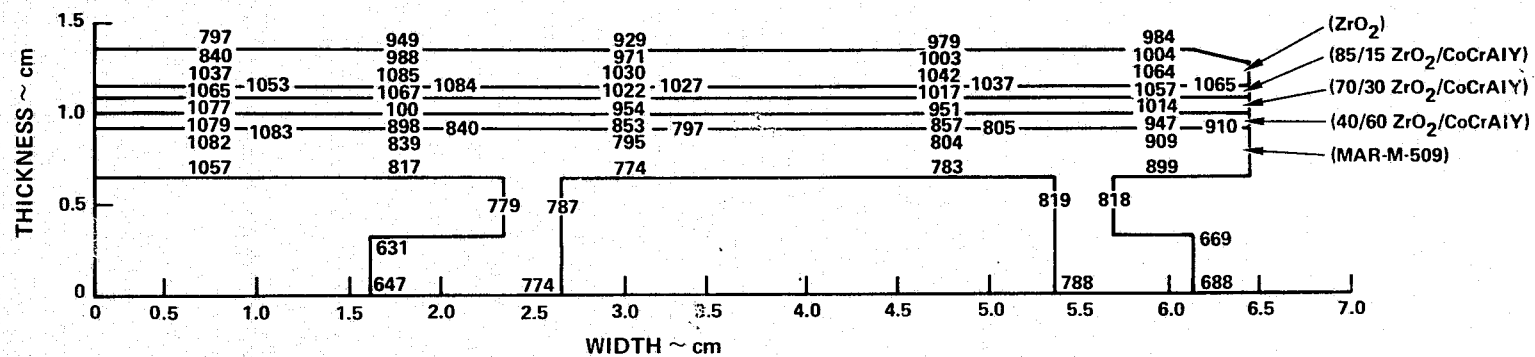


Figure 50 Engine Seal Segment Calculated Temperature Cycle at Hottest Location



ENGLISH UNITS
CONVERSION FACTORS

$$(9/5) ^\circ\text{K} - 459.67 = ^\circ\text{F}$$

$$0.3937 \text{ cm} = \text{in}$$

Figure 51 Engine Seal Segment Temperature Distribution at 12 Sec. Decel.

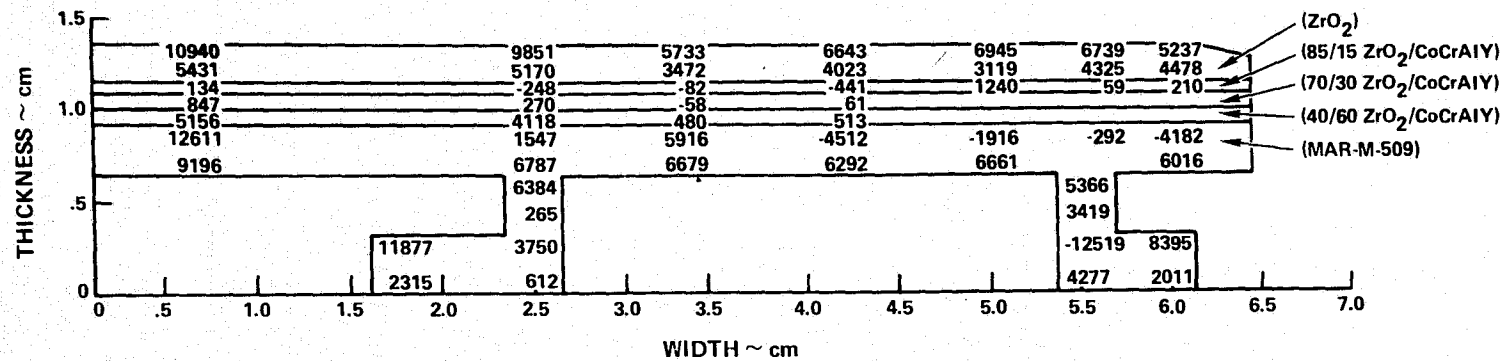
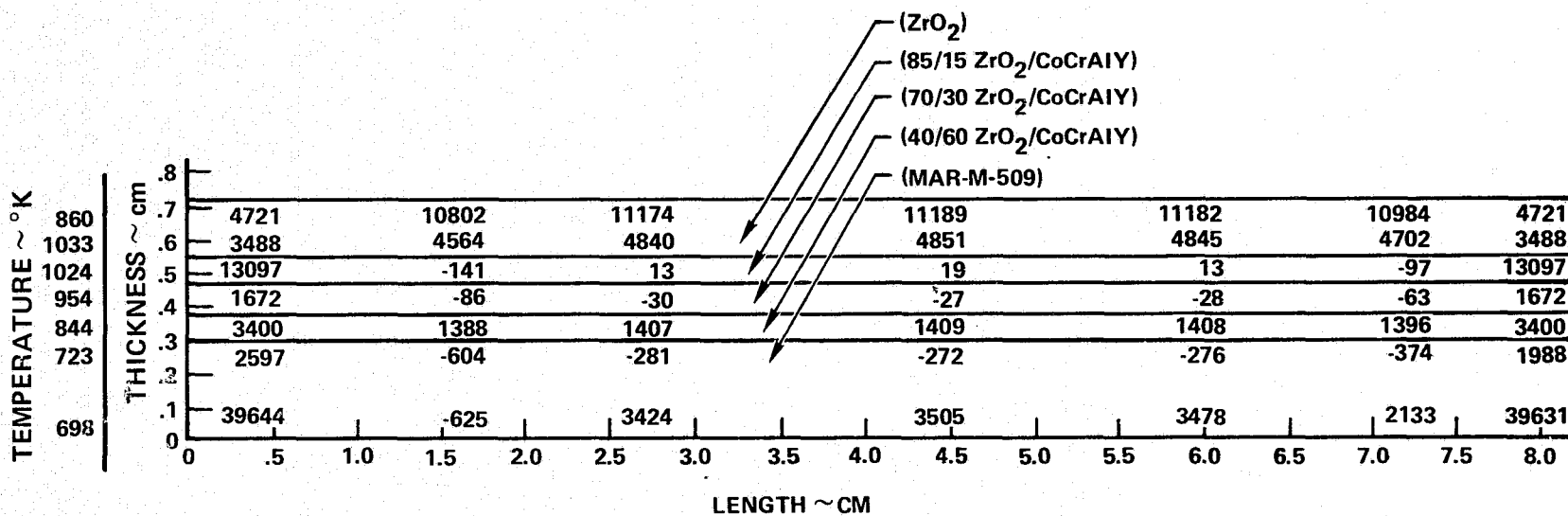


Figure 52 Engine Seal Segment Maximum Principal Axial Stress Distribution at 12 Sec. Decel.



NOTE: 1. NEGATIVE NUMBERS INDICATE
COMPRESSIVE STRESSES
2. UNITS: N/CM²

ENGLISH UNITS
CONVERSION FACTORS

1.4503774 N/cm² = psi
(9/5) °K - 459.67 = °F
0.3937 cm = in

Figure 53 Engine Seal Segment Maximum Principal Circumferential Stress
Distribution at 12 Sec. Decel.

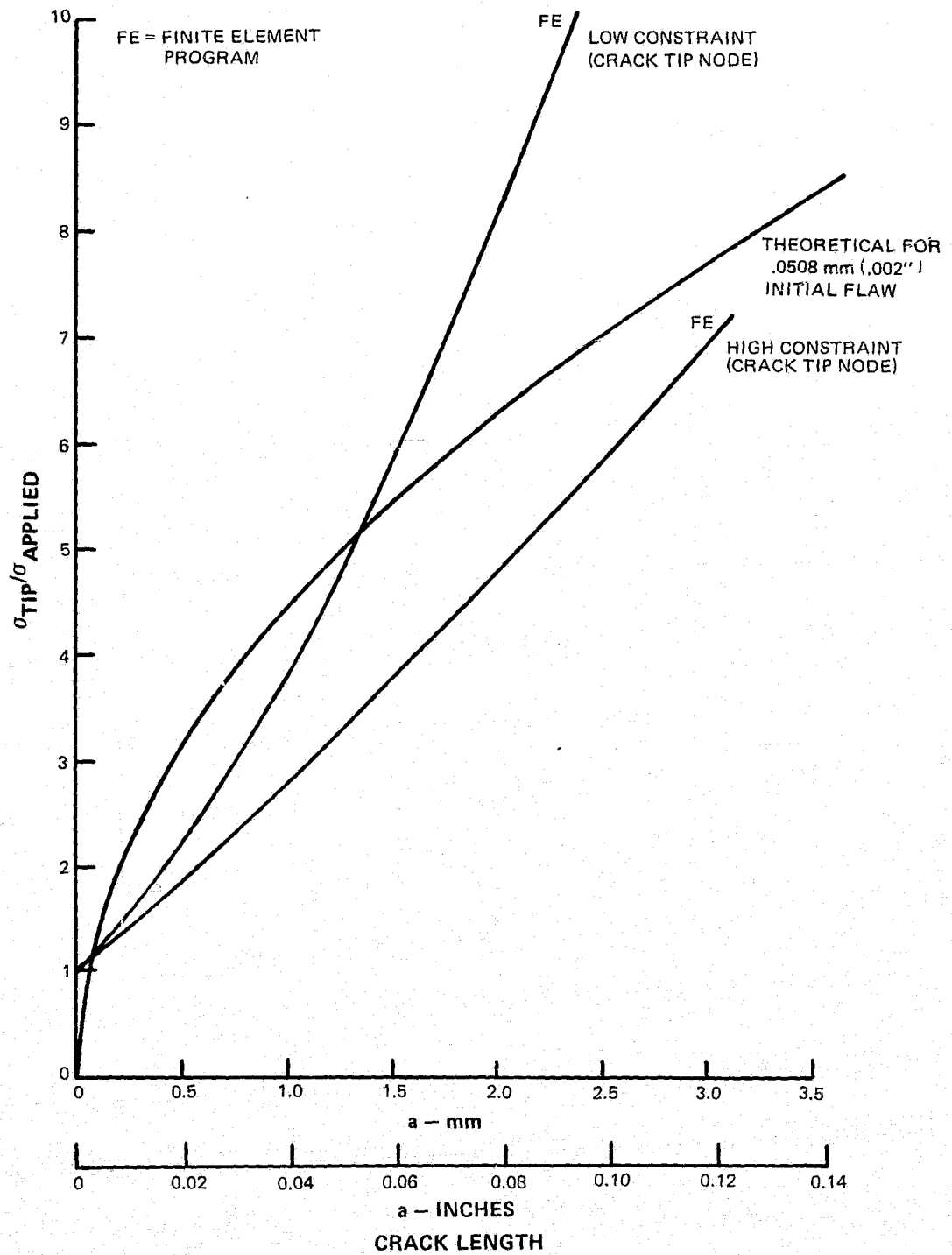
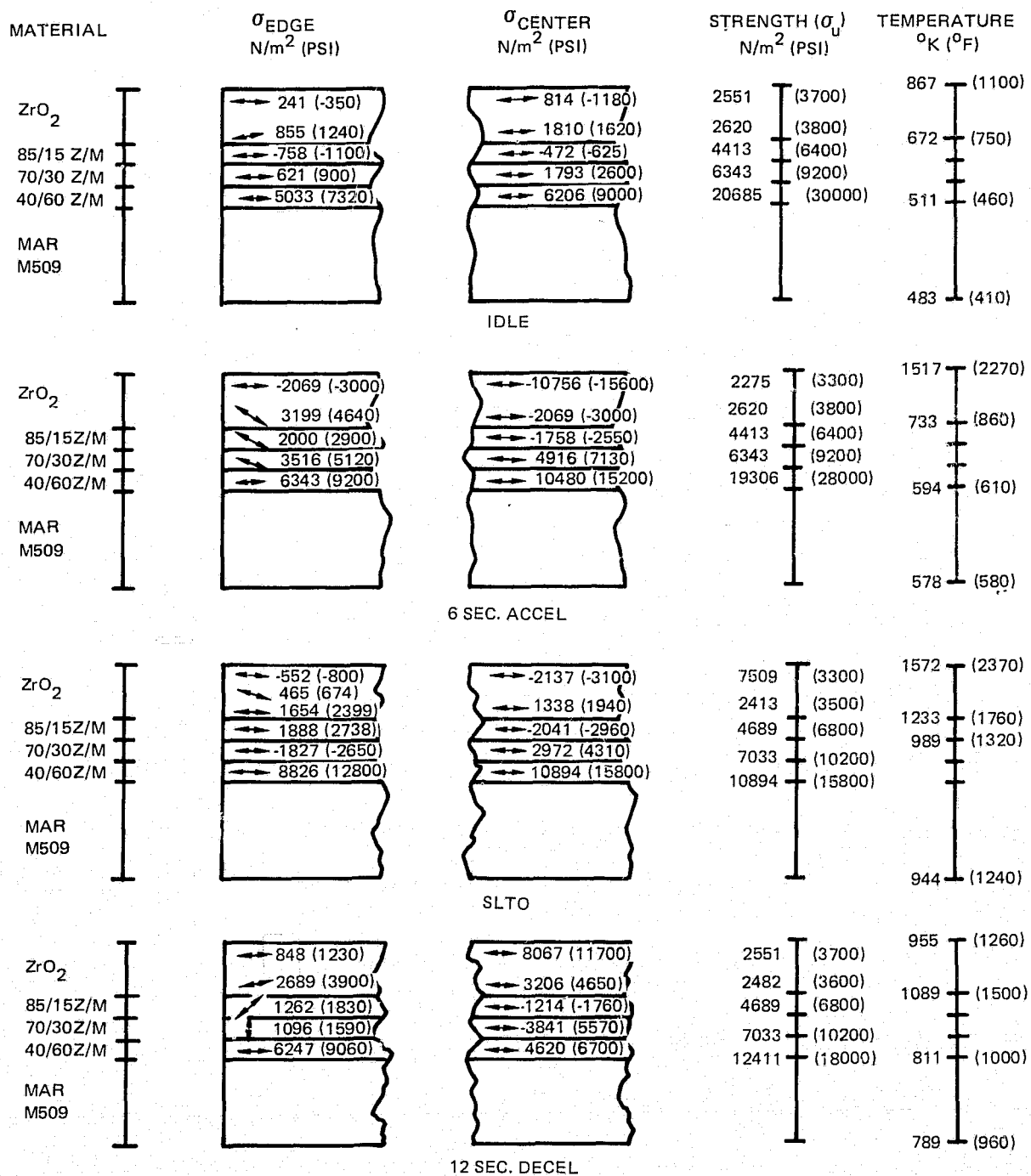
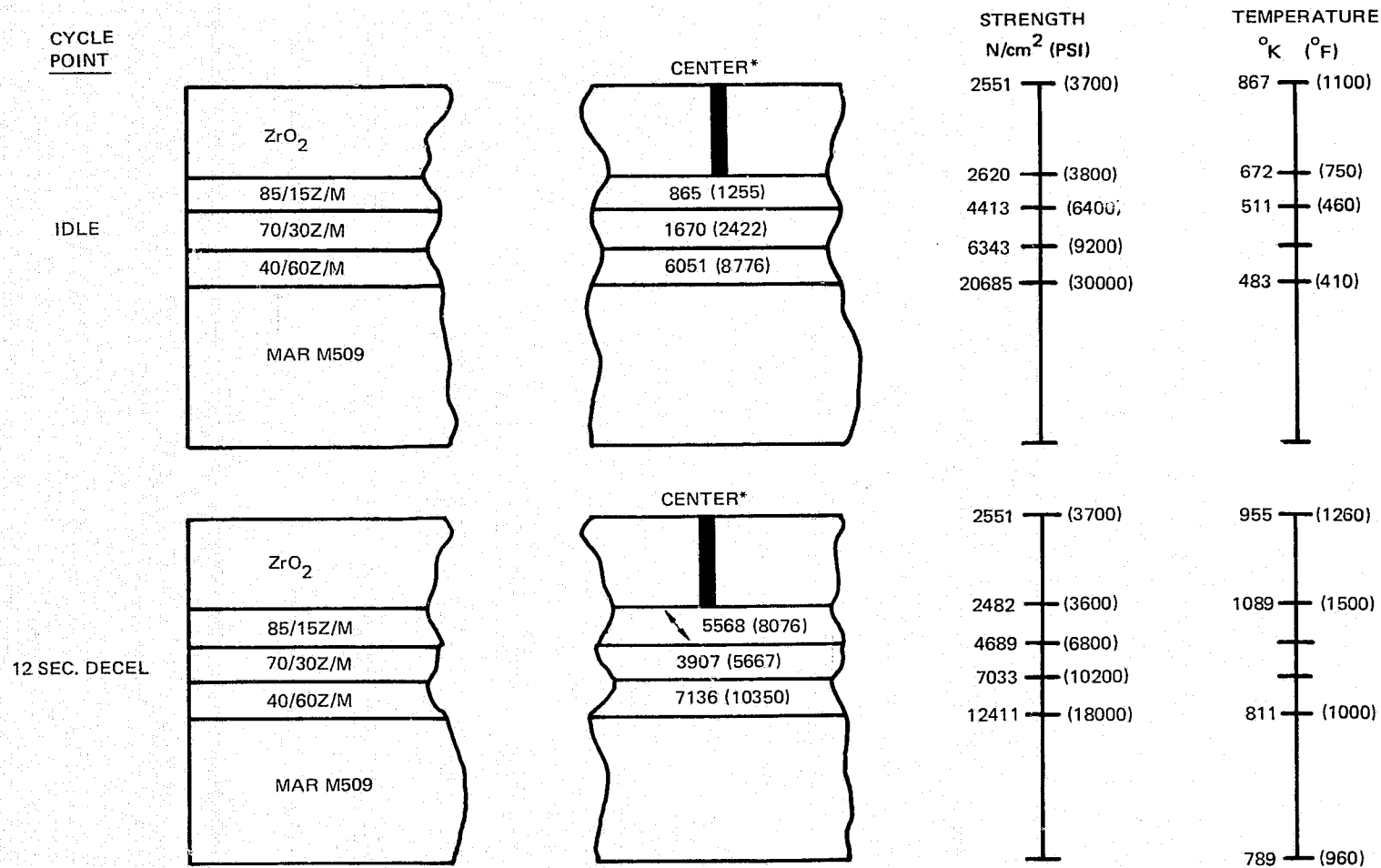


Figure 54 Crack Tip to Applied Stress Ratio vs. Crack Length



- NOTE: 1. AT SEVERAL LOCATIONS $\sigma > \sigma_u$, BUT ONLY THE 12 SEC. DECEL 8067 (11700) SURF. σ IS OVER STRAIN TO FAILURE LIMIT. DO NOT EXPECT EDGE CRACKS.
2. STRESSES ARE MAX. PRINCIPAL STRESS. ARROWS INDICATE DIRECTION.
3. Z/M = ZrO₂/CoCrAlY

Figure 55 Initial Stress Field



*ALL STRESS ARE PARALLEL TO THE INTERFACE EXCEPT THE STRESS AT THE CRACK TIP WHICH WAS AT APPROXIMATELY $\pi/4$ RADIAN (45 DEGREES).

UNITS: MAX. PRINCIPAL STRESS \sim N/cm² (PSI)

Figure 56 Crack Entering 85/15ZrO₂/CoCrALY Layer

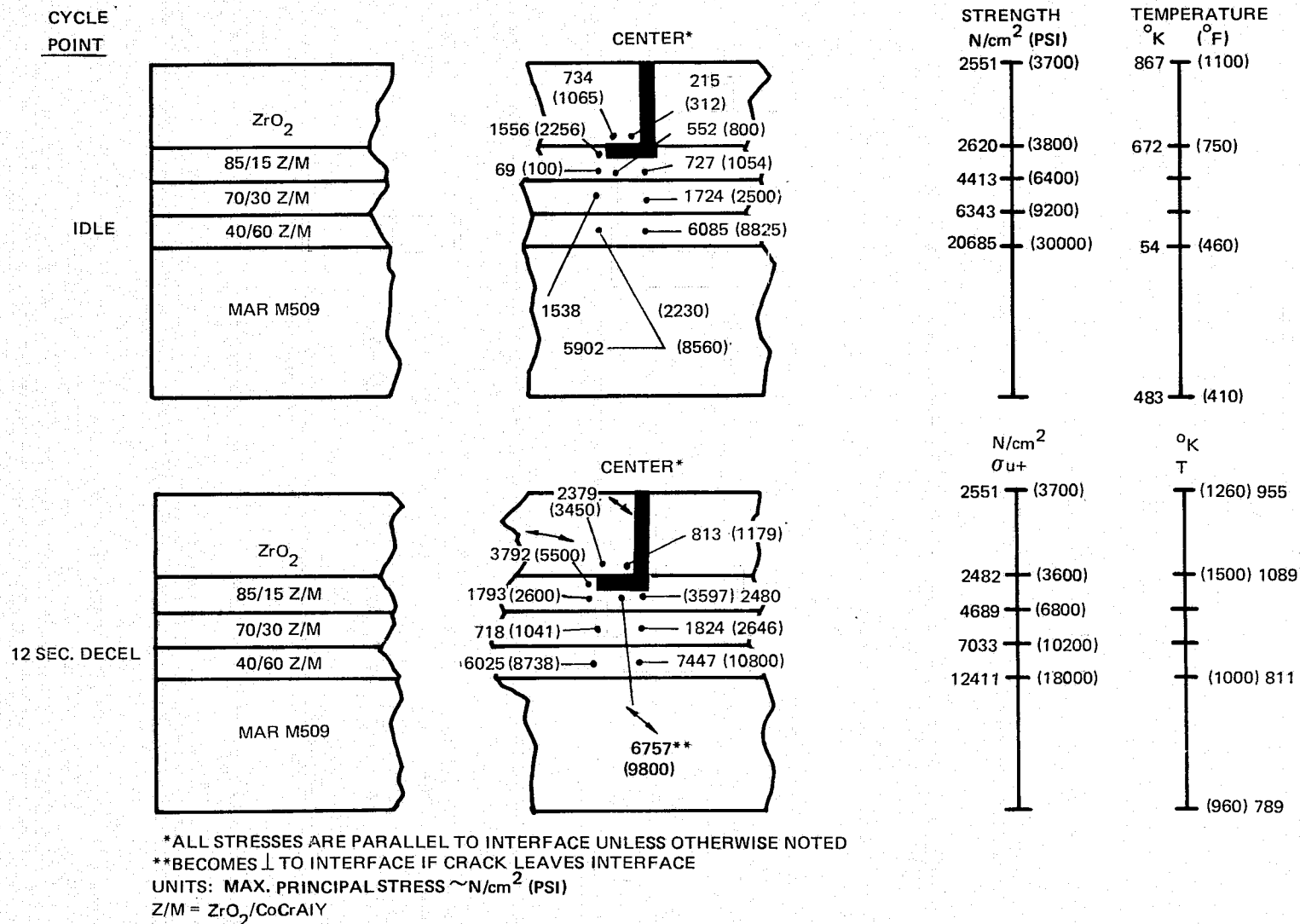
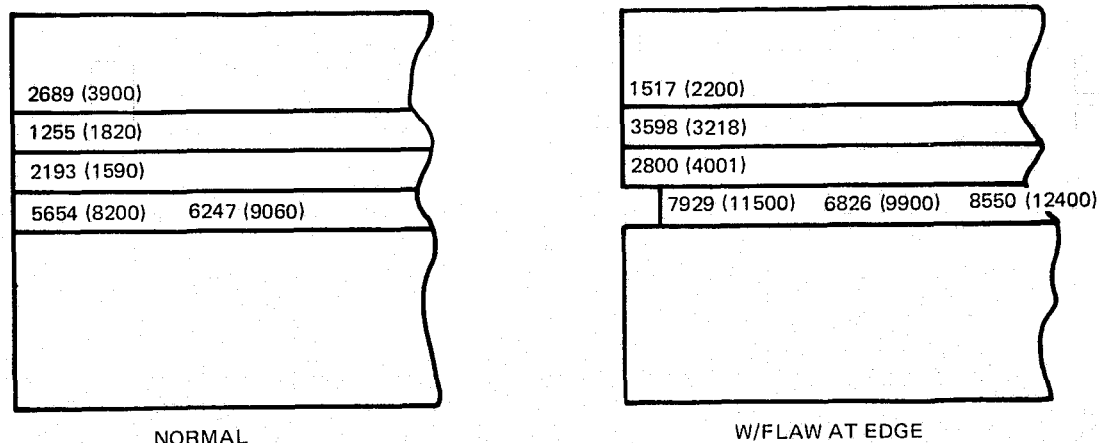


Figure 57 Crack Allowed to Turn at Interface with 85/15 ZrO₂/CoCrAlY Layer



NOTE: UNITS = MAX. PRINCIPAL STRESS $\sim \text{N/CM}^2$ (PSI)

Figure 58 Stress at Irregular Edge

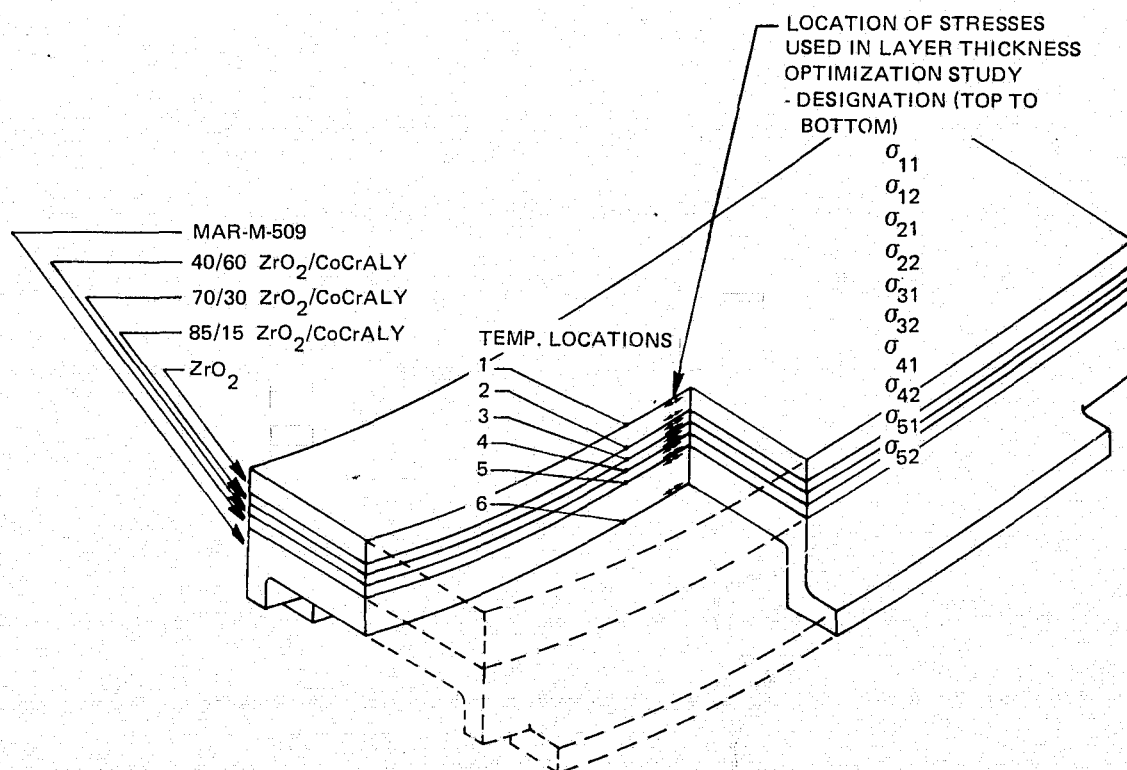


Figure 59 Location of Temperatures and Stresses Reported in Table XIII

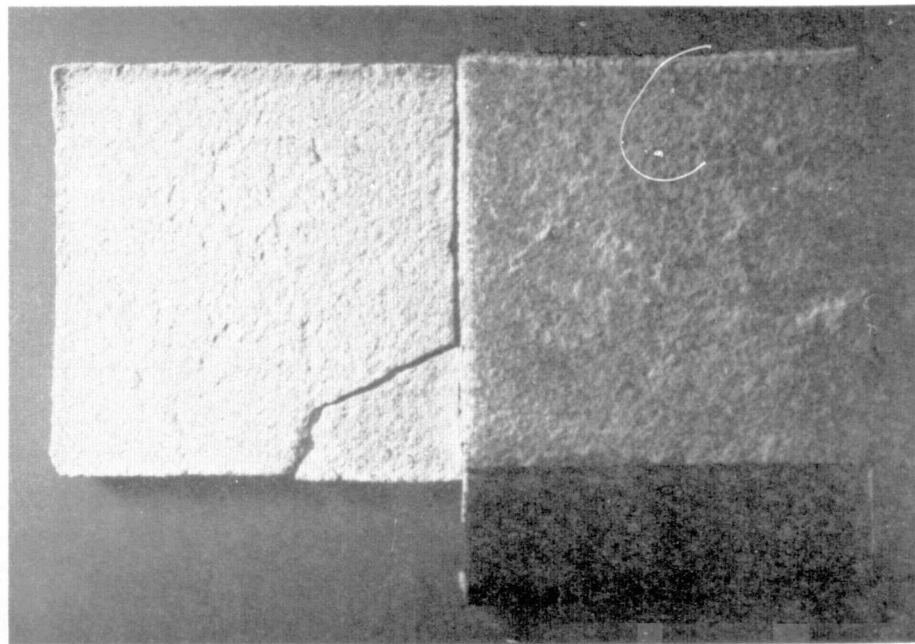
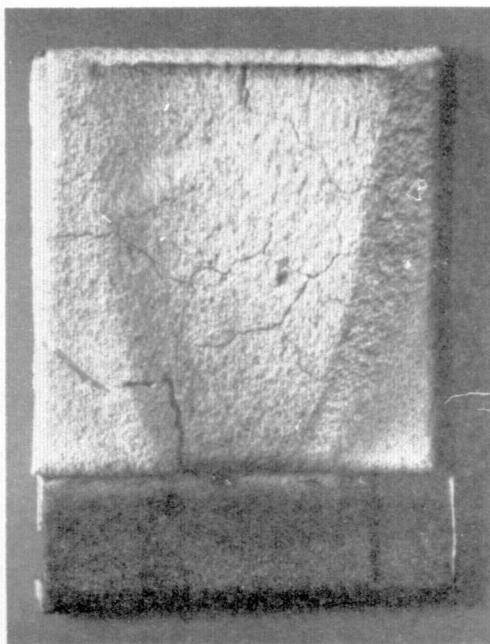


Figure 60 Erosion Specimen, Optimized Configuration

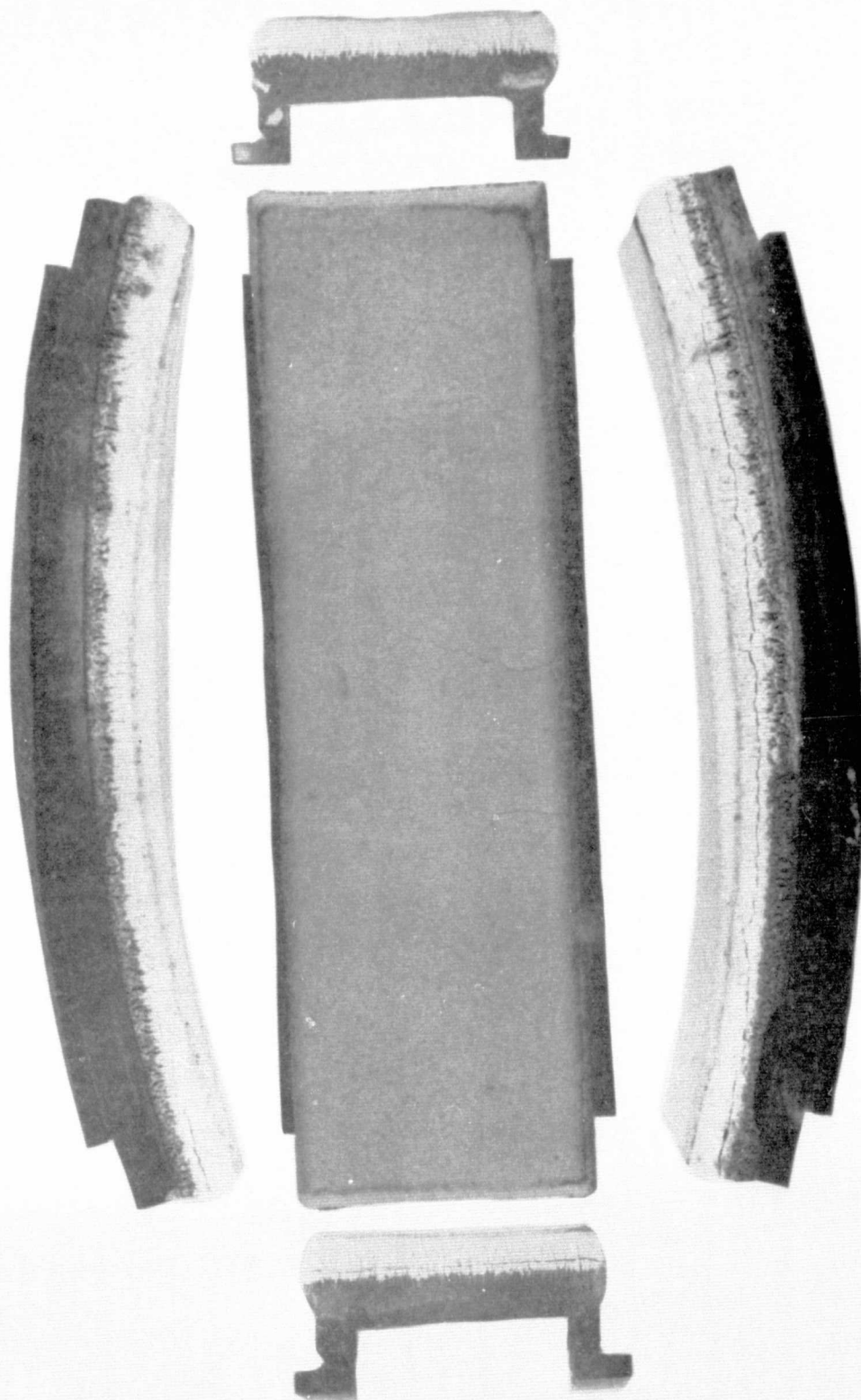


Figure 61 Optimized Configuration, Post Thermal Fatigue Test (Test No. 6)

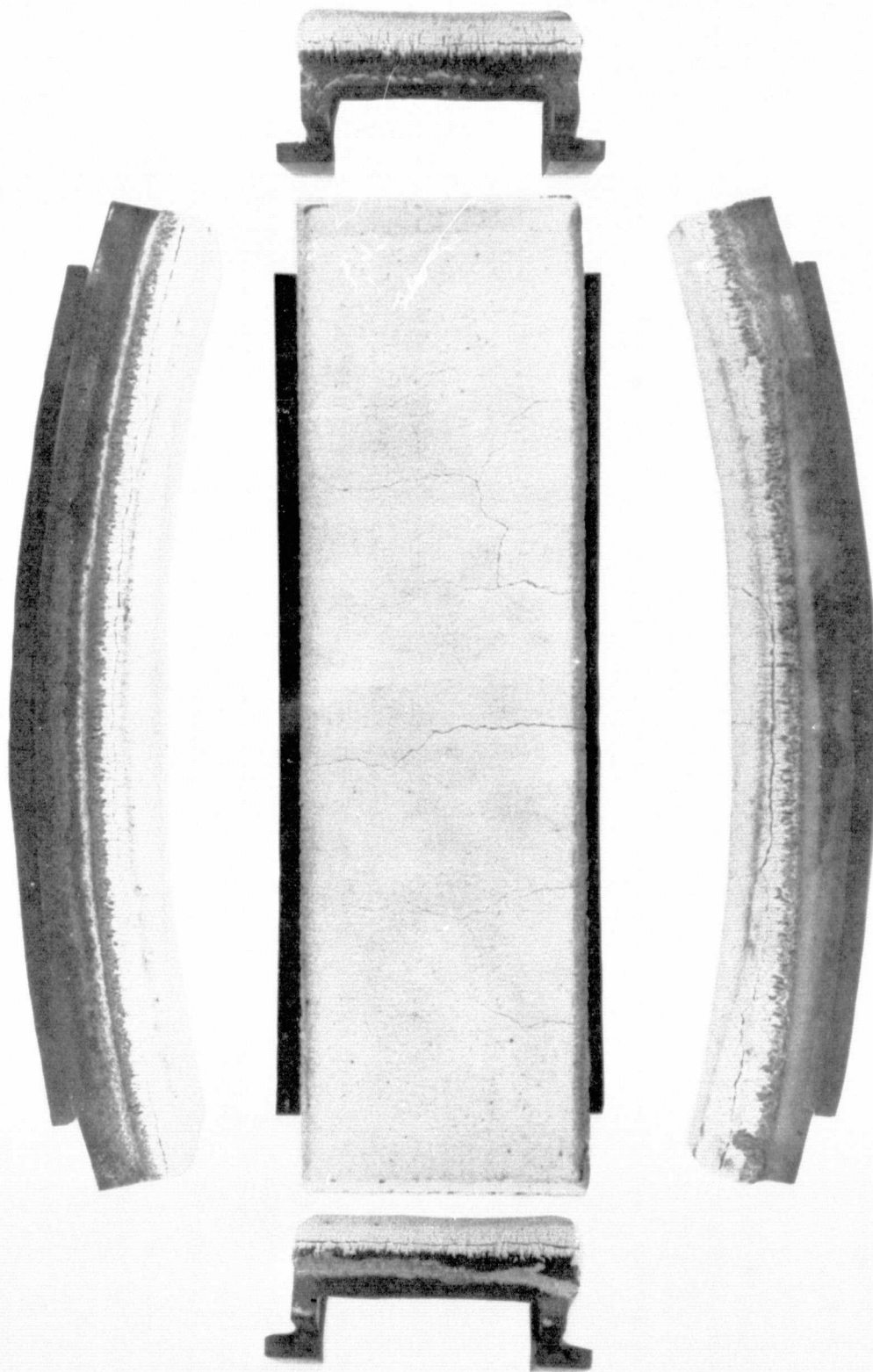


Figure 62 Optimized Configuration, Post Thermal Fatigue Test (Test No. 7)

ORIGINAL PAGE IS
OF POOR QUALITY

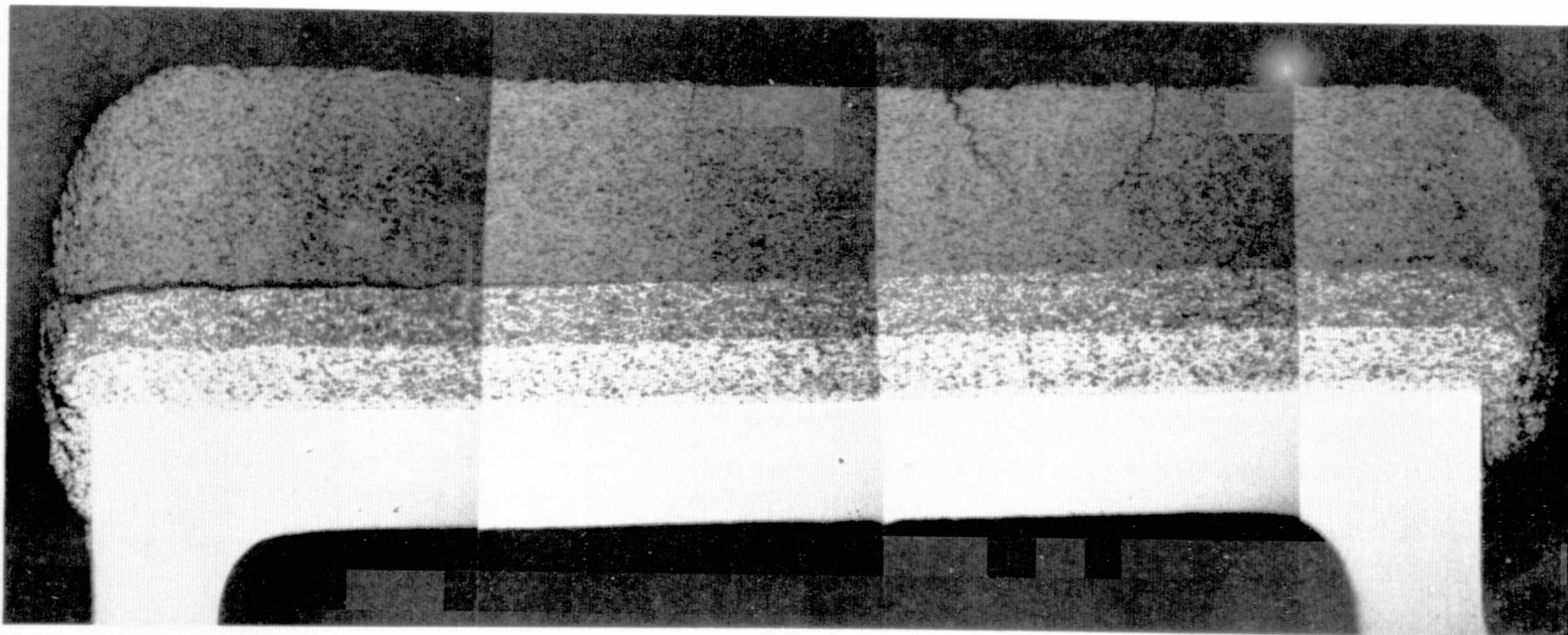
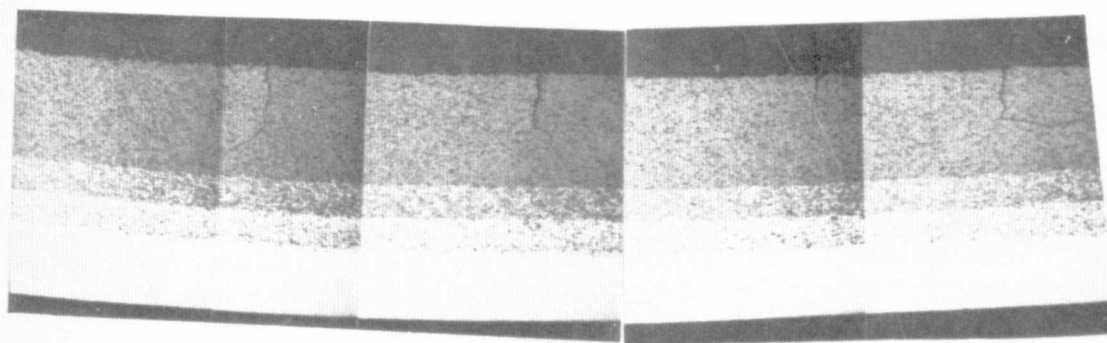
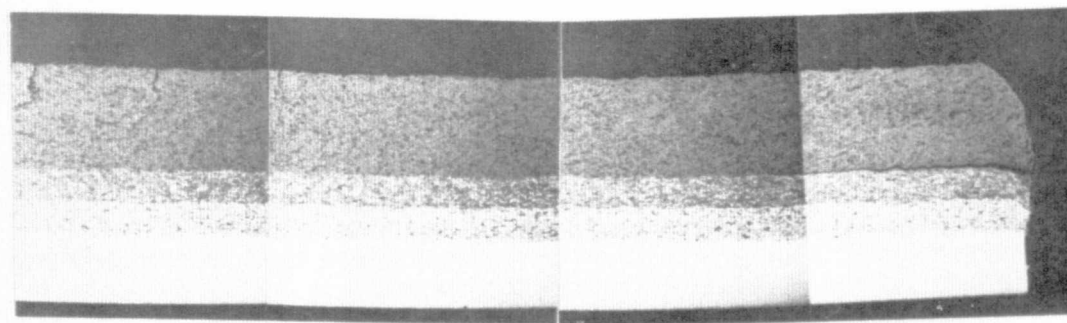


Figure 63 *Optimized Configuration, Thermal Fatigue Tested Specimen,
Axial Section (Test No. 6)*

ORIGINAL PAGE IS
OF POOR QUALITY



A



A

Figure 64 *Optimized Configuration, Post Thermal Fatigue Tested Specimen, Circumferential Section (Test No. 6)*

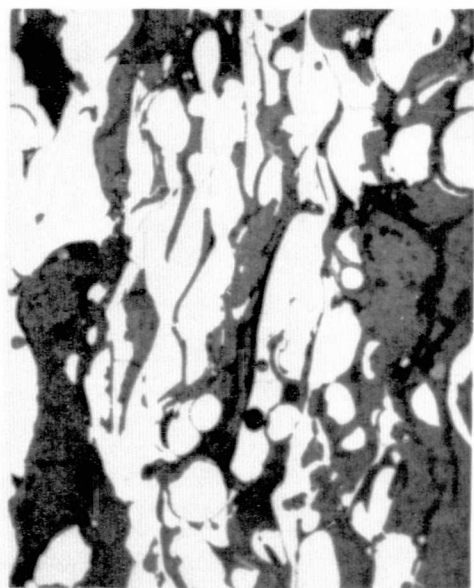
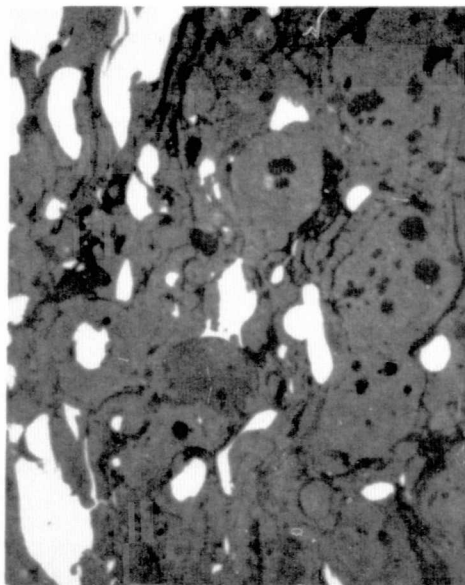
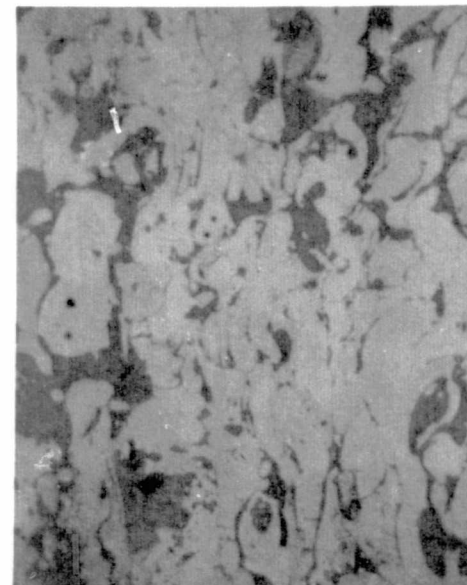
 ZrO_2 85/15 $\text{ZrO}_2/\text{CoCrAlY}$ 40/60 $\text{ZrO}_2/\text{CoCrAlY}$

Figure 65 Optimized Configuration Microstructure

ORIGINAL PAGE IS
OF POOR QUALITY

APPENDIX A

Singularity at the tip of a through crack at the center of an infinite plate in plane stress:

$$\sigma = \frac{K_I}{\sqrt{\pi r}}, \quad K_I = \text{constant}$$

At the tip of a crack of tip radius ρ ,

$$\sigma_{\text{tip}} = \frac{K_I}{\sqrt{\pi \rho}}$$

Therefore, for a given constant ρ ,

$$\sigma_{\text{tip}} \propto K_I$$

Similarly, the ultimate strength of a body containing such cracks, the largest of which has a half-length a_0 , is:

$$\sigma_u = \frac{K_{IC}}{\sqrt{\pi a_0}}$$

For a given a_0 , then,

$$\sigma_u \propto K_{IC}$$

Therefore, $\frac{K_I}{K_{IC}} = \frac{\sigma_{\text{tip}}}{\sigma_u} \times C$, where the constant C is implicit in the correction factor

plot of Figure 6 in that $C \times \sigma_{\text{tip}} = \sigma_{\text{corrected}} = \frac{\sigma_{\text{theoretical}}}{\sigma_{\text{FE (Fig. 54)}}} \times \sigma_{\text{tip F.E.}}$

Thus:

$$\frac{K_I}{K_{IC}} = \frac{\sigma_{\text{tip corrected}}}{\sigma_u}$$